

UNIVERSITY OF PADOVA
Department of Industrial Engineering
Doctoral Program in Industrial Engineering
Curriculum: Energy Engineering
Cohort XXXVI

NUMERICAL METHODS FOR DESIGN, VALIDATION AND OPTIMISATION OF HIGH-PERFORMANCE WATERJETS

Thesis for the degree of Doctor of Philosophy

A research project entirely funded by SEALENCE S.p.A. SB

Prof. Giulio Rosati, Course Coordinator
Prof. Ernesto Benini, Candidate's Supervisor
Prof. Francesco De Vanna, Candidate's Co-supervisor

Ph.D. Candidate: FILIPPO AVANZI

Padua
February 28, 2024

*Così ne disse; e però ch'el si gode
tanto del ber quant'è grande la sete,
non saprei dir quant'el mi fece prode.*

— Dante, *Divina Commedia*, Purgatorio, Canto XXI, vv. 73-75

ABSTRACT

This study scientifically characterises a novel waterjet concept. The innovative design presents a single unit housing the entire propulsive system, which distinctively eliminates the need for any internal components within the hull. Its superiority over existing propulsors lies in the elimination of the detrimental presence of the shaft and the capability to be positioned significantly below the waterline. Operations at deep submergence facilitate the processing of an axial, uniform capture stream tube, resulting in the generation of thrust in potential, perfect alignment with the advancing direction. The primary objective of this work is to establish a comprehensive and robust numerical framework addressing key aspects of fluid dynamic behavior, including system design, validation of computational models, and possible optimisation techniques. The proposed methodology involves the application of various methods in a systematic progression of increasing complexity. Beginning with a 1D approach to assess the propulsive performance of the nacelle, inspired by aero-engines principles, the study then transitions to the implementation of a meanline code for blades design. The latter employing a Blade Element Method (BEM) integrated with several empirical correlations to model various physical flow phenomena. The two approaches prove in general stable. However, computations of the propulsive statistics show significant accuracy in predicting the thrust coefficient but evidently overestimate the efficiency. Differently, hydraulic design shows accurate capturing of the leaving flow velocity and direction, but exaggerates the machine head rise capability. In light of providing a verification of the preliminary study, Computational Fluid Dynamic (CFD) is adopted as the reference tool, offering a comprehensive assessment of the numerical models through comparison with experiments on public domain test cases. Employing a generalised approach, the study considers various turbulence models and grid refinements to solve the Reynolds-Averaged Navier Stokes (RANS) equations, thoroughly evaluating predictive accuracy. The adoption of a 2D-axisymmetric simplification proves to be a reliable strategy for reproducing test measurements, particularly for inlets generated by a revolved profile. Conversely, a single-channel periodic reduction emerges as a more suitable approach for simulations involving bladed geometries. During nominal operations, the study observes an overestimation of both head rise and hydraulic efficiency. However, a systematic manipulation of the Zwart cavitation model coefficients significantly enhances accuracy in predicting pressure rise during thrust breakdown simulations. Subsequently, the study proceeds with the numerical analysis of the installed pump operations, after defining an integration strategy for the two previously isolated sub-systems. Hydraulic statistics indicate minimal influence from the upstream intake. Nevertheless, a detailed assessment of the entire system

off-design performance highlights a deficiency in the matching strategy, illustrating peak performance at differing advancing speeds for the inlet and the pump. This observation suggests the need for optimisation to ensure feasible operations over wider ranges of mission envelopes. Consequently, a Latin Hypercube Sampling (LHS) is adopted as the initial step for a Genetic Algorithm (GA) optimisation. This investigation involves the manipulation of the 2D-axisymmetric intake geometry, focusing on three key decision variables: axial and radial locations of the highlight, and throat radius. Through a two-objective oriented analysis, the study reveals that while the drag contribution can be readily reduced, the maximisation of pressure recovery is inherently limited. A concluding evaluation employs the 3D installed model for three optimised solutions, thus pursuing a multi-fidelity strategy. The evidence suggests that, while cruise operations may experience improvement, a multi-point optimisation, including off-design performance, may result necessary to prevent the generation of individuals with unfeasible off-cruise behaviour, accentuated by emphasised cavitation evolution.

CONTENTS

1	Introduction	1
1.1	Context	1
1.2	Why yet another waterjet?	7
1.3	Thesis framework	10
1.4	Research products	11
2	Design	13
2.1	Propulsor model	13
2.1.1	Methods	13
2.1.2	Results	19
2.2	Blade Element Method	21
2.2.1	Methods	22
2.2.2	Results	35
3	Validation	49
3.1	Numerical methods	49
3.1.1	Governing equations	49
3.1.2	Modelling of turbulence	50
3.1.3	Modelling of cavitation	52
3.1.4	Thrust-Drag Bookkeeping	53
3.2	Propulsor 2D-axisymmetric model	54
3.2.1	Computational model	54
3.2.2	Results	56
3.3	Pump 3D model	62
3.3.1	Computational model	62
3.3.2	Results	65
3.4	Installed pump model	86
3.4.1	Computational model	86
3.4.2	Results	90
4	Optimisation	99
4.1	Methods	99
4.1.1	Design Of Experiments	99
4.1.2	Evolutionary algorithms	99
4.2	Intake optimisation	101
4.2.1	Latin Hypercube Sampling	104
4.2.2	Genetic Algorithm	108
4.3	Installed model outcomes	113
4.3.1	Results	113
5	Conclusions and outlook	123

1 INTRODUCTION

1.1 Context

Background on marine propulsion

The adoption of waterjet systems in marine propulsion is a relatively recent trend. Although the concept dates back to the 17th century, practical implementation was constrained by technological limitations until the mid-1900s, restricting the availability of propulsors primarily to conventional screw propellers [1]. Technically, the two systems share the same physical principle. The thrust being the result of a momentum imbalance between the advancing and the rear cross sections of the stream tube encompassing the propulsor [75]. As a result, the flow path from the free stream to the discharge wake may be indiscriminately idealised as a generic convergent stream surface of revolution. However, a distinction arises: in open rotors, this outline varies with the advancing velocity, while in waterjets, the capture stream tube is constrained by the bounding ducting. This feature enables the pump to operate almost independently of the free stream under nominal conditions [1]. Specifically, these propulsors are characterised by three fluid dynamic components: a diffuser intake, a pumping device, and a convergent nozzle. Therefore, when examining the flow evolution upstream of the pump interface, a distinctive property of waterjets becomes apparent: the diffusion through the inlet. This ability allows the rotating blades to safely operate at significant shaft speeds, preventing the occurrence of cavitation [125]. A phenomenon that induces the transition of the liquid phase to vapour where the fluid pressure drops below the specific vapour pressure. These bubbles, or cavities, are primarily responsible for performance degradation and propulsor noise. Moreover, they can lead to structural damages when reaching a higher pressure region of the blade, causing their sudden explosion [21]. Consequently, cavitation represents a major propulsive limit for open rotors, where the static pressure on the suction side is only regulated by the Bernoulli equation, written for the fluid relative velocity on the blades inertial frame. In this regard, ducted propellers represented the first approach to overcome this problem, by decelerating the flow directed to the machine through an axisymmetric shroud [125]. Waterjets, to some extent, fall within this class of propulsors and can be distinguished only based on the presence of a longer duct [19].

Various factors contribute to choosing waterjets over conventional propellers, although the ultimate decision inevitably hinges on the specific application, which serves as the primary cost function for the designer [18]. For high-speed vessels, which need to achieve speeds over 30-35 knots, they currently represent a well-established solution in either civilian and military

1. INTRODUCTION

environments, particularly when navigating through shallow waters within the mission envelope. Indeed, at these flow regimes, waterjets exhibit higher efficiencies compared to other systems. Additionally, their insensitivity to free stream conditions contributes to the remarkable manoeuvrability of these propulsive units. This characteristic, along with enhanced noise reduction capabilities, holds particular significance for military applications [100]. On the other hand, these propulsors may increment the weight of the system and require greater costs for design and development of the several components. In this regard, research over the years has favoured the choice of axial- or mixed-flow pumps, which offer dual benefits: they handle higher mass flow rates, thereby reducing the head rise, which, in turn, enhances propulsive efficiency; and they can operate at lower speeds, minimising shaft torque and, consequently, mechanical requirements [1].

As anticipated, the inlet represents a fundamental section for waterjet propulsors. In fact, the way it directs the mass flow rate to the pump heavily affects the pressure rise capability and, as a consequence, the entire system propulsive performance [59]. Based on the intake shape, waterjets are commonly classified into two types, namely: ram (or pod) and flush (Fig. 1.1). While the first typology is the typical choice for hydrofoils [54], the latter represents the common installation on a wider selection of applications [100]. Details on flush intakes are beyond the purposes of the present work, with only some of the copious research products left for the potential interest of the reader [100, 99, 22, 42, 59]. Anyhow, it is important to introduce certain prop-

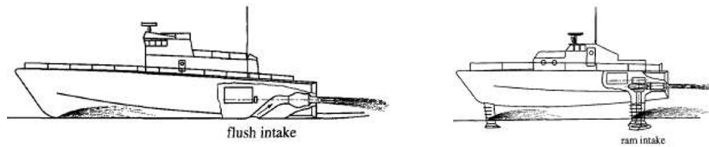


Figure 1.1: Schematic representation of flush and ram intakes, adapted from Eslamdoost [42].

erties of the two configurations. Generally, flush and ram intakes are designed to draw water from different vertical locations below the waterline and duct it towards the pump housed within the vessel. In the case of flush inlets, Bulten [22] identified four primary factors responsible for the non-uniformity of the mass flow rate: hull boundary layer ingestion, bend capture section, shaft obstruction, and deceleration through the ducting. Although the displacement allows pod waterjets to collect a uniform, undisturbed flow at the highlight section, the resulting stream is impacted by higher losses associated with the submerged nacelle and the longer ducting [71]. However, another advantage is that these installations, in contrast to the previous ones, are not susceptible to air ingestion phenomena [1].

To complete the characterisation, it is worth spending a few words on

pumpjet systems. This particular configuration of ducted propeller is a common installation for underwater vehicles, where it is typically integrated astern the centerbody (Fig. 1.2) to efficiently exploit the tailcone boundary layer profile [46]. Unlike a simple shrouded rotor, these units are often complemented by a bladed stator upstream of the exhaust section [60, 132]. Despite

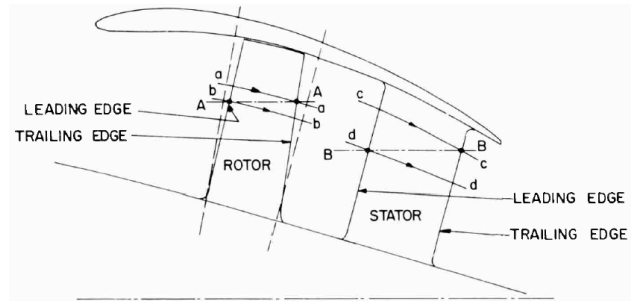


Figure 1.2: Schematic meridional view of a pumpjet for underwater vehicle [55].

the numerous similarities with waterjets, with which they share some advantages such as efficiency and noiselessness [46], Wislicenus [125] proposes separate definitions based on the placement of the pumping device inside or outside the hull. Dating back to 1973, this definition now appears to be surpassed by the latest advancements. In fact, the adoption of inclined shafts has enabled a different design that combines the properties of a fully submerged pumpjet with those of an internally installed conventional waterjet [62]. Thus, possible configurations may include entirely outboard shrouded units [115, 61] or scoop inlet solutions with a partially hull-integrated propulsor [62]. While both strategies improve waterjet losses by reducing deflections and vertical lifts through the ducting [115], the influence of the shaft on detrimental effects and flow distortion, hull boundary layer ingestion due to the vicinity to the vessel, and oblique flow evolution cannot be avoided [43, 61].

Design

Although the different configuration of the corresponding propulsors, the design approaches for pumpjet shrouds and waterjet inlet nacelles share common characters. These in general stem from the assumption of an isolated, axisymmetric throughflow duct and draw inspiration from the aeroengines propulsion principles [71, 55]. Thus, the spirit behind the definition of a shape primarily combines cavitation-free operations and proper pressure recovery capability. These need to be satisfied over a range of Inlet Velocity Ratio (IVR), which is defined as the inlet highlight to free stream velocity ratio. This parameter quantifies the shape of the capture stream tube, serving as an index for the operating point. Values around 1 identify the optimal cylindrical con-

1. INTRODUCTION

figuration for cruise conditions. While lower values are commonly accepted for the design point to generate a certain amount of pre-diffusion, excessively small values are to be avoided to prevent external cavitation. Conversely, IVR greater than 1, which are typical of take-off operations, may induce internal lip cavitation, and consequent inlet choking up to the critical situation of pump starvation [111]. Preliminary solutions for tentative geometries are obtained through either potential flow methods or simplified solutions of irrotational, inviscid flow momentum equations. In the first case, finite difference schemes are available, but the panel method by Hess and Smith [57] is often favoured for computational convenience. Thus, viscous effects can be included using integration of a wide range of possible boundary layer theories, as well as empirical correlations [71]. On the other hand, discretisation and computation of momentum conservation is favourably achieved using Streamline Curvature Methods (SCM) across a chosen number of stream surfaces of revolution, passing through the duct [46]. Even at preliminary design stages, optimisation can be conducted. The latter in general relying on a minimisation of external and/or internal loss sources [71].

In addition to the shroud dimensions, the design strategies may be adapted to perform a simultaneous definition of the blades geometries [46]. Whether the pump is designed concurrently with or prior to the corresponding casing, the rotational regime is a mandatory datum. While this parameter is left to the discretion of the designer, a possible technique for its determination relies on approximate early considerations on the specific speed. The latter varies with the rotor velocity, once the required flow rate and head rise are defined to satisfy the propulsive constraint. Here, the work done by the pump directly relates to the kinetic energy imbalance across the propulsor [55]. Research in this field has concurred over the years on the selection of axial- or mixed-flow pumps with high specific speeds, based on the evidence that higher mass flow rates benefit propulsive efficiency [1]. In this regard, the adoption of Blade Element Methods (BEM) appears a well-established practice for the design of axial-flow incompressible vanes [55, 106, 94, 46, 134]. These techniques typically consider the blades as a spanwise stacking of independent, inviscid aerofoils, or elements, with the specific fluid dynamic behaviour of each element influencing the overall performance of the row. Following meanline approaches, no modelling of the blade-to-blade flow is included; instead, the flow evolution is lumped at stations located upstream and downstream of each row. Thus, to achieve high-fidelity performance estimations, a broad array of experimental and numerical correlations can be integrated to capture real-machine flow effects. Consistency in the solution is typically ensured through iterative methods, enforcing the satisfaction of both mass and flow momentum conservation across the Blade Elements (BE). In this regard, the remarkable contribution of Lieblein during the 1950s deserves special recognition. The systematic experimental analysis performed over straight blades, compressor

cascades allowed for the establishment of a first comprehensive database on this field. The exploration of various geometrical and flow parameters resulted in the development of correlations for optimal blade incidence, deviation, and profile losses. These relations, even today, serve as the basis for nearly every meanline code developed for compressible applications [122, 16, 15, 89]. Thus, the utilization of compressors-derived correlations has proven to be efficient for pump designs as well. The efficiency of BEMs has sustained the interest of the research community, resulting in ongoing revisions and integrations of the original correlations over the years [101, 67, 106, 8, 16, 40, 41]. In recent times, the coupling of vortex lattice propeller codes with axisymmetric Euler solver proved an advanced and reliable strategy for waterjets pumps geometry design [92].

Validation

After the geometrical definition, performance verification has traditionally relied on experimental measurements of prototypes. The gradual shift from ram-type inlets to flush applications [1] has led to reduced interest in such systems, potentially justifying the limited availability of related research products. To the author's best knowledge, the only detailed investigation of a high-speed hydrodynamic nacelle is the relatively dated work by Sobolewski [111]. In that study, global and local statistics are evaluated for various operating points encountered within a potential mission envelope, utilising a plug-regulated, variable area podded intake. Conversely, the published tests results on pumpjets are numerous and definitely more recent [117, 116, 118, 107].

Partly, this is facilitated by the growing advancements in experimental facilities capable of handling and investigating cavitation. In fact, despite the complex and highly nonlinear nature of this phenomenon, researchers have conducted numerous experiments in recent decades to enhance understanding and mitigate its detrimental effects. Initial studies focused on observing cavitation in stationary cases like hydrofoils [69, 6, 65]. However, in turbomachinery, challenges arise due to blade rotation, making the characterisation of vapour development complex, especially at the blade tip, where relative motion with respect to the casing occurs [45]. While nominal operations were effectively measured, ensuring local accuracy, as early as the 1960s [30, 93, 94, 134, 133], detailed studies on clearance leakage evolution emerged towards the end of the century [70]. Later on, recent technological advancements, as seen in the work of Wu et al. [127], using Particle Image Velocimetry (PIV) measurements, have provided insights into the evolution of the Tip Leakage Vortex (TLV). The impact of the TLV on cavitation breakdown onset has been highlighted by Tan et al. [119] and Chen et al. [25], emphasising its substantial influence on attached sheet cavitation near the rotor blade tip, leading to the

1. INTRODUCTION

formation of Perpendicular Cavitating Vortices (PCVs).

Concurrently, the growing accessibility of computational resources has driven remarkable advancements in Computational Fluid Dynamics (CFD), establishing it as a robust and efficient tool for forecasting the development of flow phenomena [12, 31, 11, 32]. To date, the only known numerical investigation available on isolated waterjet ram inlet performance consists on a 2D axisymmetric CFD assessment by the author and co-authors [10]. On the other hand, pumpjets are commonly analysed using three-dimensional models that include the shroud and the bladed components. Here, computational demand may be reduced through axial periodicity for open water simulations [49, 60, 61].

However, when accurate predictions are to be obtained for rotating bodies within incompressible media, the availability of validated cavitation models becomes mandatory. In this regard, CFD plays a crucial role in the initial phases of machine design, serving as a valuable tool for investigating cavitating structures at early design stages. Over time, the modelling of phase transition has undergone several formulation revisions to enhance accuracy in predicting vapour cavity behaviour in industrial applications [114]. Currently, a widely adopted solution incorporates mass-transfer rate approaches. Two commonly referenced techniques, namely the Singhal method [109] and the Zwart-Gerber-Belamri (ZGB) method [135], have been formulated and successfully implemented and validated in popular commercial CFD software, such as ANSYS solvers, Fluent® [5], and CFX® [2]. These models find widespread application in axial-flow pumps for waterjet propulsion, centrifugal water pumps, and pump inducers [7].

Reynolds Averaged Navier-Stokes (RANS) analyses have been primarily employed to study cavitation in complex machines, chosen for their ability to reduce computational costs, despite limitations in modelling turbulent effects and cavitation events. Turbulence modelling, in particular, significantly influences cavitation inception, as the low pressure within the vorticity feeds the generation of vapour bubbles [20]. In this context, various eddy viscosity models, including the $k-\omega$ Shear Stress Transport (SST) model by Menter [91], have been utilised to account for subgrid-scale terms in different hydraulic machinery analyses [87, 74]. Numerous examples can be found in the literature for further insights [7, 76, 96, 78, 74, 129, 128, 50, 130, 79, 53].

Regarding cavitation modelling, recent studies have proposed modifications to standard models aimed at enhancing the accuracy in predicting cavitating structures. Specifically, modified versions of the Zwart-Gerber-Belamri (ZGB) cavitation model have been formulated by Zhao et al. [131] and Guo et al. [51], addressing the influence of vorticity on cavitation. A study conducted by Lindau et al. [76] reached favourable results for the axial-flow waterjet pump designed by Michael et al. [92], employing a steady-state Reynolds-Averaged Navier-Stokes (RANS) approach with a homogeneous

multiphase assumption and a mass-transfer rate cavitation model. The chosen cavitation model features empirical coefficients set to default values, ensuring good performance for general applications encompassing both simple geometries like hydrofoils and complex machinery. Additionally, Liu et al. [77] conducted a sensitivity analysis of the Rayleigh–Plesset model applied to a centrifugal pump, demonstrating improved predictive accuracy over experimental results, primarily attributed to the reduction in the condensation coefficient. In the same path as experimental tests, advancements in cavitation modelling focuses on TLV prediction. Consequently, substantial efforts have been dedicated to numerically predicting this phenomenon across geometries ranging from simple [38, 51, 131] to complex [48, 50, 128]. As highlighted by Cheng et al. [27], the RANS approach appears somewhat limited in predicting the intricate structures associated with TLV. For more accurate predictions, advanced CFD methods such as Large Eddy Simulations (LES) prove more suitable [13, 26, 80, 52, 27].

Optimisation

Thanks to reliable CFD models, marine propulsion performance improvements have become a more feasible task. Multi-objective optimisation of existing systems are commonly adopted for either flush intakes enhancements [59, 49] and pumpjets propulsive capability increments [126, 47]. These studies inevitably involve parameterising the geometries of propulsors, encompassing both ducting and blades. Manipulation of the component shapes is systematically performed to generate geometrical variants, or individuals. Thus, the corresponding propulsive performance metrics are evaluated using CFD to serve as objective functions for the optimisation process. Design Of Experiments (DOE) through Latin Hypercube Sampling (LHS) proves in general a well-established approach. Thus, detailed refinements are typically approached using Genetic Algorithms (GA), with the Non-Dominated Sorting Genetic Algorithm-II (NSGA-II) standing out as an efficient and favourable implementation. Although studies related to the optimisation of ram type waterjet inlets are beyond the author’s current knowledge, the extensive literature concerning the enhancement of aero-engines nacelles propulsive performance is regarded as valuable and relevant [110, 81, 82, 103]. In fact, while the phenomena regulating the two systems differ in many aspects, the functions they are required to fulfil are the same. These including high pressure recovery capability and a low contribution to resistance.

1.2 Why yet another waterjet?

Considering the state-of-the-art in marine waterjet propulsion, it is evident that the available systems cannot be analysed in isolation from the associ-

1. INTRODUCTION

ated vessel. Although outboard solutions, like certain pumpjets, have been discussed, the requirement to place them near the hull for connection to the internal engine shaft partially discards the benefits associated with a uniform mass flow rate processed by the pump.

The recent advancements in industrial technology have shown that, thanks to the electric power supply, an autonomous, outboard unit can be designed, in the same spirit of the aeronautical applications. This Outboard Dynamic-inlet Waterjet (ODW) comprises a single device that houses the intake, pump, and exhaust nozzle. Since there is no shaft required to drive the rotor, there are no additional obstructions affecting the entering flow. Consequently, a uniformly distributed velocity profile is directly ducted by the intake to the pump face. Another related advantage is the absence of oblique stream evolution, ensuring that the advancing direction is always aligned with the thrust. Additionally, the propulsor can be positioned sufficiently below the waterline to eliminate hull boundary layer ingestion. One potential benefit includes the ability to use the system as a steering device, eliminating the need for supplementary components and associated losses.

The novelty of the proposed propulsor explains the current lack of dedicated studies. Therefore, the present project aims to establish a comprehensive numerical environment capable of addressing various aspects concerning the system. The manuscript begins with low-order considerations, suitable for addressing possible design strategies for all waterjet subsystems. In this regard, the approach for the nacelle analysis is derived from best practices in aero-engine installations. Thus, a 1D code is developed to serve as a preliminary tool for predicting propulsive performance. Verification of the code reliability is addressed through a comparison with numerical results obtained from an intake-installed pump model developed later in this work. Specifically, the inlet performance prediction is regarded with particular attention, in light of the importance of this component on the system operations. To this end, two approaches are implemented to model the intake pressure recovery, depending on the incoming stream tube: one derived from existing experimental-based correlations and another retrieved from present numerical datasets. The assessment of the bladed components' sizing is achieved using a meanline technique, and a BEM library is implemented in Python for the resolution of mass and flow momentum conservation laws within an axisymmetric duct. Approaching the blade-to-blade field as the stacking of 2D cascades allows for accuracy improvements, by including a list of empirical correlations derived from both experimental databases and numerical methods. The latter addressing multiple effects such as profile deviation, losses due to non-optimal incidence, and detrimental effects from the End Wall Boundary Layer (EWBL), tip clearance leakage flow and three-dimensional secondary evolutions. After proving the code robustness, in terms of sensitivity and stability, three experimental test cases are selected to evaluate the accuracy of

the algorithm, encompassing different operating conditions: an early-stage pump rotor, a high Reynolds number pump rotor, and a complete waterjet pump.

The intention to numerically investigate pump operations under installed conditions inevitably collided with the absence of available measurements on this system for model validation. Such a tool is considered fundamental for characterizing the mutual interactions between the inlet and the pump, which are not accounted for during the design process. Therefore, the possibility to draw reliable predictions on the conditions that may cause distinct performance between isolated and installed configurations is deemed a key aid for the designer during advanced verification stages. Thus, the definition of a high-fidelity computational model is initially approached by investigating the isolated components. To this end, a public ram-type waterjet inlet geometry is selected to study the modelling accuracy of the nacelle. RANS equations are coupled with four turbulence models, and sensitivity is evaluated depending on the domain discretization resolution. Specifically, the axial symmetry of the chosen shape is exploited to reduce the computational effort by adopting 2D-axisymmetric simulations. Internal and external local pressure measurements are employed as metrics for validation. As a second step, an axial waterjet pump test case is selected from the public domain to conduct an extensive numerical analysis. Again, RANS equations are considered. Nominal operations are adopted to evaluate the model accuracy with respect to three turbulence models on three incremental discretization refinements. Here, a single channel for both the rotor and the stator is modelled, exploiting circumferential periodicity. Thus, an extensive study is performed to select a specific computational configuration. To this end, global and local field variables distributions are adopted as qualitative and quantitative metrics, the latter including advanced grid convergence extrapolation and comparison with PIV results from experiments. This computational model is retained for a comprehensive study regarding the dependence of the ZGB cavitation model on the constitutive coefficients of its foundational equations. The corresponding values are systematically altered, and the model response is evaluated at both integral and local levels, in comparison with experiments if applicable. Concerning this investigation, thrust breakdown loops are emulated from tunnel tests and the corresponding numerical results are adopted as primary metrics. Thus, the discussion is enriched with in-depth analysis, by considering the behaviour of field variables at a local level. The last step of this part of the work consists in the definition of the integrated model. Thus, a strategy for the pump installation is proposed and detailed. The geometries of the two isolated components are properly manipulated to allow for mutual matching. The considerations drawn for the individual numerical analyses are exploited to build the computational model. Results from the computations are discussed at both in- and off-design operations. To this end, the propulsor

1. INTRODUCTION

maps are generated for three rotational regimes, by systematically varying the advancing free stream velocity. In this regard, both hydraulic and propulsive integral performance is analysed. The latter computed according to the aero-engines Thrust-Drag Bookkeeping (TDB) principles. In addition, attention is quantitatively directed towards local flow dynamics, evolving on the intake and propagating the corresponding effects on the whole system operations.

From the results obtained within this investigation, critical effects of the installation strategies suggest that a system optimization is required. As is common practice in aero-engine studies, this task is approached using a multi-fidelity technique. Thus, the 2D-axisymmetric model of the intake is adopted for the optimization process, and the corresponding outcomes are subsequently evaluated on the 3D installed model. An initial DOE is performed, generating a LHS decision variables distribution. Here, radial and axial coordinates of the highlight section as well as the throat radius are allowed to vary on the parameterised inlet geometry. The emergence of a Pareto confirms pressure recovery and intake drag as conflicting objectives. Thus, the corresponding dominant individuals are selected as the initial population for a genetic evolutionary optimization using the NSGA-II.

1.3 Thesis framework

The structure of the manuscript is organised to follow an increasing complexity of the methods adopted for the investigations. This leads to the division of the discussion into three main chapters, corresponding to the key issues the thesis aims to address. Each of these blocks first introduces the numerical methods adopted for the subsequent discussions, then the results are presented. A breakdown of the sections content is summarised below.

Chapter 2 addresses the design aspects, differentiating between the external system and the bladed parts. Thus, Section 2.1 focuses on the nacelle 1D modelling while Section 2.2 discusses the implementation of the BEM code and the corresponding results.

Chapter 3 provides thorough insights on the validation of CFD models. Specifically, Section 3.1 introduces the numerical methods adopted for turbulence and cavitation modelling and the TDB metrics for the propulsive performance evaluation. Then, Section 3.2 discusses the computational results obtained with the 2D-axisymmetric intake model, while Section 3.3 focuses on the extensive study performed on the 3D isolated pump modelling. The definition of the installed model and corresponding outcomes are presented in Section 3.4.

The optimisation study is included in Chapter 4. Here, the principles of the methods are briefly introduced in Section 4.1. Thus, the results of both the DOE and the GA analyses are discussed in Section 4.2. Evaluation of the optimised geometries effects on the 3D installed configuration are addressed

in Section 4.3.

Finally, Chapter 5 draws the conclusions and state the intentions for the future developments.

1.4 Research products

The indexed works published during the past three years are listed below.

- [1] AVANZI, F., BAÙ, A., DE VANNA, F., and BENINI, E. “Numerical Assessment of a Two-Phase Model for Propulsive Pump Performance Prediction”. In: *Energies* 16.18 (2023). DOI: [10.3390/en16186592](https://doi.org/10.3390/en16186592).
- [2] DE VANNA, F., AVANZI, F., COGO, M., SANDRIN, S., BETTENCOURT, M., PICANO, F., and BENINI, E. “GPU-acceleration of Navier-Stokes solvers for compressible wall-bounded flows: the case of URANOS”. In: *AIAA SCITECH 2023 Forum*. National Harbor, MD & Online, Jan. 2023. DOI: [10.2514/6.2023-1129](https://doi.org/10.2514/6.2023-1129).
- [3] DE VANNA, F., AVANZI, F., COGO, M., SANDRIN, S., BETTENCOURT, M., PICANO, F., and BENINI, E. “URANOS: A GPU accelerated Navier-Stokes solver for compressible wall-bounded flows”. In: *Computer Physics Communications* 287 (2023), p. 108717. DOI: [10.1016/j.cpc.2023.108717](https://doi.org/10.1016/j.cpc.2023.108717).
- [4] AVANZI, F., DE VANNA, F., RUAN, Y., and BENINI, E. “Enhanced Identification of Coherent Structures in the Flow Evolution of a Pitching Wing”. In: *AIAA SciTech Forum 2022*. San Diego, CA & Virtual, Jan. 2022. DOI: [10.2514/6.2022-0182](https://doi.org/10.2514/6.2022-0182).
- [5] AVANZI, F., DE VANNA, F., BENINI, E., RUARO, F., and GOBBO, W. “Analysis of Drag Sources in a Fully Submerged Waterjet”. In: *The 9th Conference on Computational Methods in Marine Engineering (Marine 2021)*. Vol. 1. June 2021. DOI: [10.2218/marine2021.6824](https://doi.org/10.2218/marine2021.6824).
- [6] AVANZI, F., DE VANNA, F., RUAN, Y., and BENINI, E. “Design-Assisted of Pitching Aerofoils through Enhanced Identification of Coherent Flow Structures”. In: *Designs* 5(1).11 (2021). DOI: [10.3390/designs5010011](https://doi.org/10.3390/designs5010011).

Other contributions to national and international conferences are hereby reported.

- [1] DE VANNA, F., AVANZI, F., COGO, M., SANDRIN, S., BETTENCOURT, M., PICANO, F., and BENINI, E. “URANOS: an open-source GPU-accelerated Navier-Stokes solver for compressible wall-flows simulations using OpenACC”. In: *34th International Conference on Parallel Computational Fluid Dynamics (ParCFD2023)* (May 29–31, 2023). Cuenca, Ecuador & virtual: University of Cuenca, May 2023.

1. INTRODUCTION

- [2] AVANZI, F. and BENINI, E. "Modeling of water-jet propulsion at the University of Padova". In: *III Giornata di studio sulle Turbomacchine* (July 8, 2022). Bergamo: Università di Bergamo, July 2022.
- [3] AVANZI, F., BENINI, E., RUARO, F., and GOBBO, W. "Design Space Exploration for a Ram Inlet Waterjet for High-Speed Propulsion". In: *International Mechanical Engineering Congress and Exposition (IMECE) 2020* (Nov. 16–19, 2020). Virtual: ASME International, Nov. 2020. DOI: [10.1115/1.0004959v](https://doi.org/10.1115/1.0004959v).
- [4] AVANZI, F., RUAN, Y., and BENINI, E. "Analysis of Dynamic Stall on a Pitching Airfoil With Spectral Proper Orthogonal Decomposition". In: *International Mechanical Engineering Congress and Exposition (IMECE) 2020* (Nov. 16–19, 2020). Virtual: ASME International, Nov. 2020. DOI: [10.1115/1.0004945v](https://doi.org/10.1115/1.0004945v).

2 DESIGN

2.1 Propulsor model

2.1.1 Methods

Drawing inspiration from aeronautical propulsion principles, the proposed system represents a conceptually novel design in the marine domain. To characterise its propulsive performance, the assumptions commonly applied in the analysis of subsonic isolated turbojet engines can be properly adopted. In fact, the generalised thrust theory relies on a list of hypotheses that can be borrowed for the present propulsor without any further modification. First, a cylindrical control volume around the device must be chosen (Fig. 2.1). The latter is conveniently placed with the axis aligned along the advancing direction. The corresponding bases being set, respectively, far upstream and in the neighbourhood of the nozzle exit to consider the exhaust velocity as the one at the discharge section [44]. Thus, additional considerations follow from these assumptions below:

- the fluid is steady, from which continuity equation imposes equality between entering and leaving mass flow rates;
- the flow is uniformly distributed, except for the outlet plane where the processed tube velocity, v_e , is higher than the free stream condition on the remaining annulus.

Furthermore, when using a near-field approach under incompressible hypothesis and in the absence of viscous effects, the actuator disk theory can be applied. According to this approach, the pumping system is replaced with an infinitely thin interface across which a finite pressure jump occurs. Thus, the flow is idealised as the evolution of the stream tube delimited by the stagnation and leaving streamlines and completed by the propulsor internal surface. This processed stream tube results split into two regions, whose fluid dynamic states are governed by the Bernoulli equation, holding upstream and downstream of the discontinuity, separately [105]. As far as the exhaust

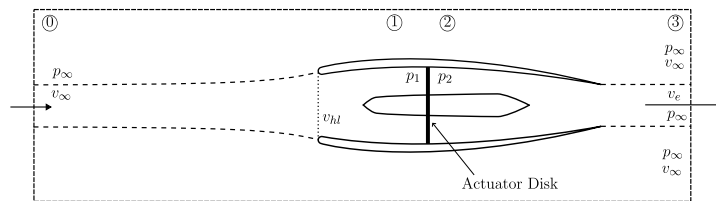


Figure 2.1: Schematic representation of the surrounding control volume and the processed stream tube, adapted from El-Sayed [105].

2. DESIGN

section, the subsonic evolution imposes perfect adaption of the pressure field to ambient conditions. It may be argued that the correct plane to be considered for the free-stream recovery is, generally, the so-called *vena contracta*, a further reduction of the stream tube from the nozzle exit area located downstream of this latter. However, when parallel throat waterjets exhausts are considered as in the present analysis, this additional contraction is such mitigated to be neglected, thus considering the discharge flow as cylindrical [1, 120].

The meanline modelling is thereby discussed. At near-field level, the flow states up to the pump disk, from station ① to ②, can be recovered from the Bernoulli equation. The latter can be written including the intake losses through the Pressure Recovery factor, $PR = p_1^0/p_\infty^0$, where p^0 denotes the total pressure. Thus reading as:

$$p_1 + \frac{1}{2}\rho v_1^2 = PR(X) \left(p_\infty + \frac{1}{2}\rho v_\infty^2 \right) \quad (2.1)$$

where PR is considered as a function of X , which identifies a general variable, depending on the approach adopted to estimate the losses. While a precise prediction is beyond the purposes for the early stage of design, some useful correlations can be used, based both on experimental or numerical reference data. In the first case, one possible solution is to rely on the measurements gathered by McDonald and Fox [86], and later included in McDonald and Fox [85], concerning a tests campaign on the pressure recovery capability of conical shape diffusers. These are categorised based on the relevant geometrical quantities as reported in Figure 2.2 . The latter including: the inlet, $2R_i$, and outlet, $2R_o$, diameters, the divergence angle, 2θ , and the axial length, N [105]. Thus, the pressure recovery coefficient, C_{PR} , is defined as:

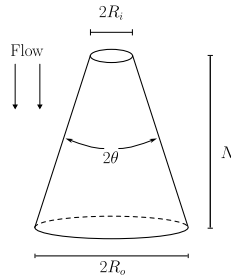


Figure 2.2: Relevant parameters in conical diffusers, adapted from El-Sayed [105].

$$C_{PR} = \frac{2(p_o - p_i)}{\rho v_i^2} \quad (2.2)$$

It is easy to prove that, in the absence of total pressure losses, from Bernoulli equation the pressure rise equals the imbalance of dynamic pressures, which can be related to the cross-sectional areas through imposition of mass conser-

vation. Therefore, the coefficient for an ideal diffuser, $C_{PR,i}$, reads as:

$$C_{PR,i} = 1 - \frac{1}{AR^2} \quad (2.3)$$

$AR = (R_o/R_i)^2$ denoting the inlet to outlet cross-sectional areas ratio. Finally, the total pressure recovery PR can be easily obtained as:

$$PR = 1 - (C_{PR,i} - C_{PR}) \quad (2.4)$$

Now, the ideal coefficient is only dependent on the geometry, while the effective pressure recovery coefficient has to be determined. In this regard, the experiments from McDonald and Fox [86] resulted in a useful chart, reporting the C_{PR} as a function of both the divergence angle and the normalised axial length, N/R_i .

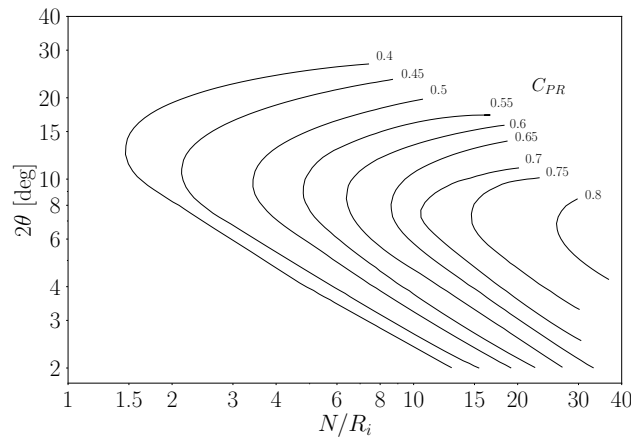


Figure 2.3: Experimental data of pressure recovery coefficient as a function of the divergence angle and normalised cone axial length [86], adapted from El-Sayed [105].

Another alternative is to extract correlations from numerical database. To this end, a function is interpolated on the CFD database described in Section 4.2.2, where an inlet geometry is systematically manipulated and simulated using 2D axisymmetric reduction. Thus, the choice is made to interpolate the pressure recovery as a function of the Inlet Velocity Ratio ($IVR = v_{hl}/v_\infty$). Initially, a second-order polynomial (Fig. 2.4) is considered as an acceptable approximation for the scattered numerical results.

Bringing back the analysis of the flow field, between the pump interfaces (① to ②), the actuator disk theory allows for the definition of the total pressure jump as:

$$p_2 + \frac{1}{2}\rho v_2^2 = \rho gH + p_1 + \frac{1}{2}\rho v_1^2 \quad (2.5)$$

where the head rise, H , is aligned to pressure dimensions through the gravitational acceleration, g , and the fluid density, ρ .

2. DESIGN

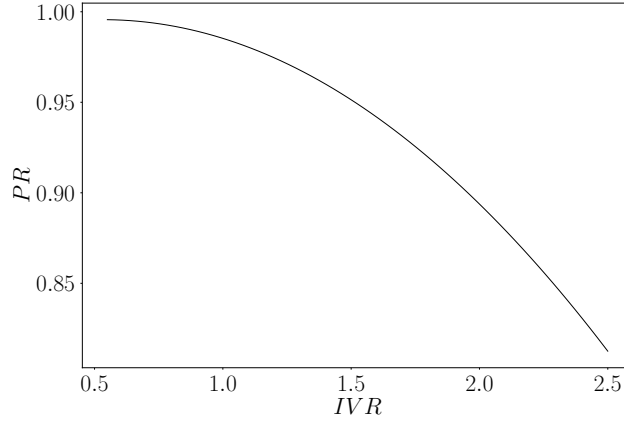


Figure 2.4: Pressure recovery as a function of the IVR , interpolated from the optimisation CFD database obtained in Section 4.2.2 from 2D axisymmetric analysis.

Finally, at the discharge adapted stream tube, Bernoulli equation from station ② to ③ holds as:

$$p_\infty + \frac{1}{2}\rho v_e^2 = \eta_{noz} \left(p_2 + \frac{1}{2}\rho v_2^2 \right) \quad (2.6)$$

where the nozzle efficiency, η_{noz} , is in general high, reaching values up to 1 for well-designed shapes [1].

Thus, the choice is made to adopt non-dimensional quantities. To this end, a normalising group is chosen equal to $\rho(\omega D)^2$, ω and D denoting, respectively, the rotor angular velocity and the characteristic diameter. The preceding equations are orderly re-assessed dividing the corresponding both sides by such factor. As a result, Equation 2.1 is reads as:

$$\frac{p_1}{\rho(\omega D)^2} = PR(X) \left(\frac{p_\infty}{\rho(\omega D)^2} + \frac{1}{2} \frac{v_\infty^2}{(\omega D)^2} \right) - \frac{1}{2} \frac{v_1^2}{(\omega D)^2} \quad (2.7)$$

Now, the left hand side is simply replaced with the non-dimensional pressure, p'_1 . Additionally, the incompressible hypothesis allows for the assumption of $p_\infty = 0$, without loss of generality. Then moving to the free-stream velocity term, further considerations are possible. In fact, multiplying the group by the unitary factor expressed as v_{hl}^2/v_{hl}^2 induces a reformulation which is a function of the highlight velocity and IVR :

$$\frac{v_\infty^2}{(\omega D)^2} = \frac{v_\infty^2}{(\omega D)^2} \cdot \frac{v_{hl}^2}{v_{hl}^2} = \frac{v_{hl}^2}{(\omega D)^2 IVR^2} \quad (2.8)$$

Again, the expression is multiplied by another unitary factor, A_{hl}^2/A_{hl}^2 , $A_{hl} = D_{hl}^2 \pi/4$ being the cross-sectional highlight area defined through the equivalent highlight diameter, D_{hl} . Hence:

$$\frac{v_{hl}^2}{(\omega D)^2 IVR^2} \cdot \frac{A_{hl}^2}{A_{hl}^2} = \frac{Q^2}{(\omega D)^2 IVR^2 \left(\frac{\pi}{4}\right)^2 D_{hl}^4} \quad (2.9)$$

where the volume flow rate (Q) continuity on the processed stream tube is imposed through the equality $Q = v_{hl}A_{hl}$. Then, the turbomachinery flow (φ) and work (ψ) coefficients are here introduced following the definitions explicitly depending on the machine diameter, as:

$$\varphi = \frac{Q}{\omega D^3} \quad (2.10)$$

$$\psi = \frac{gH}{(\omega D)^2} \quad (2.11)$$

This allows for expressing Equation 2.9 as:

$$\frac{Q^2}{(\omega D)^2 IVR^2 \left(\frac{\pi}{4}\right)^2 D^4 \nu_{hl}^4} = \varphi^2 \frac{1}{IVR^2 c_\pi^2 \nu_{hl}^4} \quad (2.12)$$

where two relations are used, respectively: the equivalent-highlight to pump diameter ratio, $\nu_{hl} = D_{hl}/D$, and the constant $c_\pi = \pi/4$. By applying the same procedure to the pump inlet velocity term in Equation 2.7, the latter is finally re-arranged as:

$$p'_1 = PR(X) \frac{\varphi^2}{c_\pi^2 IVR^2 \nu_{hl}^4} - \frac{1}{2} \varphi^2 \frac{1}{c_\pi^2 (1 - \nu_1^2)^2} \quad (2.13)$$

after introducing the concept of pump inlet hub to pump reference diameter ratio, $\nu_1 = D_{h,1}/D$, which induces the pump inlet annulus area computation as $A_1 = (D^2 - D_{h,1}^2)\pi/4$.

The same considerations are extended to the normalised formulations of Equations 2.5-2.6. Thus, omitting algebraic steps, the former is cast as:

$$p'_2 = \psi + p'_1 + \frac{1}{2} \frac{\varphi^2}{c_\pi^2} \left(\frac{1}{(1 - \nu_1^2)^2} - \frac{1}{(1 - \nu_2^2)^2} \right) \quad (2.14)$$

where the pump outlet hub to pump reference diameter ratio, $\nu_2 = D_{h,2}/D$, is used.

While the downstream tube flow is modelled as:

$$p'_2 = \frac{1}{\eta_{noz}} \left(\frac{1}{2} \varphi^2 \frac{1}{c_\pi^2 \nu_e^4} \right) - \frac{1}{2} \varphi^2 \frac{1}{c_\pi^2 (1 - \nu_2^2)^2} \quad (2.15)$$

where $\nu_e = D_e/D$ denotes the equivalent-exit to pump diameter ratio. In conclusion, Equations 2.13-2.14-2.15 define a non-linear system for the three variables: p'_1 , p'_2 , IVR . This implies that the pump characteristic map, $\psi = f(\varphi)$, is known, and so are the geometrical parameters ν , the nozzle efficiency and the pressure recovery law. In this regard, it should be noted that, in case PR is known as a function of IVR , the solution can be conveniently achieved through iterations starting from a set of initial tentative values for the variables.

Conversely, if a method relying on the experiments from [86] is chosen, the pressure recovery results as a constant, once the geometry is fixed, thus reducing the problem to a straightforward linear arrangement. However, in this

2. DESIGN

case additional geometrical information should be provided. In fact, so far the discussed parameters included only cross-sectional quantities. Nevertheless, to extrapolate C_{PR} from the chart in Figure 2.3 it is necessary to know at least one axial dimension. In principle, the diffusion occurs in the propulsor portion extending from the intake throat to the pump interface. However, to resolve the corresponding geometrical parameters, either the axial length between this two stations and the initial contraction ratio should be given. To reduce the decision variables for the design space exploration, on first approximation the diffuser may be identified as an equivalent cone, whose inlet base is the highlight cross-section, while the outlet diameter coincides with the external pump size. Thus, if the non-dimensional intake axial length, $\lambda = N_{int}/D$, is a parameter, the corresponding normalisation by the highlight diameter reads as:

$$\frac{N_{int}}{D_{hl}} = \frac{N_{int}}{D\nu_{hl}} = \frac{\lambda}{\nu_{hl}} \quad (2.16)$$

while the divergence angle is readily obtained as:

$$\theta = \arctan \frac{D - D_{hl}}{N_{int}} = \arctan \frac{1 - \nu_{hl}}{\lambda} \quad (2.17)$$

Finally, the area ratio is computed as:

$$AR = \frac{D^2 - D_{h,1}^2}{D_{hl}^2} = \frac{1 - \nu_1^2}{\nu_{hl}^2} \quad (2.18)$$

The proposed formulation favours an application in optimisation investigations, during which several parameters are looped over to extract a possible design. Conversely, the hydraulic curve within an operating range is not intended as a parametric quantity, therefore a consistent method for a priori estimation, involving a meanline technique, is presented in the next Section.

To this end, performance statistics can be obtained from the model. First of all, the propulsor thrust, T , is computed through integration of the momentum equation over the boundaries of the control volume in Figure 2.1. This yields the common relation adopted for adapted reaction engines [105, 44, 1, 120]:

$$T = \rho Q(v_e - v_\infty) \quad (2.19)$$

Now, the propulsive efficiency is defined as the ratio between the propelling and the jet energy as:

$$\eta_{prop} = \frac{2Tv_\infty}{\rho Q(v_j^2 - v_\infty^2)} \quad (2.20)$$

However, the energy added by the pump can be approximated with that spent in accelerating the jet [1]:

$$\frac{1}{2}\rho Q(v_j^2 - v_\infty^2) = \rho QgH \quad (2.21)$$

thus, the definition of the efficiency here retained is:

$$\eta_{prop} = \frac{T v_{\infty}}{\rho Q g H} \quad (2.22)$$

The latter can be re-arranged once multiplied by the unitary factor $(\omega D)^2/(\omega D)^2$, as follows:

$$\begin{aligned} \eta_{prop} &= \frac{T v_{\infty}}{\rho Q g H} = \frac{\rho Q v_{\infty} (v_e - v_{\infty}) (\omega D)^2}{\rho Q g H (\omega D)^2} = \\ &= \frac{v_{\infty} (v_e - v_{\infty})}{(\omega D)^2} \frac{1}{\psi} = \frac{v_{\infty}^2}{(\omega D)^2} \left(\frac{v_e}{v_{\infty}} - 1 \right) \frac{1}{\psi} = \\ &= \frac{\varphi^2}{IV R^2 c_{\pi}^2 \nu_{hl}^4} \left(\frac{v_e}{v_{\infty}} - 1 \right) \frac{1}{\psi} \end{aligned} \quad (2.23)$$

As regards thrust, the corresponding normalised evaluation, similarly to the aeroengine nomenclature, is the non-dimensional specific thrust [44]:

$$\tilde{T}_s = \frac{T}{\rho Q v_{\infty}} = \frac{\rho Q (v_e - v_{\infty})}{\rho Q v_{\infty}} = \frac{v_e}{v_{\infty}} - 1 \quad (2.24)$$

Thus, both η_{prop} and \tilde{T}_s depend on the ratio between the exit and the advancing velocity. This term can be easily determined once v_e is normalised as:

$$\frac{v_e^2}{(\omega D)^2} = \frac{v_e^2}{(\omega D)^2} \cdot \frac{v_{\infty}^2}{v_{\infty}^2} = \frac{v_e^2}{v_{\infty}^2} \frac{\varphi^2}{IV R^2 c_{\pi}^2 \nu_{hl}^4} \quad (2.25)$$

Finally, introducing Equation 2.25 into normalised Equation 2.6 yields the following:

$$\frac{v_e}{v_{\infty}} = \sqrt{2\eta_{moz} \left(p'_v + \frac{1}{2} \varphi^2 \frac{1}{c_{\pi}^2 (1 - \nu_2^2)^2} \right) \frac{IV R^2 c_{\pi}^2 \nu_{hl}^4}{\varphi^2}} \quad (2.26)$$

The dimensionless nature of the method allows for a general extension to any size and regime, once the pump reference diameter and angular velocity are chosen to retrieve the propulsive statistics in dimensional units.

2.1.2 Results

In the absence of existing measurements for a propulsor as the one here presented, the accuracy on the code is evaluated against the numerical data obtained with a 3D model, integrating the pump within a reference hydrodynamic ram type inlet. Such a model is extensively discussed in Section 3.4, after a thorough validation of the numerical techniques adopted to investigate the corresponding isolated sub-systems. As a consequence, the pump operating map and the geometrical properties to serve as input are taken from that configuration. Both the methods detailed above for estimating the intake pressure recovery are analysed.

2. DESIGN

By comparison of the propulsive statistics (Fig. 2.5), the code demonstrates a great agreement with the available CFD reference, particularly in predicting the non-dimensional specific thrust. It is important to note that, while the CFD solution imposes the advancing velocity as a far-field boundary condition, in the present approach, it results from the system solution since it depends on the unknown IVR according to Equation 2.12. Conversely, the exhaust velocity is fixed by the input flow condition, φ , and the nozzle geometry. The

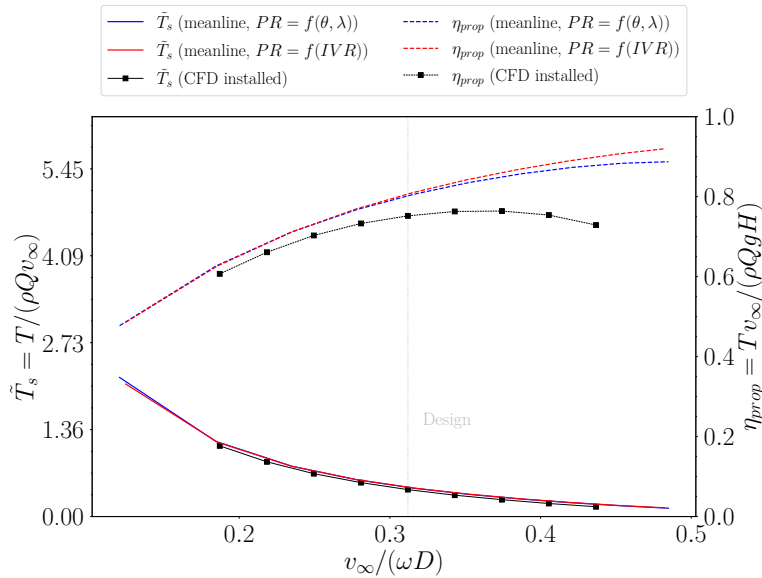


Figure 2.5: Specific thrust \tilde{T}_s and propulsive efficiency η_{prop} as functions of normalised advancing velocity. CFD results from the pump-intake integrated model discussed in Section 3.4 are compared with the present meanline code outcomes. The latter obtained with two different approaches for the inlet pressure recovery estimate: one based on the geometrical correlations from McDonald and Fox [86] and the other relying on the IVR dependency from the 2D axisymmetric database discussed in Section 4.2.2.

results depict no significant dependency on the technique adopted for the treatment of PR .

However, the efficiency curves consistently remain above the CFD data, indicating a tendency for the code to overestimate propulsive performance. The trends reveal that the considered operating range does not cover the peak performance conditions, while the simulations indicate that this point is evidently within the computed cases. The discrepancy between the two approaches increases with advancing velocity, starting from about 2% for the lowest values and reaching around 6.7% at peak conditions. Consequently, the CFD data initiate the performance drop operating phase, while the meanline code still shows an increasing pattern, albeit with a reduced slope. From this operating point, the curves separate faster due to opposite patterns, and even

the two inlet recovery approaches portray different behaviors. In fact, the method based on geometrical parameters flattens earlier than the other, which instead denotes a higher derivative slope.

The shape of the capture stream tube depicts a good agreement with the CFD reference over the entire range (Fig. 2.6). The trend is monotonically decreasing as the free-stream velocity and essentially superimposed with the 3D-installed model curve, especially from the design operating point. Again, the methods adopted for the inlet losses estimation prove equivalent, with a minimal separation of the curves occurring at the lowest advance speeds.

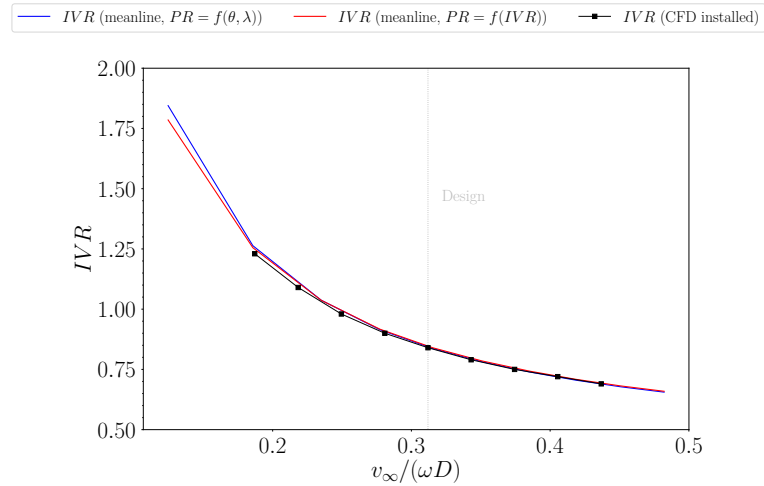


Figure 2.6: IVR as functions of normalised advancing velocity. CFD results from the pump-intake integrated model discussed in Section 3.4 are compared with the present meanline code outcomes. The latter obtained with two different approaches for the inlet pressure recovery estimate: one based on the geometrical correlations from McDonald and Fox [86] and the other relying on the IVR dependency from the 2D axisymmetric database discussed in Section 4.2.2.

2.2 Blade Element Method

To provide a fast tool for initial design steps, the Axial-flow pumps Radial Equilibrium through Streamlines (ARES) meanline solver is implemented as a Python library. The present code relies on continuity and flow momentum conservation equations. The latter, commonly referred to as Radial Equilibrium (RE), is integrated along the Blade Elements (BE), or streamlines, through which the machine meridional channel is discretised. The inclusion of proper correlations for the flow angles and head losses allows for the prediction of the spanwise distribution of the stream quantities at both in- and off-design conditions. As a result, it is possible to estimate the overall performance throughout

2. DESIGN

the operating map. Although the detailed geometry is required for the definition of numerical models or experimental prototypes, to be used for a more accurate evaluation, 1D models are a common choice for preliminary analysis, since they permit the investigation over a wide number of candidates with a much lower time and computational demand [88].

2.2.1 Methods

Assumptions

The solution of governing equations is simplified through the adoption of specific hypotheses on the evolving flow.

- i). the fluid has a constant density, ρ ;
- ii). the flow is assumed at a steady-state, implying that for any variable, $\partial \cdot / \partial t = 0$;
- iii). the solution of flow states is performed at planes perpendicular to the revolution axis, which is aligned along the meridional direction, M (Fig. 2.7). These planes are located downstream of the blade rows and no modelling is provided for the flow evolution within the blades;
- iv). at each plane, the RE is integrated through N_s streamlines, or BE (Fig. 2.7). These are conceived as independent, axisymmetric surfaces of revolution, generated through cylindrical sections of the channel, having the same axis as the machine. The spanwise discretization at the solution stations is iterated through to impose a mass-flow-balanced approach, rather than employing constant radial increments. This strategy enforces continuity within streamtubes, ensuring an equal amount of mass flow rate flowing through each surface, from pump inlet to outlet.
- v). no local viscous effects are modelled. These are instead treated as uniformly lumped at each streamline, through the adoption of empirical correlations detailed further on.

Concerning the stream tubes, the corresponding flow is assumed to be regulated by the blade cascades geometries, which need to be provided as a function of the corresponding radial location following a hub-to-shroud distribution (Fig. 2.7). Thus, at a given streamline section, the schematic of two consecutive blades for a pump stage is depicted in Figure 2.8, where the blades are considered as a spanwise stacking of aerodynamic profiles. Here, α and β denote, respectively, the absolute and relative flow angles, referred to the rotational axis. These angles result from the direction of the corresponding velocities, labelled as c and w . The subscripts 1, 2, 3 identify the corresponding locations of the solution planes. If the reference stage in Figure 2.7 is considered, the indexes can be related to the inlet, mid-stage and outlet stations. Conversely, a subscript b is adopted to refer to the blade metal angles, that is the inclination of the camberline tangent above

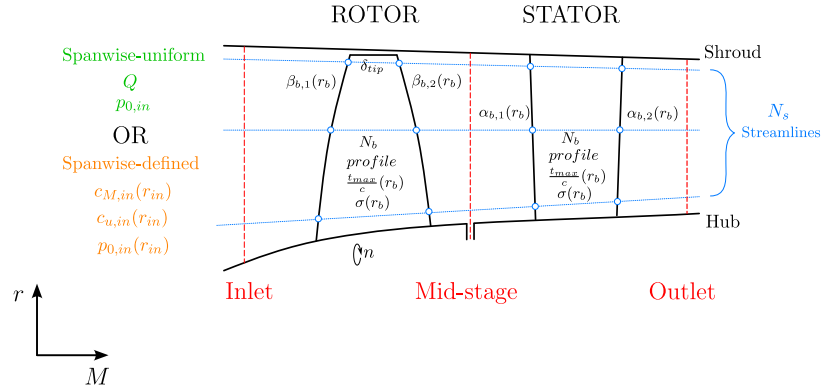


Figure 2.7: Schematic of a pump stage meridional view, including the domain discretisation and the input variables and parameters required by the solver.

the meridional direction, generally required for the leading and trailing edge locations. The difference between these angles and the flow velocity directions is measured with incidence, i , and deviation, δ , respectively for the upstream and downstream evolution. Specifically, the two parameters, e.g., for the rotor blade, are defined as follows:

$$i = \beta_1 - \beta_{b,1} \quad (2.27)$$

$$\delta = \beta_2 - \beta_{b,2} \quad (2.28)$$

Thus, both the absolute and relative flow velocities may be decomposed along the meridional and tangential directions, generating two components respectively differentiated by the subscripts M and u . The latter signifies the direction parallel to the rotational velocity, u . In this way, the typical velocity diagrams, or triangles, result defined by the flow angles and the velocity components.

Additionally, the empirical correlations may require the profile maximum thickness, t_{max} , generally normalised by the chord length, c , which represents the straight line between the leading and trailing edge. Its inclination above the axial direction is the stagger angle, γ . The latter, when circular arc camberline aerofoils are considered, can be directly computed from the metal angles as:

$$\gamma = \frac{\beta_{b,1} + \beta_{b,2}}{2} \quad (2.29)$$

The same relation can be retained when circular arc equivalent formulation is adopted for differently shaped profiles. Conversely, the difference between the two terms yields the profile camber as $\theta = \beta_{b,1} - \beta_{b,2}$. In case a tip clearance exists between blades and casing, the corresponding radial gap is denoted as δ_{tip} .

Finally, the blade solidity, σ , represents another fundamental geometrical parameter. This quantity is defined as the ratio between the chord and the

2. DESIGN

blades pitch, s . The latter representing the distance separating two corresponding points on consecutive blades. It is expressed based on the radial location of the streamsurface, through the number of blades, N_b , as $2\pi r/N_b$.

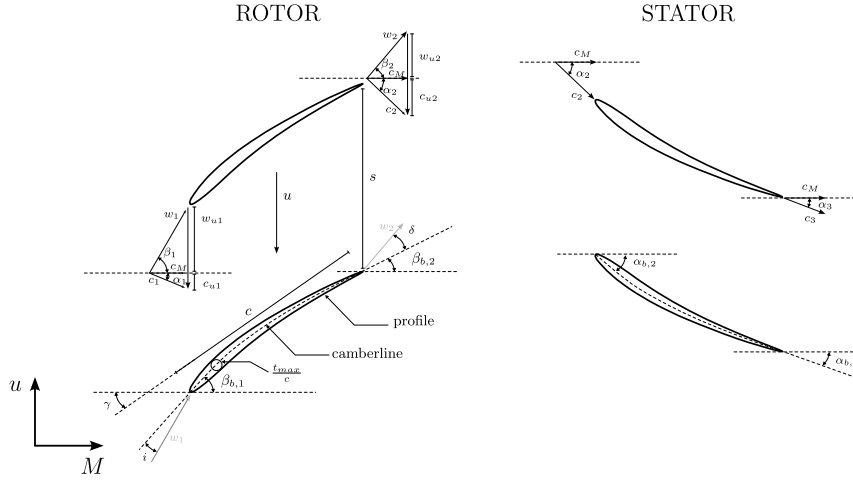


Figure 2.8: Blade geometrical and flow quantities for a sample axial-flow pump stage section.

Governing equations

The flow momentum conservation equation is cast following Serovy et al. [106], who also offer a possible algorithm implementation for its solution, which is similar to the one presented here. In differential formulation, the relation reads as:

$$g \frac{\partial h}{\partial r} = \frac{c_u^2}{r} - c_r \frac{\partial c_r}{\partial r} - c_M \frac{\partial c_r}{\partial M} \quad (2.30)$$

where g is the gravitational acceleration, while h is the static head. The latter is directly linked to the total head, h_0 , by considering the total pressure definition, divided by the factor (ρg) :

$$h_0 = h + \frac{1}{2g}(c_u^2 + c_M^2) \quad (2.31)$$

Now, if Equation 2.31 is differentiated with respect to radius and coupled with Equation 2.30 assuming negligible variations of the velocity radial component, c_r , throughout a computation plane, the resulting equation can be integrated along r . By applying the finite difference approximation from streamline j to $j + 1$, for a chosen solution plane i , the integral is expressed as:

$$\int_{c_{M,j}}^{c_{M,j+1}} c_M dc_M = g \int_{h_{0,j}}^{h_{0,j+1}} dh_0 - \int_{r_j}^{r_{j+1}} \frac{c_u^2}{r} dr - \int_{c_{u,j}}^{c_{u,j+1}} c_u dc_u \quad (2.32)$$

The terms are re-arranged using integration rules and trapezoid approximation for the second term in the right hand side.

Then, two additional laws are considered. One expresses the energy variation between the blades, for any streamline j , as:

$$h_{0,i} = h_{0,i-1} + c_{u,i}u_i - c_{u,i-1}u_{i-1} - h_{0,loss} \quad (2.33)$$

where the ideal total head rise, $\Delta_{i-1 \rightarrow i}(c_u u)$, identically zero for stator blades, is decreased by the total head losses, $h_{0,loss}$. The second equation is the trigonometric relation beneath the velocity diagrams, which, at any station i and streamline j , holds as:

$$c_u = u - c_M \tan(\beta) \quad (2.34)$$

In conclusion, after coupling the integrated formulation with Equations 2.33 and 2.34 and by isolating the variable $c_{M,j+1}$, the following fundamental expression of the RE equation is obtained:

$$Ac_{M,j+1}^2 + Bc_{M,j+1} + C = 0 \quad (2.35)$$

which regulates the downstream meridional velocity for any streamline starting from a reference j . In the previous relation, the coefficients A, B, C are defined as follows:

$$A = 1 + \tan^2(\beta_{j+1}) \left[1 + \frac{r_{j+1} - r_j}{r_{j+1}} \right] \quad (2.36)$$

$$B = -2u_{j+1} \tan(\beta_{j+1}) \frac{r_{j+1} - r_j}{r_{j+1}} \quad (2.37)$$

$$\begin{aligned} C = & -c_{M,j}^2 - 2g(h_{0,j+1}^{(i-1)} - h_{0,j} - h_{0,loss,j+1}) \\ & + 2u_{j+1}^{(i-1)} c_{u,j+1}^{(i-1)} - u_{j+1}^2 \frac{r_j}{r_{j+1}} \\ & + c_{u,j+1}^2 \left(\frac{r_{j+1}}{r_j} - 2 \right) \end{aligned} \quad (2.38)$$

where the quantities are assumed referred to the plane i and the indication is omitted for compactness, unless variables at the upstream measuring station, $i - 1$, are required, in which case they are reported with the corresponding superscript.

Solution of Equation 2.35 yields the c_M distribution along the r locations defined through the j streamlines, once a starting condition at a chosen j_{start} is given. While the information on the upstream plane, $i - 1$, is given by the inflow boundary conditions for the first, computed station, the latter becomes the reference inlet for the second station, and so on. Thus, a multi-rows configuration is solved progressively by advancing from one plane to the next one, without any further intermediate data needed. Therefore, iterations are required for the problem since any variable depends on the radial location. The latter, in turn, is continuously revised until the mass-flow-balanced distribution hypothesis is satisfied.

Although the implementation strategy regarding these steps is detailed in the next paragraph, another important condition justifies the iterative procedure. In fact, the continuity assumption through the stage imposes that, at

2. DESIGN

any computed station, the leaving flow rate equals the inflow value, within a user-defined tolerance. As a result, the meridional velocity spanwise distribution recovered needs to satisfy mass conservation, which is verified at the end of each iteration by numerically expressing the resulting flow rate through quadrature, as:

$$Q_{comp} = \pi \sum_{j=1}^{Ns-1} (c_{M,j+1} + c_{M,j})(r_{j+1}^2 - r_j^2) \quad (2.39)$$

For any further detail on the derivation of the equations the reader is referred to reference literature [106, 98, 97].

Implementation

An input parameter file, containing the mandatory information regarding the case, is initially read by ARES. Listing 2.1 provides an example of the formatted data required by the code to start computations, mixing scalars, arrays and strings. This is divided into 4 main blocks:

- FLUID PROPERTIES
this block contains the information of the working fluid, characterised by density and viscosity;
- GEOMETRY
this section contains all the parameters needed for the geometrical characterisation of blades shapes through the `nStages`. These include: an array gathering the number of blades for each row of each stage, intended as modular succession of rotor+stator; the radial locations at which the metal angles, the solidities and the thickness to chord ratios are defined. These lists are labelled with incremental numbers referring to the incoming and leaving locations for hub-to-shroud distributions of radii and angles, so 1 and 2 denote the leading and trailing edges of the first stage blades, and will become 3 and 4 for a second stage. Conversely, the distributions of σ and t_{max}/c are only labelled according to incremental integers referred to the order of the blades. In addition, the `bladeShape` needs to be chosen between `naca` and `dca`, depending on the definition of the camberline equation. In this regard, the empirical correlations are available for both NACA-65 series curves and Double Circular Arc (DCA). Finally, the `tipGap` for each blade is required for the estimate of tip clearance losses;
- INFLOW & CASE CONDITIONS
this block contains the boundary conditions. Two options are available, once the rotational regime `n` is inserted: either *spanwise-uniform* or *spanwise-defined*. In the first case, the flow rate and total pressure at inlet station are required as scalar values. Then, the code assumes no

pre-swirl entering components and uniformly distribute the meridional component, $c_M = Q/A_{inlet}$, and the input pressure along the span. In the second case, specific distribution of the inflow variables should be prescribed. This implies providing the radial locations where these are defined. For the solution, tangential and meridional velocities and the total head are mandatory.

- SOLUTION

these parameters control how the solver approaches the solution. Specifically, the required quantities are: the number of blade elements, `nStreamLines` (≥ 3), the maximum number of iterations for the radial equilibrium loop and the tolerances for the continuity error and for the BE radial locations and total head losses residuals.

```

+-----+
|PARAMETER UoM      VALUE(S)|
+-----+

FLUID PROPERTIES
=====
rho  [kg/m^3]  : 1000
mu   [Pa s]    : 0.001
=====

GEOMETRY
=====
nStages      : 1
nBladesStation : [27, 27]

rbeta1_hs [m] : [0.04572, 0.052578, 0.066294, 0.08001, 0.093726, 0.107442, 0.1143]
rbeta2_hs [m] : [0.04572, 0.052578, 0.066294, 0.08001, 0.093726, 0.107442, 0.1143]
ralpha1_hs [m] : [0.04572, 0.052578, 0.066294, 0.08001, 0.093726, 0.107442, 0.1143]
ralpha2_hs [m] : [0.04572, 0.052578, 0.066294, 0.08001, 0.093726, 0.107442, 0.1143]

beta1_hs [deg] : [49.5, 55.6, 62.5, 66.4, 69.4, 71.8, 72.8]
beta2_hs [deg] : [-10.7, 11.1, 38.6, 52.4, 60.3, 65.4, 67.5]

alpha1_hs [deg] : [-51.44, -49, -44.3, -40.2, -36.4, -33.1, -31.69]
alpha2_hs [deg] : [10.76, 10.60, 10.90, 11.20, 11.60, 12.20, 12.47]

sigma1_hs : [2.52, 2.19, 1.74, 1.44, 1.23, 1.07, 1.00]
sigma2_hs : [2.34, 2.09, 1.65, 1.36, 1.16, 1.01, 0.96]

tOverc1_hs : [0.1, 0.097, 0.091, 0.085, 0.079, 0.073, 0.073]
tOverc2_hs : [0.08, 0.08, 0.08, 0.08, 0.08, 0.08, 0.08]

bladeShape : dca

tipGap [mm] : [1, 0]
=====

INFLOW & CASE CONDITIONS
=====
n [rpm] : 3910

Spanwise-uniform
-----
Q [m^3/s] :
p0 [Pa] :

Spanwise-defined
-----
r0_hs [m] : [0.04572, 0.04953, 0.0521208, 0.0659892, 0.08001, 0.0940308, 0.1078992, 0.11049, 0.1143]
cm0_hs [m/s] : [16.24584, 16.24584, 16.52016, 16.36776, 16.18488, 15.78864, 15.30096, 14.6304, 14.6304]
cu0_hs [m/s] : [0, 0, 0, 0, 0, 0, 0]
h0_hs [m] : [35.11296, 35.11296, 35.11296, 35.11296, 35.11296, 35.11296, 35.11296, 35.11296, 35.11296]
=====

SOLUTION
=====
nStreamLines : 20

radEqMaxIt : 40
continuityTolerance : 1e-5
rElementsTolerance : 1e-5
hLossTolerance : 1e-5
=====

```

Listing 2.1: Sample of ARES input file.

2. DESIGN

Thus, the code advances following the steps graphically depicted by the flow chart in Figure 2.9 . A brief descriptive discussion follows.

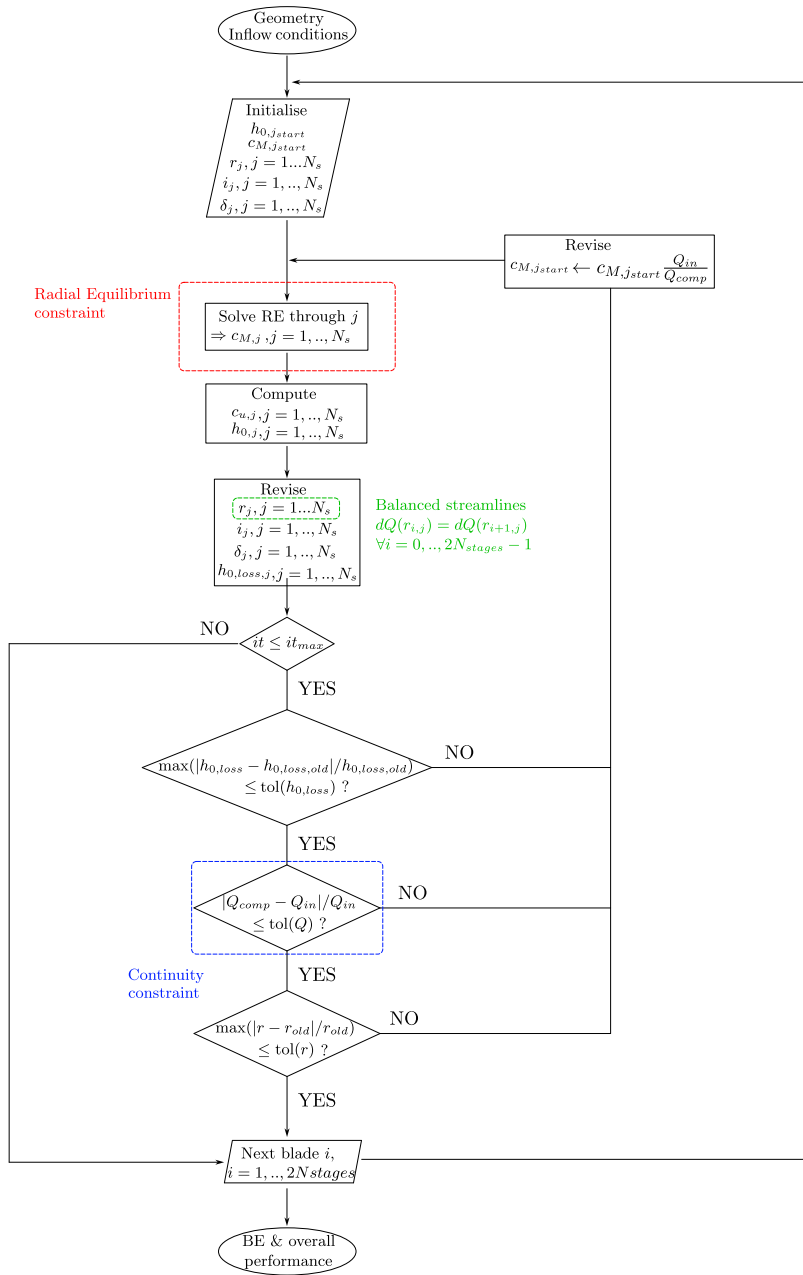


Figure 2.9: Flow chart of ARES meanline solver.

- i). the radial locations at the initial computed plane are initialised at N_s constant radial increments. Thus, a 3-points Lagrange interpolation is adopted to evaluate the geometrical parameters on the newly determined distribution. The inflow conditions distinctively impose the

inflow velocity diagram, through which incidence and deviation can be estimated. The tangential velocity and total head at j_{start} are defined after an initial value for $c_{M,j_{start}}$ is chosen, e.g. equal to the averaged value on the passage.

- ii). radial equilibrium can be solved at any streamline to obtain the meridional velocity component, while simultaneously updating the tangential component and total head state;
- iii). the iteration terminates with the interpolation, applied to compute the new radial distribution. From this information, the values of the blade elements are revised. These including: geometry, incidence, deviation and total head losses according to the correlations detailed further on;
- iv). the code performs the checks required for the stop of iterations. This event occurs always when the maximum allowed number of iterations is reached. Conversely, the relative errors of three statistics are compared with the corresponding chosen tolerance. In addition to the continuity error, identifying the discrepancy between inflow and computed flow rate, the code checks for the residuals of the r and $h_{0,loss}$ arrays from one iteration to the following. In this regard, the maximum criterion is adopted to select a significant scalar value among the streamlines. If any of the three break condition is not satisfied, $c_{M,j_{start}}$ is revised based on the inflow to computed flow rate ratio and iterations continue from step ii);
- v). upon convergence of a blade row, the code advances with either the next row or the conclusion, thus calculating the streamlines and overall performance. These are computed as mass-flow-averaged quantities throughout the blade elements. Finally, the statistics are both printed to screen and saved in Python binary files.

Throughout the code, interpolation tasks are performed using 3-points Lagrange polynomials, while integration operations are computed using the trapezoid rule.

Empirical correlations

So far, the discussion regarding the solution of the flow evolution through the pump relied on the application of general principles, such as mass and momentum conservation, to the duct-flow downstream of the blades rows. However, an accurate prediction of the processes acting on the stream, between the inlet and the outlet sections, must also include the several phenomena occurring within the blades and the influence of the casing.

Concerning the meanline strategy, a well-established technique to address these aspects involves the adoption of empirical correlations [106, 17, 122, 15, 88]. The latter, based on both experimental and numerical datasets, allow for modelling specific flow effects without the need to resolve them. In this

2. DESIGN

regard, the investigations conducted by Lieblein [63] proved pioneering in characterising the blade element behaviour of straight blade cascades, with particular attention to the profile deviation and head losses. However, those studies were limited to inherent 2D flow evolutions. Although subsequent investigations focused on the possibility to capture the actual 3D nature of machinery vanes flows, the current state of meanline approaches is necessarily tied to the calibration using high order analyses [66].

Inside ARES, the impact of leaving stream deviation and several loss sources are taken into account. In this regard, the latter are here defined as:

$$h_{0,loss} = \bar{\omega} \frac{w_1^2}{2g} \quad (2.40)$$

where the total pressure loss coefficient, $\bar{\omega}$, is converted into head losses dimensions through the inflow relative velocity. Different correlations have been developed for the term $\bar{\omega}$. Among them, the ones retained for the present analysis contribute to define the overall coefficient as:

$$\bar{\omega} = \bar{\omega}_{pro} + \bar{\omega}_{sec} + \bar{\omega}_{tip} + \bar{\omega}_{EWBL} \quad (2.41)$$

which includes, respectively, profile shapes total head drop, secondary flows effects, tip clearance leakage, and End Wall Boundary Layer (EWBL) losses. Specifically, the former represents the predominant source and it is assumed to depend on the incidence angle distance to the optimal value, i^* , according to the following relation:

$$\bar{\omega}_{pro} = \bar{\omega}_{pro}^* f(i - i^*) \quad (2.42)$$

where, again, subscript * is used to denote the profile losses at minimum loss incidence. This parameter is important also for the deviation prediction, since the off-design value, $\delta_{2D,off}$, results as a modification of the minimum loss deviation, δ^* , through the term $(i - i^*)$.

A list of the implemented correlations follows.

- Minimum loss incidence

This value is modelled according to the observations made by Lieblein [63]. The extensive analysis on 2D low-speed compressor cascades allowed for the definition of the incidence angle corresponding to minimum losses for NACA-65 series profiles. The relation, including blade geometry parameters, is given as:

$$i^* = K_{sh} K_{i,t} i_{0,10} + \tilde{n} \theta \quad (2.43)$$

Possible correlations of the terms in the previous equation have been proposed by Aungier [8], based on the experiments presented in Johnson and Bullock [63]. The expression essentially reads as a linear correlation, with the intercept depending on the reference incidence for a zero-camber,

65-series 10% thickness distribution aerofoil, $i_{0,10}$, which depends on the inflow angle and profile solidity, as follows:

$$i_{0,10} = \frac{\beta_1^{0.914 + \frac{\sigma^3}{160}}}{5 + 46 \exp(-2.3\sigma)} - 0.1\sigma^3 \exp\left(\frac{\beta_1 - 70}{4}\right) \quad (2.44)$$

Thus, the shape constant, $K_{i,sh}$, is defined based on the profile camberline, assuming values 1 and 0.7 respectively for NACA and DCA outlines. While the thickness parameter, $K_{i,t}$, is correlated as:

$$K_{i,t} = \left(10 \frac{t_{max}}{c}\right)^{\frac{0.28}{0.1 + \frac{t_{max}}{c} 0.3}} \quad (2.45)$$

Finally, the minimum loss incidence results regulated by the profile camber, θ , through the slope, \tilde{n} , which reads as:

$$\tilde{n} = 0.025\sigma - 0.06 - \frac{\left(\frac{\beta_1}{90}\right)^{1+1.2\sigma}}{1.5 + 0.43\sigma} \quad (2.46)$$

- Deviation

The reference data are taken from Lieblein [63] even for this parameter, by taking advantage of the correlations provided by Aungier [8]. At minimum loss conditions, the deviation, δ^* , can be expressed in terms of geometrical and flow quantities as:

$$\delta^* = K_{sh} K_{\delta,t} \delta_{0,10} + \tilde{m} \theta \quad (2.47)$$

Here, the reference deviation for a zero-camber, 65-series 10% thickness distribution aerofoil, $\delta_{0,10}$, is given as:

$$\delta_{0,10} = 0.01\sigma\beta_1 + (0.74\sigma^{1.9} + 3\sigma) \left(\frac{\beta_1}{90}\right)^{1.67+1.09\sigma} \quad (2.48)$$

Additionally, while K_{sh} is the same that presented for the reference incidence relation, the thickness coefficient, $K_{\delta,t}$ is expressed as:

$$K_{\delta,t} = 6.25 \frac{t_{max}}{c} + 37.5 \left(\frac{t_{max}}{c}\right)^2 \quad (2.49)$$

Concerning the linear correlation slope, \tilde{m} , the following equation holds:

$$\tilde{m} = \frac{0.17 - 0.0333 \frac{\beta_1}{100} + 0.333 \left(\frac{\beta_1}{100}\right)^2}{\sigma^{0.9625 - 0.17 \frac{\beta_1}{100} - 0.85 \left(\frac{\beta_1}{100}\right)^3}} \quad (2.50)$$

Thus, the off-design prediction implements the model proposed by Dongrun et al. [41]. The method stems from a simplified definition of a blade cascade lift profile [40], C_L , to define the following intermediate, implicit function of δ :

$$f(\delta) = C_L = \frac{2}{\sigma} \cos(\beta_m) [\tan(\beta_{b,1} + i) - \tan(\beta_{b,2} + \delta)] \quad (2.51)$$

2. DESIGN

with β_m denoting the mean flow angle, expressed as:

$$\beta_m = \arctan \left[\frac{\tan(\beta_{b,1} + i) + \tan(\beta_{b,2} + \delta)}{2} \right] \quad (2.52)$$

Then, the incidence dependency is included in the following relation:

$$f(\delta) = \frac{df(\delta)}{di} (i - i^*) + f(\delta^*) \quad (2.53)$$

where the derivative is further expanded as:

$$\frac{df(\delta)}{di} = \frac{\partial f(\delta)}{\partial i} + \frac{\partial f(\delta)}{\partial \delta} \frac{\partial \delta}{\partial i} \quad (2.54)$$

Here, the reader is referred to the reference literature for an extensive treatment of the terms included in Equation 2.54 [40, 41]. However, a non-linear scheme is necessary for the solution of the latter. The method implementation allows for estimating the derivative with a $< 10^{-8}$ residuals accuracy within 20 inner iterations. The value is then introduced into Equation 2.53. Thus, the result can be employed for the computation of $\delta_{2D,off}$, by inverting the definition given in Equation 2.51. The estimate for the deviation angle takes into account two additional effects. In fact, Robbins et al., in a work collected in Johnson and Bullock [63], recognised the influence of 3D flow evolution, which modifies the original correlations derived by Lieblein from planar cascades measurements, especially far from the mid-span. From the tables obtained within rotor test campaign, a 3D correction for δ , at low speed conditions, can be retrieved as a function of the normalised span of the blade element, the latter defined as $b = (r_{BE} - r_{hub}) / (r_{tip} - r_{hub})$, where the denominator coincides with the blade height, h_b . Incompressible data extracted from the charts of Robbins et al. [63] are reported in Figure 2.10 .

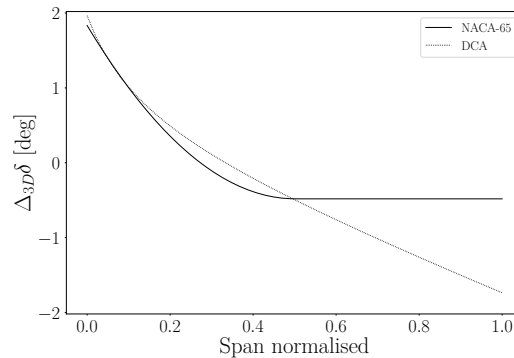


Figure 2.10: Three-dimensional effects correction on the predicted δ . Data extracted from Robbins et al. in Johnson and Bullock [63].

Thus, a further correction is introduced to account for the Axial Velocity Ratio (AVR) between the blades. The correlation, taken from Pollard and

Gostelow [101], is expressed as follows:

$$\Delta_{AVR}\delta = 10 \left(1 - \frac{c_{M,2}}{c_{M,1}} \right) \quad (2.55)$$

In conclusion, the deviation angle results as the simultaneous contribution of off-design profile behaviour, three dimensional and AVR effects, as:

$$\delta = \delta_{2D,off} + \Delta_{3D}\delta + \Delta_{AVR}\delta \quad (2.56)$$

- Profile losses

This loss source was initially modelled by Lieblein in Johnson and Bullock [63] for minimum loss conditions, as:

$$\bar{\omega}_{pro}^* = 2 \frac{\tilde{\theta}_2}{c} \frac{\sigma}{\cos \beta_2} \left(\frac{\cos \beta_1}{\cos \beta_2} \right)^2 \left(\frac{2H_{TE}}{3H_{TE} - 1} \right) \left[1 - \frac{\tilde{\theta}_2}{c} \frac{\sigma H_{TE}}{\cos \beta_2} \right]^{-3} \quad (2.57)$$

where boundary layer development is included through the wake momentum thickness, $\tilde{\theta}_2$, and the wake form factor, H_{TE} , denoting the ratio between the displacement and the momentum thickness. A well-known formulation of these two terms is the one provided by Koch and Smith [67]. Their improved arrangement resumes the original dependency on the equivalent diffusion factor (or diffusion ratio), $D_{eq} = w_{max}/w_2$, proposed by Lieblein. Thus, additional, influencing factors are recognised as fundamental and, therefore, added in the correlations. Specifically, these include: blade-chord Reynolds number, $Re_{1c} = \rho w_1 c / \mu$, blade cascades area contraction, blade geometry and compressibility effects (not effective here). A comprehensive list of equations is drawn and closure constants are empirically determined. For the sake of conciseness these are not reported here, but the reader can easily find them in the programmatic work [67], as well as in Tournier and El-Genk [122].

Once the minimum loss coefficient is computed, the off-design profile value can be determined according to Aungier [8], as:

$$\bar{\omega}_{pro} = \bar{\omega}_{pro}^* f(\xi) \quad (2.58)$$

where ξ is a parameter quantifying the normalised incidence, with respect to the positive, i_p , and negative, i_n , stall angles of attack. These are taken from the NACA-65 test campaign by Herrig et al. [56], and respectively modelled by Aungier [8] as:

$$i_p - i^* = 10.3 + \left(2.92 - \frac{\beta_{b,1} + i_p}{15.6} \right) \frac{\theta}{8.2} \quad (2.59)$$

$$i_n - i^* = -9 + \left[\left(1 - \frac{30}{\beta_{b,1} + i_n} \right)^{0.48} \right] \frac{\theta}{4.176} \quad (2.60)$$

Solution of Equations 2.59 requires a non-linear procedure. Thus, after i_p and i_n are known, ξ and $f(\xi)$ can be computed and off-design loss

2. DESIGN

coefficient is obtained from Equation 2.58. For details on the relations for ξ and $f(\xi)$ the reader is referred to Aungier [8].

- Secondary losses

Modelling of secondary flows, especially those responsible for trailing edge vortices, was addressed by Howell [58]. The same approach is used in Tournier and El-Genk [122], where the following correlation is reported:

$$\bar{\omega}_{sec} = 0.018\sigma \frac{(\cos \beta_1)^2}{(\cos \beta_m)^3} C_L^2 \quad (2.61)$$

- Tip leakage losses

The reference model for this loss source is the approach of Denton [39], as more recently formulated by Banjac et al. [16]. The total pressure drop is ascribed to the overall entropy production, $T\Delta S$, associated to the local mass flow rate flowing through the tip gap, which can be related to the pressure drop between the blade pressure and suction sides, as:

$$d\dot{m} = C_c \delta_{tip} c \sqrt{2\rho\Delta p} \cos \gamma d\bar{x} \quad (2.62)$$

where the constant C_c is considered equal to 0.79 as suggested in Banjac et al. [16], while \bar{x} denotes the local coordinate along the chord, ranging from 0 at the leading edge to 1 at the trailing edge. Thus, the loss coefficient reads as:

$$\bar{\omega}_{tip} = \frac{2N_b T \Delta S}{w_1^2 \rho Q} \quad (2.63)$$

Here, the overall entropy is computed through the following integral:

$$\begin{aligned} T\Delta S = & C_c \delta_{tip} c \cos \gamma \int_0^1 \sqrt{2\rho\Delta p} w_s (w_s - w_p) d\bar{x} \\ & C_c \delta_{tip} c \cos \gamma \rho \int_0^1 \sqrt{w_s^2 - w_p^2} w_s (w_s - w_p) d\bar{x} \end{aligned} \quad (2.64)$$

where Bernoulli equation is used to relate the static pressure drop to the kinetic energy drop from the pressure, w_p , to the suction, w_s , sides. The corresponding velocities are assumed to follow a linear variation along the chord position, which is regulated according to the diffusion ratio derived from Lieblein [63]. These expressions can be found in full formulation in Banjac et al. [16].

Thus, the integration of Equation 2.64 is efficiently performed using the trapezoid rule over the interval $[0, 1]$, discretised into 20 steps. However, it should be noted that the theory applies to the tip BE. As a consequence, the loss coefficient results as a lumped quantity instead of a spanwise distribution, as in the other cases. If in principle the leakage losses affect only the vicinity of the clearance region, this may represent a problem for the numerical scheme. In fact, as pointed out by Aungier [8], in real machines the several flow phenomena result mixed downstream of each blade row, which effect is not included a priori on conventional meanline

codes. As a consequence, the losses may accumulate on a single streamline from station to station, until a possible divergence of the numerical solution. The approach retained by Aungier [8] implies a linear distribution of the lumped value obtained from Equation 2.63, in such a way that at the hub the tip leakage losses are 0, while the sum of the spanwise loss fractions yields again the computed $\bar{\omega}_{tip}$. In the present work, the loss coefficient is re-distributed using the same method.

- EWBL losses

The detrimental effects of the casing boundary layer are included following the formulation of Aungier [8], derived from Howell [58]. As reported by Tournier and El-Genk [122], the following correlation holds:

$$\bar{\omega}_{EWBL} = 0.0146 \frac{c}{h_b} \left(\frac{\cos \beta_1}{\cos \beta_2} \right)^2 \quad (2.65)$$

A summary of the empirical correlations is reported in Table 2.1 along with the corresponding reference.

Table 2.1: Summary of the empirical correlations implemented.

Parameter	Symbol	Reference
Reference incidence	i^*	Lieblein [63]
Reference deviation	δ^*	Lieblein [63], Aungier [8]
Deviation	δ	Dong-run et al. [40], Dongrun et al. [41], Robbins et al. [63], Pol-lard and Gostelow [101]
Profile losses	$\bar{\omega}_{pro}$	Lieblein [63], Koch and Smith [67], Aungier [8]
Secondary losses	$\bar{\omega}_{sec}$	Howell [58]
Tip leakage losses	$\bar{\omega}_{tip}$	Banjac et al. [16], Denton [39]
EWBL losses	$\bar{\omega}_{EWBL}$	Tournier and El-Genk [122]

2.2.2 Results

The accuracy of the presented method is assessed through comparison with available experimental data of three axial flow pumps for different installations. The main geometrical and flow properties of the machines are reported in Table 2.2.

The discretisation of passages remains consistent across all test cases, adopting a fixed number of streamlines, $N_s = 21$. Although the analysis is tailored to each individual machine based on boundary conditions replicating measurement configurations, a unified solver setup demonstrates convergence regardless of the specific problem addressed. Specifically, a maximum number of 40 iterations is allowed. However, solutions demonstrate that when the

2. DESIGN

Table 2.2: Main parameters of the test cases adopted for the validation of ARES.

Parameter	R02 [†] [94]	HIREP [†] [134]	AxWJ-2 [‡] [92]
Blades number, N_b	16	7	6 – 8
Profile	DCA	DCA	NACA
Hub radius, r_{hub} [mm]	45.7	266.7	46.3 – 79.8
Tip radius, r_{tip} [mm]	114.3	533.3	152.4 – 127.7
Hub solidity, σ_{hub}	2.11	1.19	1.88 – 2.43
Tip solidity, σ_{tip}	0.84	0.56	1.72 – 0.97
Tip gap, δ_{tip} [mm]	0.5	3.3	0.5 – 0
Rotor speed, n [rpm]	~ 3918.6	260	1400
Tip Reynolds number, Re_{1c}	$2.15 \cdot 10^6$	$5.5 \cdot 10^6$	$5.36 \cdot 10^6$
Flow coefficient [§] , φ	0.387	0.216	0.135

[†] Rotor only

[‡] Rotor and stator blades data

[§] Computed at design using Equation 2.10 for comparison

solver completes the computation successfully, all the three relative errors criteria are satisfied within a maximum number of 25 iterations. The stop conditions being $1 \cdot 10^{-5}$ for either the continuity error and the BE radius and head losses residuals.

An illustrative representation of the convergence profiles for a near-design solution is reported in Figure 2.11 . Despite minimal fluctuations depicted

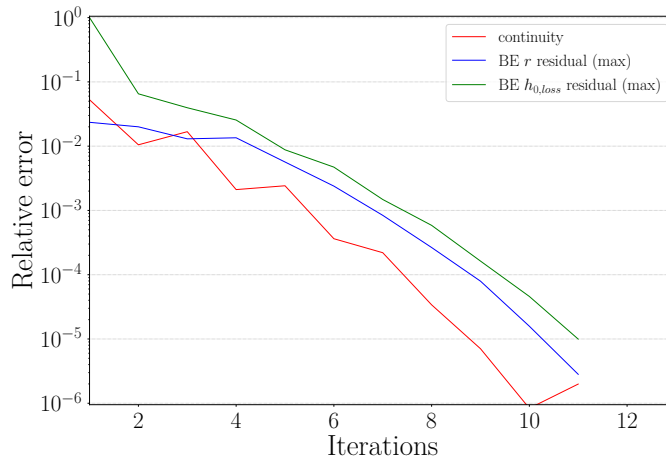


Figure 2.11: Example of convergence profiles throughout the iterations history of a single point computation.

by the continuity curve, the residuals trends maintain a smooth decreasing

behaviour throughout the 11 iterations. As far as the discretisation sensitivity, Figure 2.12 reports the relative error between measured and computed torque coefficient of the HIREP [134], operating at design conditions, as a function of the streamlines number. A minimum number of 3 is required for the 3-point Lagrange approximation, hence N_s is progressively doubled up to 96 BE. The plot confirms that increasing the number beyond 12 yields no significant improvements in the prediction. The chosen number for the subsequent analyses lies well within the mesh independency range and is not unduly exaggerated.

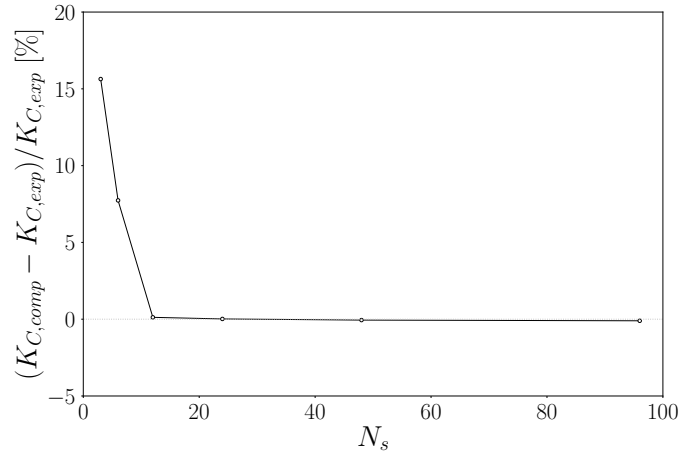


Figure 2.12: Grid dependency analysis taken from the design condition simulation of HIREP [134]. Torque coefficient error is computed relative to the experimental value and plotted as a function of the discretisation, N_s .

The results are presented on a case-by-case basis below. To maintain consistency with the original reference conventions, the various quantities introduced are defined according to the respective publications, and the expressions will be explicitly reported throughout the discussions.

NASA Rotor 02

This straight-duct rotor is part of an extensive experimental campaign, whose results are made available as blade element quantities by Miller et al. [94]. The geometry reflects the characteristic features of an initial pump stage, commonly located downstream of an inducer. It arises as a modification of a prior design [30, 93].

Inflow boundary conditions are extracted from the reference document [94] at the spanwise locations corresponding to the measurements. Based on these, 8 flow configurations are reported from experiments. The latter encompassing operations over a range of flow coefficients, $\varphi = Q/(A_{annulus}u_{tip})$, from 0.262 to 0.337. As a result, the input parameter file is filled with spanwise-defined conditions, which means that the inlet values of c_M , c_u and h_0 are provided

2. DESIGN

as a function of the radial coordinate, depending on the flow configuration.

The resulting map, depicting the work coefficient and the overall efficiency as functions of the flow coefficient, is reported in Figure 2.13. The latter respectively defined as $\psi = (gH)/u_{tip}^2$ and $\eta = H/H_{id}$, where the ideal head rise reads as $H_{id} = (c_{u,2}u_2 - c_{u,1}u_1)/g$. Here, only 6 out of 8 flow configurations are retained for the discussion, thus rejecting the ones at the lowest φ . Specifically, configuration 7 generates a solution. Though, this is not successfully converged within 40 iterations. As regards configuration 8, the first operating point on the left of the map, the code shows divergence as reversed flow arises at some streamlines. This condition is determined by the computation of two negative c_M solutions for Equation 2.35. The results portray a quite smooth

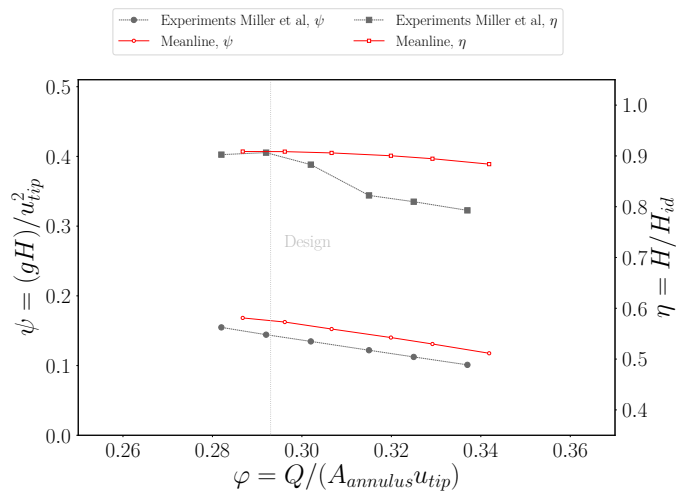


Figure 2.13: Overall work coefficient and efficiency as functions of the flow rate coefficient for the NASA Rotor 02, comparing ARES solution and experimental values from Miller et al. [94].

trend throughout the simulated points. This induces a significant similarity of the ψ curves. However, a nearly constant vertical shift, $\Delta\psi = 0.13 \div 0.17$, suggests a tendency of the code to overestimate the pressure rise capability of the rotor, especially at the highest flow coefficients. A similar consideration may hold for the efficiency prediction. However, the discrepancy for this statistics reach a peak over 9%, while near design conditions the accuracy reach a significant order of 0.2%. The code proves to miss the abrupt efficiency drop just after design conditions, as resulting from measurements. Thus, the smooth trend recovered by the meanline method induces the great separation at the farthest right operating points.

Comparisons between the spanwise distributions of flow quantities downstream of the rotor and experimental data are conducted to assess local accuracy. In configuration 1 ($\varphi = 0.337$), the rotor operates with a flow coefficient exceeding the design value (Fig. 2.14). The tangential component closely

aligns with measurements across the majority of the span, deviating notably only near the 70%. Conversely, the meridional component exhibits clear underestimation, with a substantial discrepancy increasing in the central region of the blade but diminishing towards the extremes. Regarding the relative flow angle, the two curves are nearly superimposed, indicating a high predictive capability (Fig. 2.14b). A slight deviation of $\sim 1^\circ$ is observed starting from around span 30%, decreasing towards the tip. This trend is driven by velocity behaviours; up to this radial location, the tangential component demonstrates substantial agreement, while the meridional one displays an increasing discrepancy. Near mid-span, the meridional component reaches its maximum deviation from the experiments. Then, it gradually approaches measurements while consistently staying below them. Conversely, the tangential component begins to deviate towards higher values. This effect compensates for the underprediction of c_M , thus bringing the β_2 curve back within the experimental range.

Differently, the pressure rise estimate is stably and considerably overestimated (Fig. 2.14c). While at lower spans the trend is similar to the experiments and the deviation remains around $\Delta c_{p0} = 0.2$, starting from approximately 40% of the blade height the total head losses are significantly underpredicted. The code demonstrates difficulty in predicting the flow evolution in the upper half. Specifically, the pressure rise remains almost constant, thus missing the linear decrement obtained from measurements. This aspect also justifies the overprediction of the BE efficiency across the entire span (Fig. 2.14d). However, the effects here appear mitigated. The uniform trend is almost replicated from experiments, thus keeping the discrepancy around an average value of +5.5%, except at the mid-span. Here, in fact, the meanline approach misses the measured bend, which generates a local deviation up to +8%.

Configuration 5 ($\varphi = 0.292$) is taken as representative of near-design operations (Fig. 2.15). In this regard, when incidence angles are within a range of optimal values, the overall efficiency showed the best agreement. The local analysis of the velocities distributions depicts a significant improvement in the meridional component prediction (Fig. 2.15a), even though the central part of the blade still exhibits a tendency toward an underestimation. Conversely, c_u overprediction results enhanced if compared with the previous outcomes, but the greater accuracy on the lower half appears confirmed. The combined effect of the two computed components is again drawn by inspection of the relative flow angle (Fig. 2.15b). For this flow configuration the computed solution portrays an impressive agreement with the experimental curve, except for a minor deviation around span 10%. Anyhow, this results from the interaction between the under- and over-prediction of the velocities components, thus an isolated analysis of β_2 may induce to misleading conclusions on the accuracy.

As regards the pressure field, the general tendency to overestimate the head rise is further confirmed (Fig. 2.15c). In fact, although the trend in this

2. DESIGN

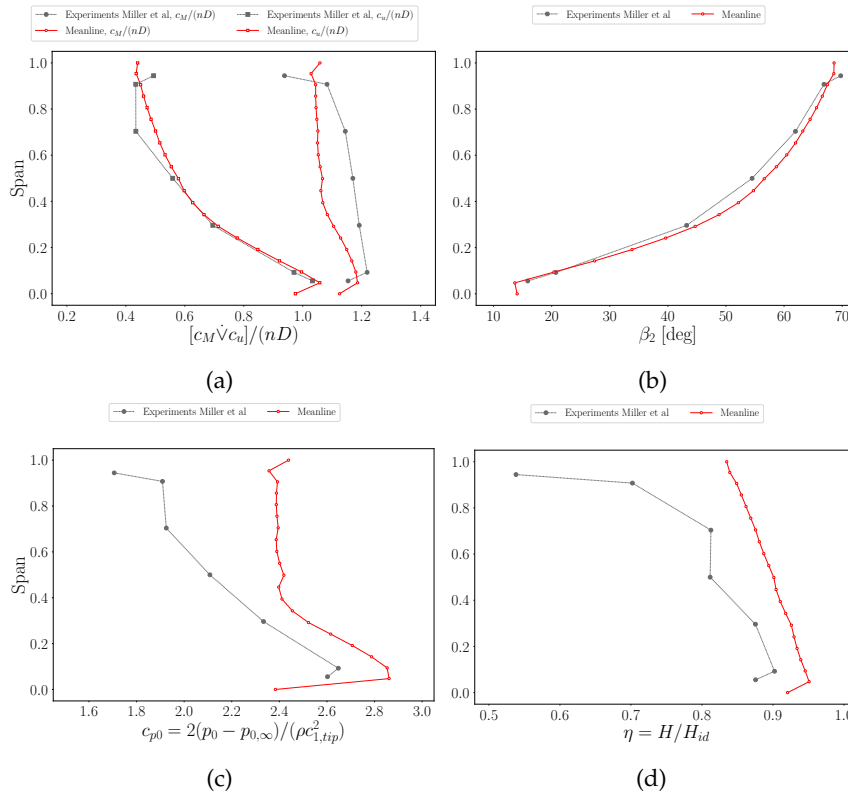


Figure 2.14: Spanwise distribution of the flow statistics, comparing ARES solution and experiments from Miller et al. [94], downstream of the NASA Rotor 02, for flow configuration 1 ($\varphi = 0.337$). Reported quantities include: normalised tangential and axial velocities (a), relative angle (b), total pressure coefficient (c) and BE efficiency (d).

case resembles the one from measurements, the right shift denotes a stable overestimation, which is on average around $\Delta c_{p0} = 0.5$. On the opposite, the BE efficiency curve is significantly improved (Fig. 2.15d). The two curves interscate, which suggests that for some locations there exists high punctual accuracy. Despite a maximum deviation of about -5.5% at span 70%, the computed solution portrays overprediction around the same order even in the vicinity of hub and tip regions. This favours a mitigation of the discrepancies during spanwise integration, thus leading to a high similarity between the overall statistics.

HIREP

The High REynolds number Pump (HIREP) facility was employed to conduct experiments on the effects of an Inlet Guide Vane (IGV) when placed ahead of a rotor [134, 133]. Measurements were taken downstream of both the IGV and the straight-duct rotor. Specifically, the data from the first station are

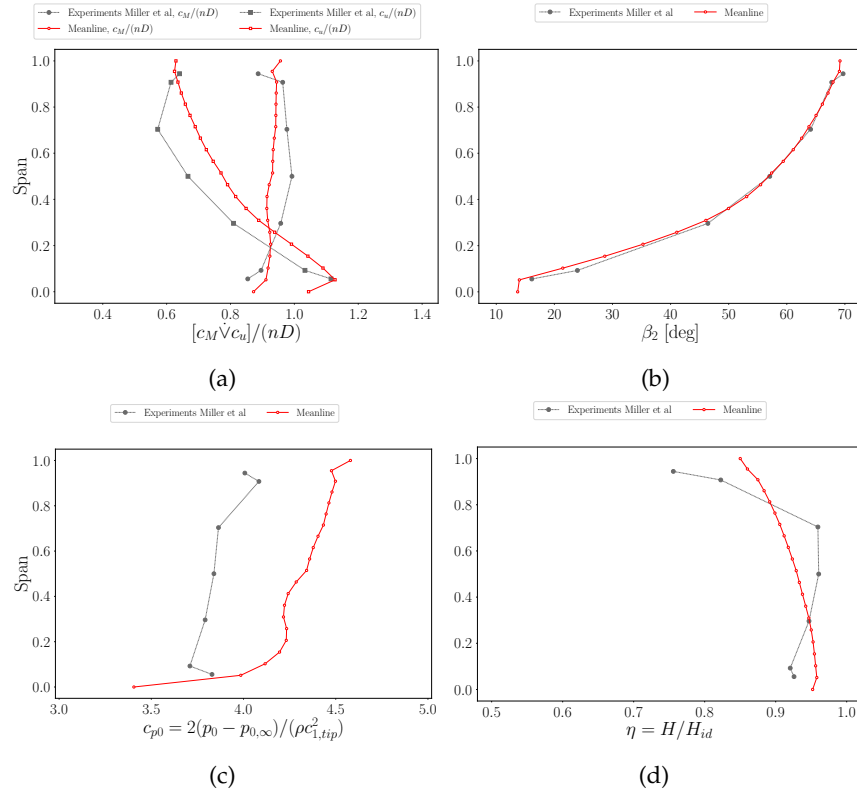


Figure 2.15: Spanwise distribution of the flow statistics, comparing ARES solution and experiments from Miller et al. [94], downstream of the NASA Rotor 02, for flow configuration 5 ($\varphi = 0.292$). Reported quantities include: normalised tangential and axial velocities (a), relative angle (b), total pressure coefficient (c) and efficiency (d).

retained and adopted here as inflow, spanwise-defined boundary conditions (Fig. 2.16). This allows for testing the code under non-uniform entering flow conditions. Although the meridional velocity distributions were in general non-uniform even for the NASA R02, the stream at the inlet was assumed with no tangential components in the reports [94]. In this case, the presence of the upstream IGV necessarily adds pre-swirl to the mass flow rate reaching the rotor. As a consequence, the rotating blades processes an accelerated entering flow, characterised by positive c_u components. Thus, 7 points are selected to sample the tests database. Hence, the corresponding values of the tangential and axial velocity (Fig. 2.16a) and total pressure (Fig. 2.16b) are extracted and used as input for the ARES parameter file. It should be noted that, in the absence of measured quantities at the hub, to let the code solve the entire passage height, the last sampled flow statistics near the root are assumed copied at span 0.

The analysis of the integral statistics focuses on the behaviour of the torque

2. DESIGN

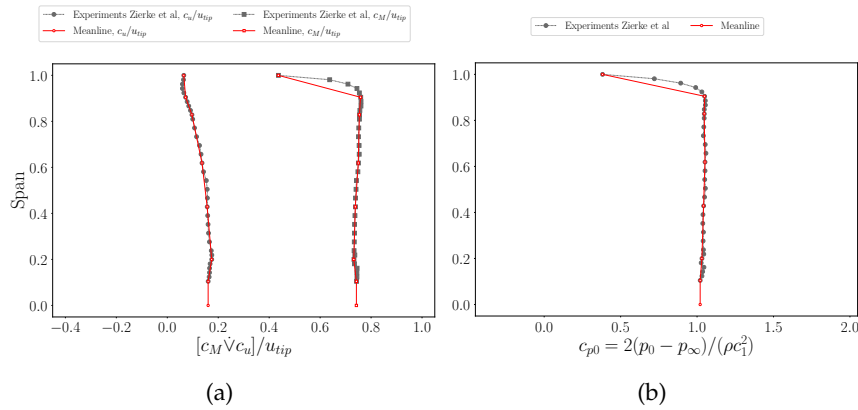


Figure 2.16: Spanwise distribution of the flow statistics downstream of the HIREP IGV under design conditions. The values from Zierke et al. [134] are sampled and retained as inflow boundary conditions for simulation of the rotor flow with ARES.

coefficient, K_C , as a function of the flow rate coefficient (Fig. 2.17). The definitions for the two parameters, as given in the reference study [134], respectively hold as:

$$K_C = \frac{C}{\rho n^2 D^5} \quad (2.66)$$

$$\varphi = \frac{Q}{n D^3} \quad (2.67)$$

C denoting the shaft torque.

In reproducing the operating map, the inflow boundary conditions are maintained as depicted for the design point ($\varphi = 1.36$) in Figure 2.16. Thus, only the rotor speed, n , is varied from 228 to 292 *rpm*, which corresponds to a range of flow coefficients between 1.2 and 1.54. As φ is modified, local variations of the flow variables are expected downstream of the IGV, with a particular influence on the total pressure spanwise distribution. However, the rotor inflow quantities, specific for each operating point, are not provided inside the tests data set and assuming them unaltered is necessary to investigate the off-design study. The results confirm a significant accuracy regarding the prediction of overall performance at near-design conditions. Conversely, the meanline method demonstrates a noticeable tendency to delay the statistics drop at lower flow coefficients while emphasising non-optimal operations at conditions exceeding the design point. Here, the underprediction is as low as $\Delta K_C = -0.07$. For the design point, spanwise distributions of the velocity and pressure fields are included in the measurements database, thus allowing for a local accuracy assessment (Fig. 2.18). Both the tangential and axial components of the predicted absolute velocity depict a consistent proximity to the experimental curves (Fig. 2.18). Specifically, not only are the profiles recovered

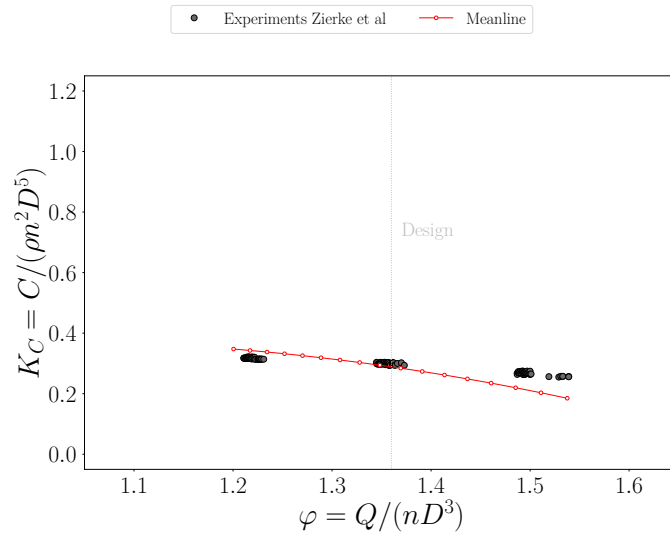


Figure 2.17: Overall torque coefficient as a function of the flow rate coefficient for the HIREP rotor, comparing ARES solution and experimental values from Zierke et al. [134].

with significant agreement, but the deviations are also limited. By inspection of the numerical solution, the code portrays an over-turning of the inflow c_u components, thus resulting in negative velocities. This contrasts with the real rotor, which instead generates an almost rectified flow. Consequently, the augmented magnitude of the tangential component induces a reduction in the meridional component, following the continuity assumption.

On the other hand, the total pressure prediction confirms a tendency to underestimate losses (Fig. 2.18b). Although the separation between experimental and numerical curves is much more reduced compared to the previous discussions, the meanline solution is stably higher, with a maximum discrepancy in the central portion. While considering the static pressure field, the nearly constant spanwise distribution is consistently reproduced, although uniformly distant from the measurements, indicating overprediction. This trend aligns with the other data. Within ARES, as explained in the code presentation, only the total head is solved. Therefore, the static quantity results from the difference between h_0 and the absolute kinetic term. Given the similarity of the velocity field, the overprediction of the total head causes the right shift of c_p . Here, the local fluctuations of the several variables compensate for each other, resulting in the constant spanwise trend.

AxWJ-2

This pump represents a typical example of pump, specifically designed for waterjet applications [92, 28, 84]. The geometry is extensively presented in

2. DESIGN

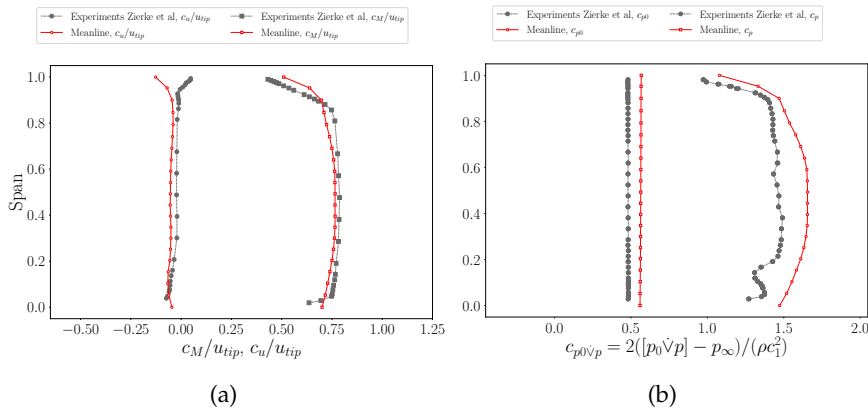


Figure 2.18: Spanwise distribution of the flow statistics, comparing ARES solution and experiments from Zierke et al. [134], downstream of the HIREP rotor, for design conditions ($\varphi = 1.36$). Reported quantities include: normalised tangential and axial velocities (a) and total and static pressure coefficients (b).

Section 3.3, where the discussion deeply focuses on the validation of the CFD models based on such test case. Differently from the previous test cases, this pump is composed by both a rotor and a stator. Furthermore, the duct geometry experiences significant variations from the inlet to the outlet station. Specifically, the tip to hub radius ratio transitions from 0.3 at the rotor entrance, to 0.25 at the machine outflow, with a maximum value of 0.5 at mid-stage. In this regard, the entire passage cannot be assumed as a straight duct.

The operating map is recovered through systematic variation of the inlet flow rate, while letting the rotor speed and inlet total pressure unchanged (Fig. 2.19). In this regard, the flow and work coefficients are defined as in the previous geometry study, while the efficiency is computed following the relation used for the NASA R02. Spanwise-uniform boundary conditions are considered for this test case, thus inducing constant radial distribution of the inflow meridional velocity and no pre-swirl component. The computed points extend well above the design conditions, and even at higher flow configurations than measured during experiments. The code proves stable even for entering flow rates 30% greater than the expected value. However, while the predicted head rise and efficiency portray a smooth decreasing behaviour, the performance drop is notably exaggerated. Specifically, considering the second parameter, the discrepancy starts from a value of $\sim 5\%$ near design conditions ($\varphi = 0.85$) and becomes almost doubled for the operating point at the farthest right. Conversely, towards the best efficiency point the meanline prediction approaches measurements. In fact, around $\varphi = 0.77$ the deviation in the efficiency curve is reduced to 1.4%. Similar considerations hold for the pressure rise characteristic, where the most accurate estimate reaches $\Delta\psi = 0.06$ at the first point on the map.

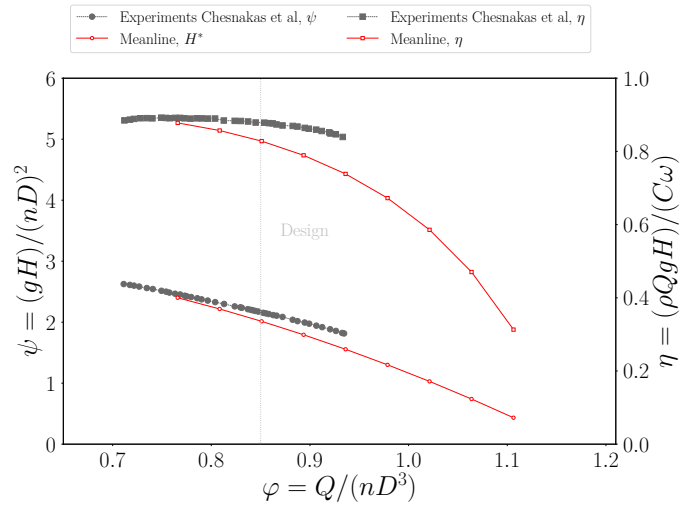


Figure 2.19: Overall head coefficient and efficiency as functions of the flow rate coefficient for the AxWJ-2 pump, comparing ARES solution and experimental values from Chesnakas et al. [28].

PIV measurements were performed by Chesnakas et al. [28] downstream of both the rotor and the stator. The velocities of the flow leaving the rotating blade are analysed first (Fig. 2.20). Across the mid-stage plane, the radial distribution of the axial component closely aligns with the measured curve, except for a considerable velocity defect from the hub to span $\sim 20\%$ (Fig. 2.20a). Thus, the plots are almost superimposed up to the tip location, where the meanline code denotes a weakness in predicting the near shroud dynamics affected by the boundary layer. Similarly, the estimate for c_u portrays the main discrepancies in the lower portion of the rotor blade, while for a substantial central region the prediction is considerably accurate (Fig. 2.20b). The scarce end-wall capturing ability induces a marked difference at the tip end for this velocity component as well.

Hence, the code reliability is evaluated downstream of the stator blade (Fig. 2.21). Here, the comparison with experiments is only approximate. In fact, ARES solves the outlet plane assuming it coincides with the trailing edge locus of points, whereas during the test campaign, measurements were taken at the nozzle exhaust. As aforementioned, the duct section undergoes several variations from the inlet to the outlet sections. In particular, the flow leaving the stator blade further expands in the terminal portion of the nozzle. The latter consisting in a convergent, axisymmetric shape, with no centerbody obstruction. As a consequence, part of the axial velocity defect in Figure 2.21a is ascribed to the different extension of the sectional area. Despite this consideration, the spanwise trend aligns with the experimental curve. The code proves to capture the fluctuation just above span 40%. Conversely, it exaggerates the velocity drop near the blade root.

2. DESIGN

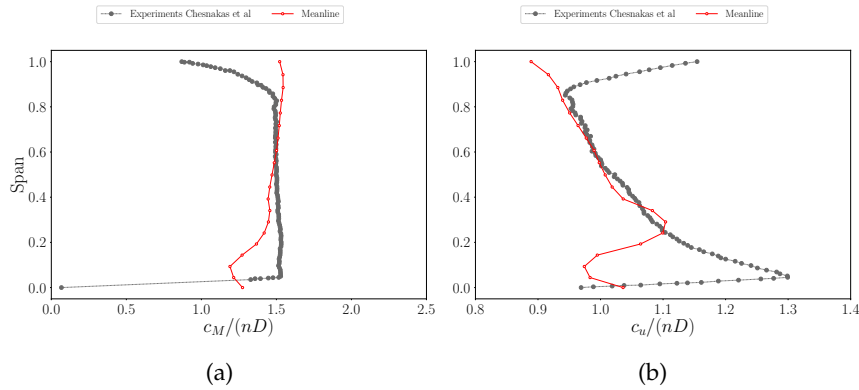


Figure 2.20: Spanwise distribution of the flow statistics, comparing ARES solution and experiments from Chesnakas et al. [28], downstream of the AxWJ-2 rotor, for design conditions ($\varphi = 0.85$). Reported quantities include: normalised meridional (a) and tangential (b) velocities.

Regarding the tangential component, it is expected to be only marginally affected by the further downstream nozzle contraction (Fig. 2.21b). Nevertheless, the meanline prediction indicates a difficulty in providing a rectified flow similar to the real machine. The trends of the two curves are substantially different, and the minimum discrepancy can only be detected near span 40%, due to a peak in the measured data. However, the maximum velocity values are recovered by ARES exactly where the measurements suggest that the tangential component is suppressed. Furthermore, the code fails to capture

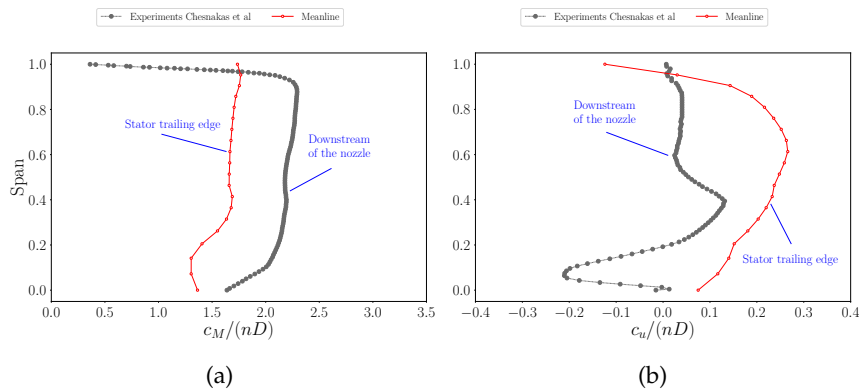


Figure 2.21: Spanwise distribution of the flow statistics, comparing ARES solution and experiments from Chesnakas et al. [28], downstream of the AxWJ-2 stator, for design conditions ($\varphi = 0.85$). Measurements refer to the nozzle exhaust, which further expands the flow from the station used for meanline predictions, at the blade trailing edge. Reported quantities include: normalised meridional (a) and tangential (b) velocities.

local fluctuations along the radial coordinate. Additional investigations are expected to reveal the possible influence of the duct shape on this behaviour, thus recovering possible ways to mitigate it.

In general, ARES proves an efficient and fast tool for axial-flow pumps performance prediction. Despite a tendency to underestimate the losses, at near design conditions the computation provides low error estimate of the overall statistics for a variety of geometry and operating configurations. Outside optimal operations, the code demonstrates stability, particularly for flow rates higher than the design, despite a pronounced overestimation of the performance drop. Conversely, at lower flow coefficients, the analysis becomes less robust, and potential divergence or flow reversals may occur.

At a local level, the spanwise distributions of the velocities are generally well-captured. However, the pressure field consistently exhibits considerable overprediction. There is a belief that there is room for improving the code accuracy. While at the current stage it proves usable across many different applications, further examination of the available empirical correlations and additional calibration are expected to benefit the accuracy at both local and overall level, making it possible to encompass a wider range of operating points.

3 VALIDATION

3.1 Numerical methods

This section addresses the numerical methodology employed for CFD analysis throughout the entire manuscript.

3.1.1 Governing equations

The technique used in homogeneous multiphase analysis involves the sharing of a unified flow field across all fluids, resulting in identical transported quantities for both the liquid and vapour phases. Instead of solving individual phasic transport equations, the model focuses only on bulk transport equations [3]. Consequently, for dynamical modelling of the liquid/vapour mixture, a pressure-based RANS solver in a steady-state framework is employed. This is designed based on the Reynolds decomposition ($\phi = \bar{\phi} + \phi'$), and the model can be represented by the following momentum equations:

$$\frac{\partial (\bar{\rho}_m \bar{u}_j)}{\partial x_j} = 0 \quad (3.1a)$$

$$\frac{\partial (\bar{\rho}_m \bar{u}_i \bar{u}_j)}{\partial x_j} = -\frac{\partial \bar{p} \delta_{ij}}{\partial x_j} + \frac{\partial \bar{\tau}_{ij}}{\partial x_j} + \frac{\partial T_{ij}}{\partial x_j} + S_i \quad (3.1b)$$

In the equations, \bar{u}_i represents the ensemble-averaged velocity component along the i -th direction, $\bar{\rho}_m$ is the ensemble-averaged mixture density, and \bar{p} denotes the ensemble-averaged mechanical pressure. Moreover, $\bar{\tau}_{ij}$ signifies the molecular stress tensor components, and $T_{ij} = -\bar{\rho}_m \overline{u'_i u'_j}$ denotes the Reynolds stress tensor components. The molecular stress components are described according to the Newtonian flow hypothesis by the equation:

$$\bar{\tau}_{ij} = \bar{\mu}_m \left(\frac{\partial \bar{u}_i}{\partial x_j} + \frac{\partial \bar{u}_j}{\partial x_i} - \frac{2}{3} \frac{\partial \bar{u}_s}{\partial x_s} \delta_{ij} \right) \quad (3.2)$$

Here, $\bar{\mu}_m$ represents the mixture molecular viscosity, and δ_{ij} indicates the Kronecker tensor. These parameters are defined by the volume fractions as follows:

$$\bar{\rho}_m = \alpha_l \bar{\rho}_l + \alpha_v \bar{\rho}_v \quad (3.3a)$$

$$\bar{\mu}_m = \alpha_l \bar{\mu}_l + \alpha_v \bar{\mu}_v \quad (3.3b)$$

Where α_l and α_v signify the liquid and vapour volume fractions, respectively. Finally, S_i denotes the source terms associated with the moving-reference portions of the domain. It should be noted that the fluid equations are cast in a general form for a two-phase medium. However, when a single-phase fluid is considered (i.e. pure liquid in the present study) the volume

3. VALIDATION

fractions reduce to $\alpha_l = 1$ and $\alpha_v = 0$ anywhere in the domain and the equations are solved with Equations 3.3 being constantly defined in the entire domain.

3.1.2 Modelling of turbulence

The Reynolds stress components are incorporated through the application of Boussinesq's hypothesis:

$$-\bar{\rho}_m \overline{u'iu'j} + \frac{2}{3}k\delta_{ij} = \mu_T \left(\frac{\partial \bar{u}_i}{\partial x_j} + \frac{\partial \bar{u}_j}{\partial x_i} - \frac{2}{3} \frac{\partial \bar{u}_s}{\partial x_s} \delta_{ij} \right) \quad (3.4)$$

Here, $k = 1/2\bar{\rho}_m \overline{u'_i u'_i}$ represents the turbulent kinetic energy, while μ_T denotes the turbulent viscosity. The selection of the latter involves several models of varying complexity to determine the numerical model sensitivity to turbulence closure. Precisely, the present analysis employs several 1-, 2- and 4-equation techniques. These models are briefly reviewed here, but for a more comprehensive understanding, readers are advised to refer to the specific literature or the Ansys CFX [3] and Fluent [4] theory guides. Throughout the analysis, the default settings for all the models remain unchanged.

1-equation models: Spalart-Allmaras and Eddy Viscosity Transport Equation

Both the Spalart-Allmaras (SA) [112] and the Eddy Viscosity Transport Equation (EVTE) [90] models features a single transport equation dedicated to the kinematic eddy viscosity, $\tilde{\nu}_t$, expressed as follows:

$$\begin{aligned} \frac{\partial \bar{\rho}_m \tilde{\nu}_t}{\partial t} + \frac{\partial \bar{\rho}_m \bar{u}_j \tilde{\nu}_t}{\partial x_j} &= G_{\tilde{\nu}_t} - Y_{\tilde{\nu}_t} + \\ &+ \frac{1}{\sigma_{\tilde{\nu}_t}} \left[\frac{\partial}{\partial x_j} \left\{ (\mu_m + \bar{\rho}_m \tilde{\nu}_t) \frac{\partial \tilde{\nu}_t}{\partial x_j} \right\} + C_{b2} \bar{\rho}_m \left(\frac{\partial \tilde{\nu}_t}{\partial x_j} \right)^2 \right] \end{aligned} \quad (3.5)$$

The two approaches mainly differing based on how they define the production, $G_{\tilde{\nu}_t}$, and destruction, $Y_{\tilde{\nu}_t}$, of turbulent kinematic viscosity, as well as related constants (e.g., C_{b2}). Here, μ_m denotes the mixture molecular viscosity, while for the kinematic eddy viscosity the following relation holds:

$$\mu_t = \bar{\rho}_m \tilde{\nu}_t \quad (3.6)$$

For in-depth information regarding the model constants and a detailed explanation of each term, one can refer to the corresponding theory guides [3, 4].

2-equation models: $k - \varepsilon$ and $k - \omega$ SST

The $k - \omega$ SST [91] model integrates a blending function to smoothly transition from the standard $k - \omega$ model [124] in the boundary layer to a higher Reynolds

number form of the $k - \varepsilon$ [73] model in the boundary layer outer region. Either ε and ω based closure techniques share a common transport equation for the turbulent kinetic energy, k , defined as:

$$\frac{\partial(\bar{\rho}_m k)}{\partial t} + \frac{\partial}{\partial x_j} (\bar{\rho}_m \bar{u}_j k) = \frac{\partial}{\partial x_j} \left[\left(\bar{\mu}_m + \frac{\mu_t}{\sigma_{k3}} \right) \frac{\partial k}{\partial x_j} \right] + P_k - D_k \quad (3.7)$$

With the turbulence production term, P_k , being identically formulate, the only differences lie in the definitions of the turbulent kinetic energy dissipation, D_k , as a function of ε and ω , accordingly, and the relations for the turbulent viscosity, respectively obtained from:

$$\mu_t = \rho_m C_\mu \frac{k^2}{\varepsilon} \quad (3.8)$$

$$\mu_t = \rho_m \tilde{\nu}_t \frac{k}{\omega} \quad (3.9)$$

The models then differentiate based on the second closure equation, being respectively cast as a transport evolution of the turbulent kinetic energy dissipation rate, $\varepsilon = \nu_m \overline{\partial u_i' / \partial x_j \partial u_i' / \partial x_j}$, and of the turbulent frequency, $\omega = \varepsilon / k$. The corresponding definitions hold as:

$$\frac{\partial(\bar{\rho}_m \varepsilon)}{\partial t} + \frac{\partial}{\partial x_j} (\rho_m \bar{u}_j \varepsilon) = \frac{\partial}{\partial x_j} \left[\left(\bar{\mu}_m + \frac{\mu_t}{\sigma_\varepsilon} \right) \frac{\partial \varepsilon}{\partial x_j} \right] + \frac{\varepsilon}{k} (C_{\varepsilon 1} P_k - C_{\varepsilon 2} \bar{\rho}_m \varepsilon) \quad (3.10)$$

$$\begin{aligned} & \frac{\partial(\bar{\rho}_m \omega)}{\partial t} + \frac{\partial}{\partial x_j} (\rho_m \bar{u}_j \omega) = \\ & \frac{\partial}{\partial x_j} \left[\left(\bar{\mu}_m + \frac{\mu_t}{\sigma_{\omega 3}} \right) \frac{\partial \omega}{\partial x_j} \right] + (1 - F_1) 2 \bar{\rho}_m \frac{1}{\sigma_{\omega 2} \omega} \frac{\partial k}{\partial x_j} \frac{\partial \omega}{\partial x_j} + \alpha_3 \frac{\omega}{k} P_k - \beta_3 \bar{\rho}_m \omega^2 \end{aligned} \quad (3.11)$$

Modifications to the ε transport equation and the C_μ definition proposed by Shih et al. [108] contributed to the formulation of the so-called *Realizable $k - \varepsilon$* model, which has shown distinct improvements over the other $k - \varepsilon$ variants. For this reason, this modified arrangement is adopted in the present study and the reader is referred to the Fluent theory guide [4] for detailed explanations of the altered definitions. Specifically designed to consider turbulent shear stress transport, the SST model improves the accuracy of the previous formulations in predicting flow separations under adverse pressure gradients. This is done by modifying the definition of the $k - \omega$ turbulence viscosity in such a way that the strain rate magnitude, S , is taken into account:

$$\mu_t = \rho_m \tilde{\nu}_t \frac{k}{\omega} \frac{1}{\max \left[\frac{1}{\alpha^*}, \frac{S F_2}{\alpha_1 \omega} \right]} \quad (3.12)$$

Detailed interpretations of the terms are extensively available in the theory guide [3, 4].

3. VALIDATION

4-equation model

The four-equation Transition SST (TSST) model [72], also recognized as the $\gamma - \tilde{R}e_{\theta t}$ model, endeavours to enhance the two-equation $k - \omega$ SST model by introducing two additional transport equations, addressing intermittency (γ) and transition onset criteria ($\tilde{R}e_{\theta t}$) regarding transported momentum-thickness Reynolds number. These parameters are aimed at capturing the transition from laminar to turbulent flow, whereas the $k - \omega$ SST model assumes full turbulence. The associated equations are as follows:

$$\frac{\partial(\bar{\rho}_m \gamma)}{\partial t} + \frac{\partial(\bar{\rho}_m \bar{u}_j \gamma)}{\partial x_j} = P_{\gamma 1} - E_{\gamma 1} + P_{\gamma 2} - E_{\gamma 2} + \frac{\partial}{\partial x_j} \left[\left(\bar{\mu}_m + \frac{\mu_t}{\sigma_\gamma} \right) \frac{\partial \gamma}{\partial x_j} \right] \quad (3.13a)$$

$$\frac{\partial(\bar{\rho}_m \tilde{R}e_{\theta t})}{\partial t} + \frac{\partial(\bar{\rho}_m \bar{u}_j \tilde{R}e_{\theta t})}{\partial x_j} = P_{\theta t} + \frac{\partial}{\partial x_j} \left[\sigma_{\theta t} \left((\bar{\mu}_m + \mu_t) \frac{\partial \tilde{R}e_{\theta t}}{\partial x_j} \right) \right] \quad (3.13b)$$

In these equations, $P_{\gamma 1}$ and $E_{\gamma 1}$ represent relaminarization sources, while $P_{\gamma 2}$ and $E_{\gamma 2}$ denote the relaminarization sources. $P_{\theta t}$ is the source term in the transport equation of $\tilde{R}e_{\theta t}$. These equations interact with the $k - \omega$ SST model through alterations in the transport equation for k .

3.1.3 Modelling of cavitation

The Zwart-Gerber-Belamri (ZGB) cavitation model [135], identified as the sole incorporated cavitation model in CFX, is utilized to address the cavitation effects. Based on the Rayleigh-Plesset equation, this model describes the expansion of a spherical vapor bubble within a liquid. Consequently, an auxiliary transport equation is employed to represent the cavitation effect, which reads as:

$$\frac{\partial(\alpha_v \rho_v)}{\partial t} + \frac{\partial(\alpha_v \rho_v u_j)}{\partial x_j} = \dot{m}_{vap} - \dot{m}_{cond} \quad (3.14)$$

were, \dot{m}_{vap} and \dot{m}_{cond} represent the vaporization and condensation terms, defined as follows:

$$\dot{m}_{vap} = F_{vap} \frac{3\rho_v (1 - \alpha_v) \alpha_{nuc}}{R_{nuc}} \sqrt{\frac{2}{3} \frac{p_v - p}{\rho_l}} \quad (p \leq p_v) \quad (3.15)$$

$$\dot{m}_{cond} = F_{cond} \frac{3\rho_v \alpha_v}{R_{nuc}} \sqrt{\frac{2}{3} \frac{p - p_v}{\rho_l}} \quad (p \geq p_v) \quad (3.16)$$

Here, p is the local pressure, p_v is the saturation pressure, F_{cond} is the condensation coefficient, F_{vap} is the vaporization coefficient, R_{nuc} is the nucleation site radius, and α_{nuc} is the nucleation site volume fraction. According to the CFX theory guide [3], the ZGB model coefficients are set to $F_{cond} = 0.01$, $F_{vap} = 50$, $R_{nuc} = 1 \times 10^{-6}$ m and $\alpha_{nuc} = 5 \times 10^{-4}$.

3.1.4 Thrust-Drag Bookkeeping

Following the aeronautically-inspired nature of the present model, the metrics for propulsive performance evaluation are borrowed from the aero-engine Thrust-Drag Bookkeeping (TDB). Modified near-field approaches have already proven their reliability and robustness for application to turbofan nacelles optimisation [82]. For this reason, the same numerical approach is adopted in the next Chapter discussion. To maintain consistency, the methodology is here briefly outlined to be employed for installed pump configuration propulsive performance. The focus of the work is the behaviour of pump installation inside an axisymmetric intake. The remainder of a notional submerged propulsor, that consists on the nozzle outlet geometry, is not included at the current stage. Additionally, the domain is truncated at the nozzle out-plane, thus assuming adaption to ambient conditions. As a consequence, the post-exit stream tube is cut out from the domain and the corresponding influence on the propulsive characteristic is neglected. The system configuration can be conceptualised as in Figure 3.1 .

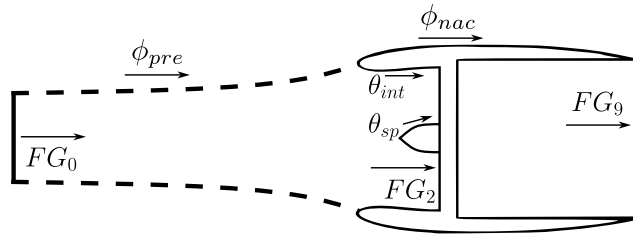


Figure 3.1: Domain decomposition for the thrust-drag bookkeeping of the present model. Image adapted from Robinson et al. [104].

According to the bookkeeping theory, the control volume is subdivided into two regions where both Gauge (FG) and wall forces contribute to determining the net thrust acting on the propulsor. Based on the zone were they are computed, wall forces are defined as θ or ϕ components, respectively for thrust and drag domain quantities. The latter being identified as the volume fractions correspondingly inside and outside the processed stream tube that can be defined as the revolution of the stagnation and ejected stream line. Forces components are obtained using the following [82]:

$$\phi, \theta = \hat{x} \int \int [(p - p_\infty)\hat{n} + \bar{\tau}_w \cdot \hat{n}] dA \quad (3.17)$$

$$FG = \hat{x} \int \int [(p - p_\infty)\hat{n} + \rho V(\vec{V} \cdot \hat{n})] dA \quad (3.18)$$

where \hat{x} is the advancing direction along which forces are computed, p_∞ is the undisturbed static pressure, \hat{n} is the walls surface normal, $\bar{\tau}_w$ is the tensor of the wall viscous stresses. From Figure 3.1 it follows that for the nacelle drag

3. VALIDATION

computation the next relation holds:

$$D_{nac} = \phi_{pre} + \phi_{nac} + \cancel{\phi_{post}} \quad (3.19)$$

Here, the pre-entry stream tube drag component results from the momentum balance as:

$$\phi_{pre} = FG_2 - FG_0 + \theta_{int} + \theta_{sp} \quad (3.20)$$

Then, it is possible to normalise the drag force through the maximum cross-sectional area of the propulsor, A_{max} , to recover the drag coefficient as:

$$c_{D_{nac}} = \frac{2D_{nac}}{\rho v_{\infty}^2 A_{max}} \quad (3.21)$$

In addition, when momentum imbalance is integrated over the whole control volume, the net thrust results as:

$$T = FG_0 - FG_9 + D_{nac} \quad (3.22)$$

For further details on the derivation of the previous equations the reader is referred to the copious literature production [29, 113, 104, 81, 102, 82].

3.2 Propulsor 2D-axisymmetric model

3.2.1 Computational model

Inlet geometry

The geometry selected for the intake numerical models validation is that reported by Sobolewski [111] (Fig. 3.2). This choice is motivated by its geometrical, operational and fluid dynamic affinity with the propulsor developed by SEALENCE S.p.a. The adopted model represents a suitable reference for high-performance waterjet ram-type inlets. Its design being the result of a compromise between minimum drag and cavitation-free operations at both cruise and hump velocities of 100 *kts* and 35 *kts* respectively. To this end, a variable area device was devised, by employing an axially movable centerbody (or *plug*) to match the wanted IVR for fully-retracted (take-off) and fully-extended (cruise) configurations. Trial and error approach allowed for the selection of the optimal solution satisfying the requirements, which is characterised by a capture-area-based $IVR = 0.85$ and 0.89 , respectively for in- and off-design conditions [71]. The flow is then delivered to the pump, housed inside the ship, through the hollow pod welded to the hull. The present work retains and investigates only the intake portion, thus cutting the part from which the flow is redirected towards the vertical ducting.

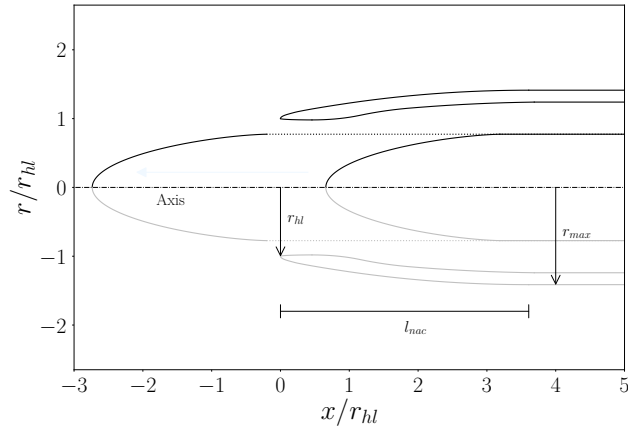


Figure 3.2: Outline of the reference intake geometry with plug in both fully-retracted and fully-extended configuration. Hub trace for cruise condition is depicted with dotted lines. The dimensions are normalised using the highlight radius, r_{hl} .

Domain discretisation

The two-dimensional computational domain is discretised using Pointwise®, by adopting a multi-block strategy through structured type elements (Fig. 3.3). The far-field boundary is shaped through a circular arc, extending up to ~ 20 times the highlight radius, r_{hl} , from the propulsor walls near-field. To further distance the outflow boundary conditions from the effective intake geometry, horizontal extensions are created from the right ends of the walls to about $10 r_{hl}$. The beginning cells are generated using a normal extrusion from the solid surfaces, by choosing an initial off-wall spacing of $\sim 2 \cdot 10^{-5} r_{hl}$, which is suitable for a y^+ estimate lower than 1 for any considered flow condition. Cell sizing is gradually expanded towards the external boundaries following a geometrical progression with a growth rate approximately equal to 1.05. Nodes counts in the wall-tangential direction are adjusted to favour denser distributions at the rounded regions, especially at the highlight and the plug extremities. Following this strategy for both fully-retracted (Fig. 3.3a) and fully-extended (Fig. 3.3b) configuration, the grid quality was ensured to maintain in any case either maximum and average equiangular skewness below 0.61 and 0.12, respectively.

Numerical schemes and boundary conditions

The solution of the 2D-axisymmetric steady-state RANS equations is approached using the cell-based Finite Volume solver from Ansys, Fluent [5]. The momentum, pressure, and turbulence terms are initially discretised using first-order upwind schemes until convergence is achieved. Subsequently, the accuracy is switched to second-order schemes for pressure and third-order

3. VALIDATION



Figure 3.3: Closeup view of the computational grid around the intake wall for both fully-retracted (a) and fully-extended (b) configuration.

Monotone Upstream-Centered Schemes for Conservation Laws (MUSCL) for the remaining terms.

To exploit the ability of the solver to obtain axisymmetric solutions from a planar computational domain, the axis boundary condition must be applied along a linear connector aligned with the x -axis. The flow configuration is instead imposed by combining different types of boundary conditions. The mass flow rate is enforced on the vertical connector, where the actual geometry is truncated, before the flow is redirected to the pod ducting and then to the pump. For the far-field circular-arc, velocity inlet boundary condition is chosen, while static pressure is imposed through a pressure outlet condition on the vertical line that completes the domain by linking the free-stream with the propulsor surfaces extensions. The latter, together with all the other geometry curves, are treated as no-slip walls.

Computations are initialised using an hybrid technique and solved until convergence before changing the discretisation order and proceeding until completion. In this regard, the convergence criteria are set on the equations residuals to be lower than $1 \cdot 10^{-5}$ and on the per-iteration x -component walls' force residual to be lower than $1 \cdot 10^{-6}$.

3.2.2 Results

To conduct an extensive sensitivity study of the model, the analysis includes either mesh dependency and turbulence treatment variability. The first aspect is addressed through generation of three mesh refinements, namely: coarse, medium and refined. These count, respectively for retracted and extended configurations, $253k$ and $376k$ cells on the first level, $571k$ and $755k$ on the second, and $1.37M$ and $1.5M$ on the latter. The chosen values are consistent with the intention to maintain at least a factor 2 throughout the refinement process. As far as the turbulence modelling, four formulations with increasing complexity of the boundary layer treatment are considered, namely: the

1-equation Spalart-Allmaras, the 2-equation standard $k - \varepsilon$, the 2-equation SST and the 4-equation Transition SST. Computations are performed to reproduce experimental measurements from Sobolewski [111], which included investigating both in- and off-design conditions.

Typical solutions of the two configurations are taken from the medium grid simulations and reported in Figures 3.4 and 3.5 respectively, through pressure coefficient contours superimposed with streamlines, coloured with the normalised stream function, ψ . The latter, derived from $\rho u_j = \pm \partial \psi / \partial x_i$ [5], is made non-dimensional using the mass flow rate processed by the pump, \dot{m}_{pump} . In particular, the analysis focuses on three operational configurations: a take-off-typical situation where (cruise-capture-area-based) $IVR = 3.34$ and highlight diameter-based Reynolds number, $Re_{hl} = \rho v_\infty D_{hl} / \mu = 3 \cdot 10^5$, and two more at high-speed cruise regimes, characterised by $IVR = 0.71$, advancing on a flow with $Re_{hl} = 1.2 \cdot 10^6$. What differentiates the latter is the simulated submergence, which regulates the free stream static pressure and is here expressed through the cavitation number as follows:

$$\sigma = \frac{2(p_\infty - p_v)}{\rho v_\infty^2} \quad (3.23)$$

For the three computations, this value is taken respectively equal to: 11.39 (Fig. 3.5), 0.128, and 0.082 (Fig. 3.4), which correspond to the opposite of the pressure coefficient evaluated at the saturation pressure.

At near-design conditions the inner plug is completely extracted, which reduces the passage section at the highlight if compared to initial hump phases. The capture stream-tube is such shaped that the stagnation line is almost located at the highlight point, thus generating an optimal distribution of the entering mass flow rate and a reduction of the entrance losses. The flow smoothly accelerates through the intake throat and is then gradually diffused before being redirected to the pump. In this regard, the pressure field depicts almost the same solution for any considered turbulence model, except for minor local differences detectable in the 4-equation closure case (Fig. 3.4d), which appear induced by the corresponding velocity field distribution. In fact, when considering this variable, the four turbulence models recover different behaviours, mainly related to the prediction of the boundary layer in the diffusing region. In particular, both the SA (Fig. 3.4a) and the SST (Fig. 3.4c) agree in recognising the presence of a single circulation bubble at the hub, following the flow deceleration. However, for the former tends to place the re-attachment location further downstream and to overestimate the bubble thickness if compared with the latter. Conversely, the flow evolution obtained with Transition SST depicts the presence of a non-uniform boundary layer development, where the circulation narrows before enlarging again. Anyhow, the overall extension of the bubble is significantly reduced than the previous solutions. Regarding this aspect, the $k - \varepsilon$ (Fig. 3.4b) performs much differently, being insensitive to the boundary layer growth occurring at the hub.

3. VALIDATION

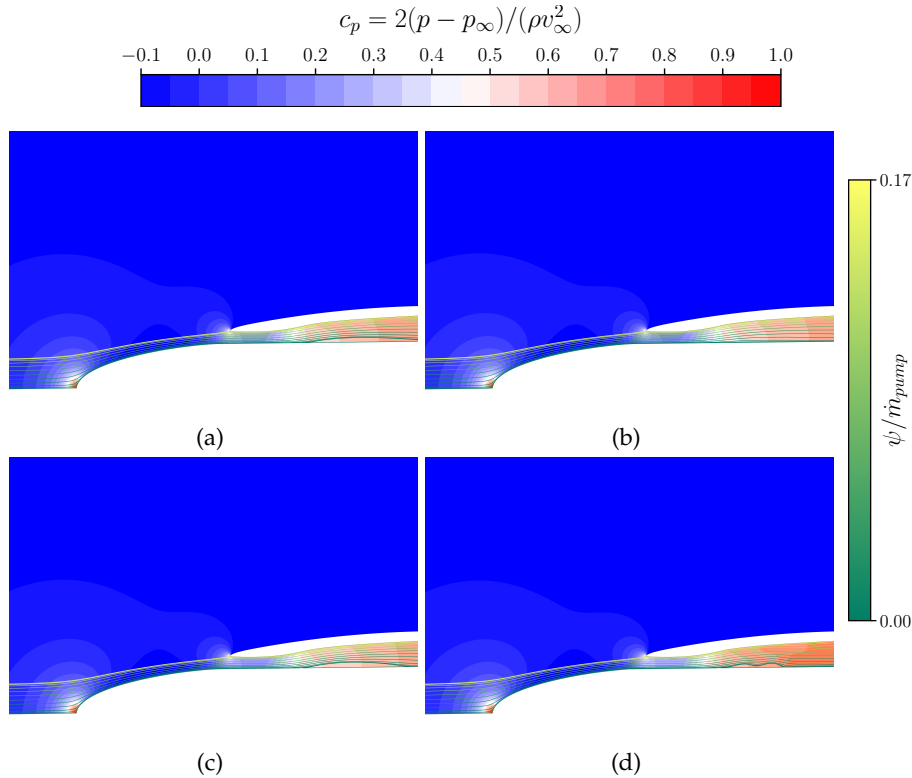


Figure 3.4: Contours of pressure coefficient, c_p , superimposed with streamlines coloured by stream function, ψ , normalised with the pump mass flow rate. Results are taken from medium grid domain at $IVR = 0.71$, highlight-based $Re_{hl} = 1.2 \cdot 10^6$ and inflow cavitation number $\sigma = 0.128$, for the four turbulence models, respectively: Spalart-Allmaras (a), $k - \varepsilon$ (b), SST (c) and Transition SST (d).

On the other hand, at take-off operations the captured streamlines assume a convergent trend, typical of low advancing speed conditions, where the mass flow rate processed induces a highlight velocity substantially higher than the undisturbed one. As a consequence, during the acceleration phase the intake acts as an expansion device until the propulsor reaches a condition such that the free stream speed and the mass flow rate generate a divergent outline of the external stagnation streamline. It should be noted that the retraction of the inner plug is fundamental during take-off. In fact, this action leads to an actual (area-based) $IVR = 1.33$, over 2.5 times lower than the same quantity evaluated with the cruise-section area, which would probably correspond to prohibitive operating conditions for the system, due to the high flow turn at the lip, responsible for either separation or cavitation cloud obstruction. For this flow condition turbulence modelling variation shows no significant difference. A single uniform circulation region originates at the lip and extends

approximately up to the throat location. Although the SA (Fig. 3.5a) and the $\gamma - \tilde{R}e_{\theta_t}$ (Fig. 3.5d) tend to recover a larger extension, the boundary layer thickness is the same as the one reported by the other 2-equation models (Figs. 3.5b and 3.5c). In any case, the depression occurring within this region results in pressures that never exceed the saturation limit.

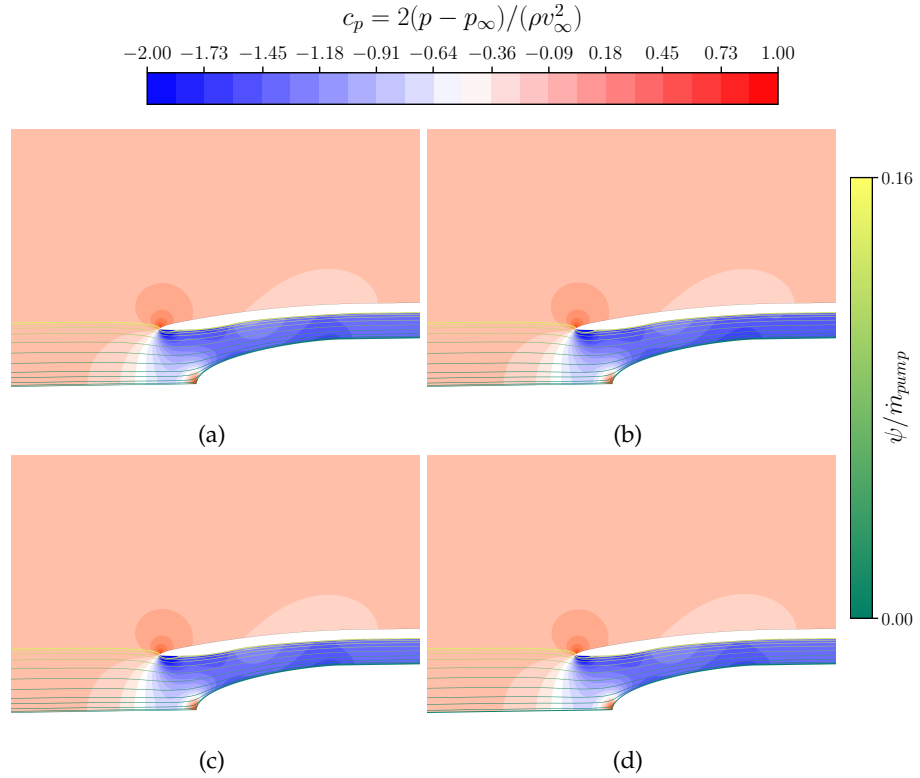


Figure 3.5: Contours of pressure coefficient, c_p , superimposed with streamlines coloured by stream function, ψ , normalised with the pump mass flow rate. Results are taken from medium grid domain at $IVR = 3.34$, highlight-based $Re_{hl} = 3 \cdot 10^5$ and inflow cavitation number $\sigma = 11.39$, for the four turbulence models, respectively: Spalart-Allmaras (a), $k - \varepsilon$ (b), SST (c) and Transition SST (d).

As additional metrics for the model sensitivity, a set of local quantities distributions (Fig. 3.6) is considered, namely: the non-dimensional wall distance, y^+ , and the skin friction coefficient, c_f . These statistics are compared by including both the discretisation and turbulence modelling variability. In particular, axial values are extracted from the spike wall, at both retracted (Figs. 3.6a and 3.6d) and extended (Figs. 3.6b and 3.6e) configuration, and at the nacelle external cowl (Figs. 3.6c and 3.6f). The corresponding flow conditions are: $\sigma = 11.39$, $\sigma = 0.128$ and $\sigma = 0.082$. In any setup, the plots depict a clear mesh independency within the same turbulence model. A similar

3. VALIDATION

consideration applies even to turbulence treatment when 1-equation SA and 2-equation SST models are considered. In fact, they both recover almost the same distribution of y^+ and c_f , for any geometrical and flow configuration, thus denoting an equivalent performance in what regards boundary layer reconstruction. In general, the shear layer predicted by the $k - \varepsilon$ is greater than the other models, despite showing a trend relatable to the two previously mentioned. In this regard, the 4-equation model recovers a substantial different behaviour. Either for retracted (Figs. 3.6a and 3.6d) and extended (Figs. 3.6b and 3.6e) configuration, the friction velocity on the fore portion of the spike abruptly decays before stabilising, which contrasts with the smooth outline depicted by the other solutions. At the terminal section of the retracted

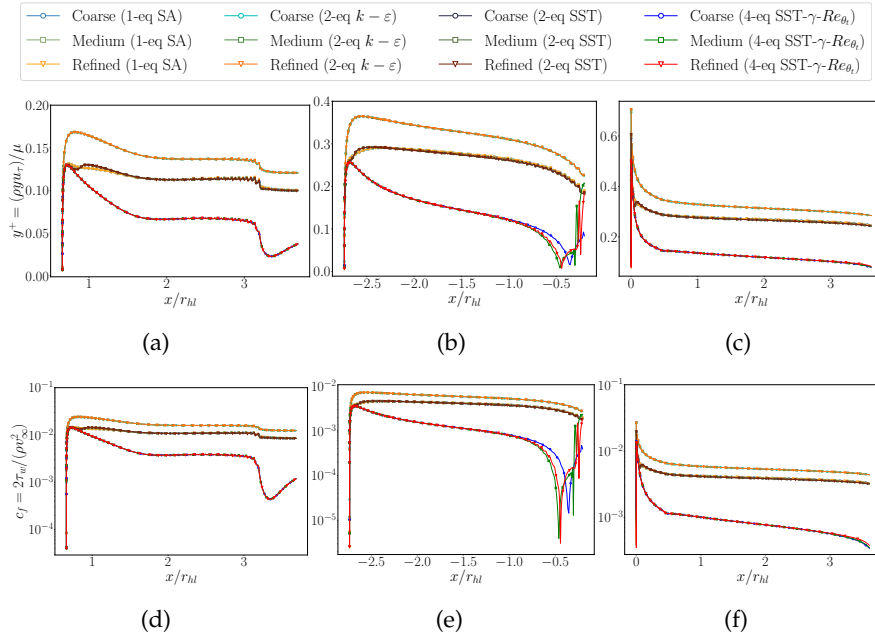


Figure 3.6: Axial distributions of non-dimensional wall-distance, y^+ (**a-c**), and skin friction coefficient, c_f (**d-f**), parametric on the grid refinements and turbulence models for the three free stream conditions considered, respectively: $\sigma = 11.39$ (**a-d**), $\sigma = 0.128$ (**b-e**) and $\sigma = 0.082$ (**c-f**).

plug, all models distinctly exhibit a sudden decrease in shear stress, with the Transition SST results being particularly accentuated. Moreover, the Transition SST results demonstrate a gradual increase preceding the connection to the hub, a distinctive observation not found in the other presented plots. As for the extended layout, the 4-equation model shows a significant influence of the entry flow dynamics at the highlight section, with the presence of markedly non-linear oscillations completely absent in the other curves. Despite minor differences generated by the three grid resolutions, the refinement does not seem to sufficiently mitigate the fluctuations. When considering the wall flow

on the external cowl, similar considerations can be drawn. However, while the magnitudes of the values are consistent with the previous discussion, the curves exhibit more comparable shapes in their trends.

Comparison with the experiments [111] is analysed through pressure coefficient values. In Figure 3.7 the design theoretical predictions are reported, where available, as a further detail. It should be mentioned that c_p differs in the internal data acquisitions of the spike (Fig. 3.7a) compared to the spike external and nacelle measurements (Figs. 3.7b and 3.7c). Specifically, the highlight average velocity is utilised for normalisation in the first case, whereas the free-stream velocity is adopted in the other cases. The numerical pressure fields demonstrate clear insensitivity to both grid resolution and turbulence modelling, with all curves collapsing into a single one at any case configuration. At take-off regimes (Fig. 3.7a) the present model performs more accurately than design prediction, which instead proved to overestimate pressure distribution. Despite the limited number of points available for comparison, the computations evidently show to fall in between the measurements obtained at $IVR = 3.20$ and $IVR = 3.40$, with the agreement being better near to the fore location. At the downstream end the CFD denotes to recover the solution from theoretical model. A minor discrepancy can be detected for the $k - \varepsilon$ model. The latter curve showing to depart from the others approximately from the axial coordinate 2 and even more downstream. Even at extended configuration (Fig. 3.7b) simulations provide a good approximation of the physical case. Again, numerics produces more accurate predictions closer to the plug leading tip, while gradually departing from test data towards the rear portion. As regards the external cowl (Fig. 3.7c), the present model confirms its reliability in reproducing the experimental evolution. However,

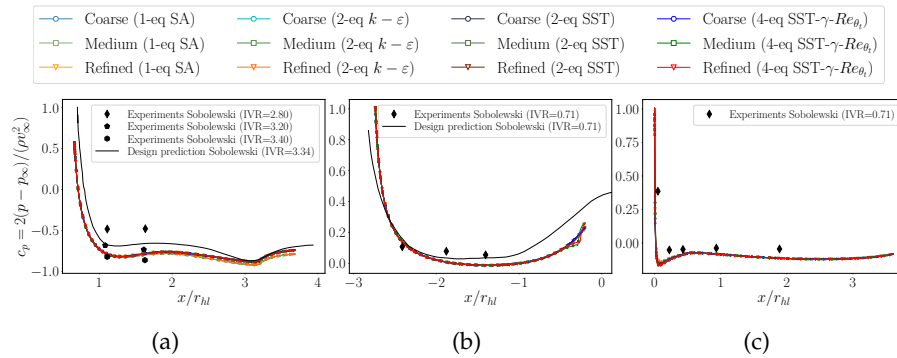


Figure 3.7: Comparison of pressure coefficient (c_p) axial distributions between present model and experiments from Sobolewski [111], parametric on the grid refinements and turbulence models for three free stream conditions, respectively: $\sigma = 11.39$ (a–d), $\sigma = 0.128$ (b–e) and $\sigma = 0.082$ (c–f).

although the general trend depicts significant adherence with test markers,

3. VALIDATION

the accuracy of the predicted undershoot near the lip cannot be tracked due to the lack of measurements at that location. As a consequence, there is no clue whether the discrepancy with the second station value is due to an over estimation of the negative peak or rather to the delay of the numerical model in recovering pressure. Anyhow, no improvements can be obtained from finer spatial resolution or more complex closures of RANS equations.

The previous discussion has overall confirmed the grid independency of the model, concerning the generated discretised domains. For this reason, to favour computing times for the optimisation loops discussed in Section 4.2, which involve a large number of CFD evaluations, an additional grid was defined to investigate the accuracy of a coarser mesh counting $119k$ cells to keep the refinement factor unchanged. Such an extra-coarse grid is created exclusively for the take-off retracted configuration, and the comparison is drawn in Figure 3.8 by plotting together the experimental data as well as the numerical results from the coarse level. The results in general prove that the further mesh coarsening produces no significant loss of accuracy, with the curves being still almost entirely superimposed with the corresponding obtained with greater spatial resolution.

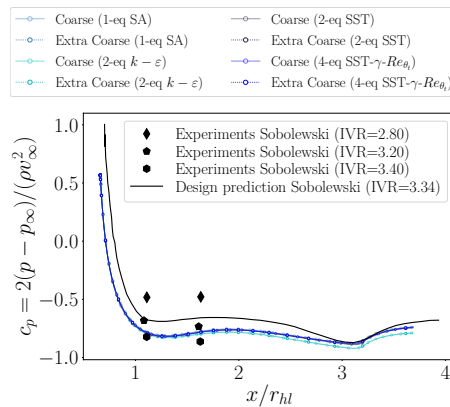


Figure 3.8: Pressure coefficient axial distributions from present model and experiments by Sobolewski [111], parametric on the turbulence models for free stream condition $\sigma = 11.39$. Comparison between coarse and extra coarse grids.

3.3 Pump 3D model

3.3.1 Computational model

Pump geometry

The ONR Axial flow Water Jet (AxWJ-2) stands as a marine propulsion system tailored to meet the specific requirements of a hypothetical high-speed

military vessel known as the Joint High-Speed Sealift (JHSS) [92]. At the core of this waterjet system lies the axial-flow pump, the geometry and data of which are publicly accessible, contributing to the development of fresh designs and supporting research endeavours, including the exploration of cavitation phenomena. For model testing, prototypes of the pump have been scaled and examined within three distinct facilities: the Naval Surface Warfare Center, Carderock Division (NSWCCD) 36-inch water tunnel, the Rolls Royce Hydrodynamics Research Centre (HRC) pump loop, and the John Hopkins University (JHU) water tunnel. Notably, the geometric configurations and results obtained from the NSWCCD tests, as detailed by Chesnakas et al. [28], serve as the point of reference for the current CFD study.

The NSWCCD water tunnel boasts a recirculation system that enables it to function as a pump loop. It can be adjusted to generate varying pressures within the tunnel, allowing for the exploration of the pump performance under cavitating conditions. The flow rate is controlled through a tunnel impeller. The AxWJ-2 test model, illustrated in Figure 3.9, comprises a six-blade rotor encased within a cylindrical housing, featuring a diameter of $D = 304.8$ mm and a tip clearance of 0.5 mm. Downstream, the flow is expanded through a nozzle equipped with an eight-blade rectifier stator. This stator component is flanged at both the ogival hub and the shroud, ensuring a seamless transition from the rotor dimensions to the throat diameter ($D_6 = 213.4$ mm) through the use of a revolved spline outline.

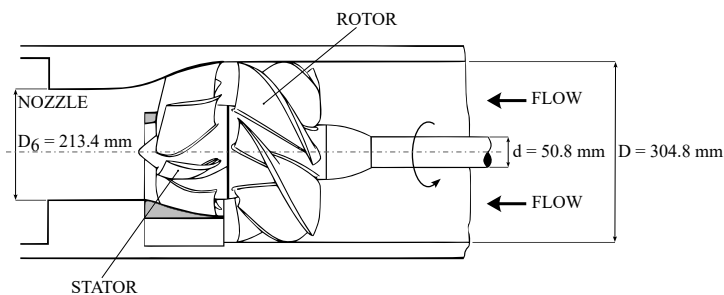


Figure 3.9: Geometry of the AxWJ-2 pump, adapted from Tan et al. [119].

Domain discretisation

The computational domain is constructed using a multi-block strategy (Fig. 3.10). Structured grids are exclusively employed to capture a singular passage around the blade regions using ANSYS TurboGrid® (Fig. 3.10a). This domain includes the cylindrical inlet within the rotor domain, extending the inflow boundary $2D$ upstream. The stator mesh is created near the blade, excluding the cone nose, and is adapted to promote cells quality. The discretisation methodology is based on a target node count to regulate the required domain size for the sensitivity study. The initial cell spacing near the wall regions, end

3. VALIDATION

walls, and blade surfaces is selected to conform to the inlet relative Reynolds number, aiming for an estimated y^+ value ranging from 1.3 to 1.1 across the three refinement levels. The maximum element length expansion rate is constrained to a maximum value of 2.1. Node distribution adjustments are made to ensure precise discretisation of the rounded leading and trailing edges without compromising the quality of surrounding cells (Fig. 3.10b). For the rotor blade, a modelled tip clearance of 0.02 inches is considered. Here, the grid expansion rate aligns with the cell sizes on both the shroud and blade tip surfaces.

A third block is generated using Pointwise® to further extend the domain $4D$ downstream and encompass the sharp end of the hub. This grid is divided into two regions. The primary region is structured and radially expands from the shroud boundary toward the axis of revolution. The domain is filled using a hybrid meshing technique, encompassing a mix of hexes, tets, prisms, and pyramids with typically extruded cells over the hub nose wall (Fig. 3.10c). Expansion rates and initial cell spacing are tailored to align with those of the communicating outflow boundary of the upstream stator block.

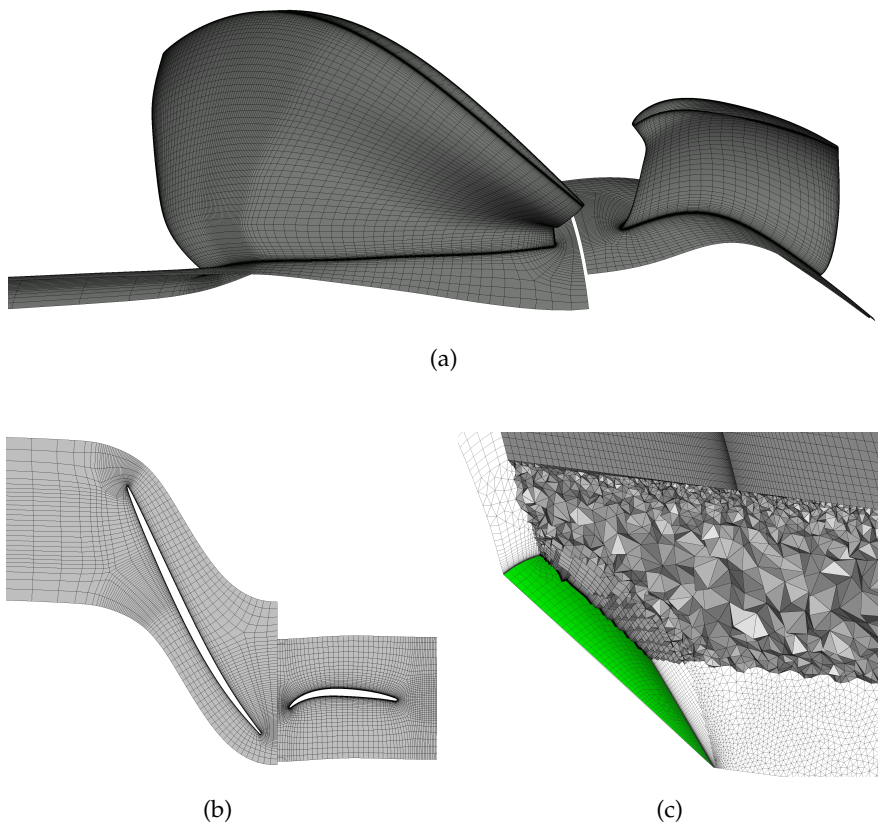


Figure 3.10: Details of the computational grid. (a) Blades' surface discretisation. (b) Zoom into the tip layer. (c) Magnification of the hybrid mesh in the proximity of the nose wall (green surface).

Numerical schemes and boundary conditions

Steady-state simulations are executed utilising Ansys CFX, exploiting a node-based Finite Volumes (FV) approach. The discretisation of advection and turbulence terms is performed using a high-resolution scheme, smoothing between first and second-order accuracy contingent on the local field gradient values.

Regarding boundary conditions, the axial symmetry of the configuration allows for computational cost reduction of the solution. This involves enforcing rotational periodicity along the boundaries defining the blade channels, resolving the circumferential flow evolution in the absent part of the domain. Total pressure is imposed as the rotor inlet boundary condition, while the mass flow rate is enforced on the domain outlet. Solid regions are managed as no-slip walls. In a steady configuration, the interpolation of the field solution between the rotating frame and the stationary one adopts a mixing plane strategy. For matching sides between the stator and the exhaust resulting from the multi-block strategy, a none-type interface can be chosen, as there is no pitch change or frame change occurring.

For nominal operation or thrust breakdown analyses, the initial state for the computations is set as single-phase solutions. Regardless of whether the fluid is considered a pure liquid or a mixture, the convergence strategy remains unaltered. Initially, solution stability is enhanced by conducting a maximum of 200 iterations with a local timescale approach at a factor of 5. The solution then switches to an auto timescale technique, maintaining the default step computed by the solver. Iterations are halted at a maximum of 500. Hydraulic efficiency is monitored as an additional stopping criterion. The Standard Deviation (SD) of that statistic is evaluated over a moving interval of 40 iterations. Computation interruption is determined by a value lower than 1×10^{-3} . Equation mass imbalances are consistently below 1%.

The loop computations were performed on a four-node cluster, each equipped with 10 Intel® Xeon® Silver 4114 CPUs running at 2.20GHz. These computations achieved convergence within 5 hours for the most demanding configuration, which included fine grid conditions under full cavitation. On average, the cavitation model sensitivity analysis required roughly 2 hours for each simulated point.

3.3.2 Results

Nominal operations

A representative solution obtained using the current model is illustrated in Figure 3.11. The visualisation details the flow field distribution through single-channel streamlines juxtaposed with static pressure contours along the pump wall surfaces. It is evident that the pressurised flow exiting the rotor blades

3. VALIDATION

is realigned by the stator to ensure an axial direction, enabling an optimal utilisation of the expansion for generating an axial thrust component.

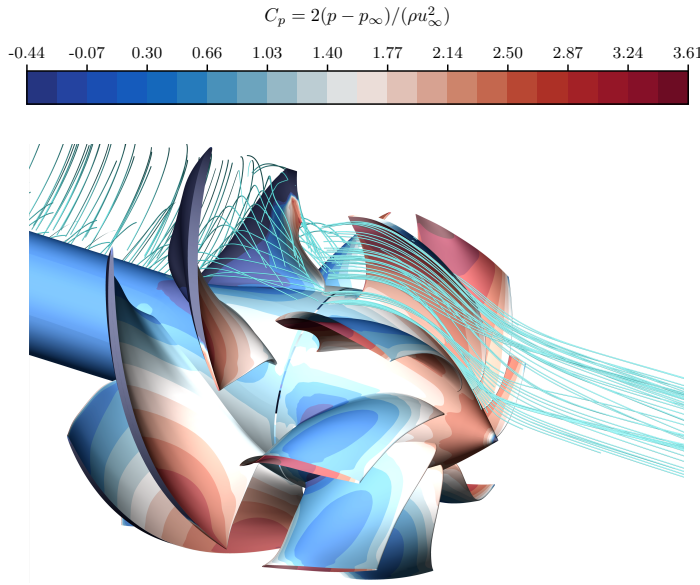


Figure 3.11: Contours of inlet axial velocity–based pressure coefficient on the pump walls, superimposed with a single-channel streamlines distribution.

In choosing the most appropriate numerical configuration, well-established CFD standards are adopted following [33, 34, 35, 23]. The evaluation of the system flow dynamics first focuses on a comparative analysis of the pump statistics under non-cavitating conditions and the measurements conducted by Marquardt [84]. Simulations are performed at a constant rotational speed of 1400 rpm, with variations in the mass flow rate controlled through the non-dimensional flow coefficient Q^* , where Q_f represents the volumetric flow rate and n is the rotational speed in rpm. The flow coefficient spans from 80% to 112% of the design condition, with uniform increments of $\Delta Q^* = 0.034$. The inlet total pressure is determined to prevent cavitation initiation based on the findings of Chesnakas et al. [28].

The assessment of the pump performance relies on three key parameters: the head coefficient (H^*), the power coefficient (P^*), and the hydraulic efficiency (η). These metrics are mathematically formulated as follows:

$$H^* = \frac{p_{t6} - p_{t3}}{\rho(nD)^2} \quad (3.24)$$

$$P^* = \frac{2\pi nT}{\rho n^3 D^5} \quad (3.25)$$

$$\eta = \frac{Q^* H^*}{P^*} \quad (3.26)$$

In these equations, p_{t3} and p_{t6} denote the total pressures at the inlet and outlet stations, respectively, and are calculated at specific measurement locations as

indicated by Marquardt [84]. The rotor torque is represented by the variable T .

The analysis incorporates three levels of mesh refinement, categorised as coarse, medium, and refined. These grids consist of $n_3 = 1.37$, $n_2 = 2.88$, and $n_1 = 6.02$ million cells, respectively. Each mesh is evaluated using three progressively complex turbulence models. The grid refinement ratio remains almost constant, with $r_{32} = (n_2/n_3)^{1/3} = r_{21} = (n_1/n_2)^{1/3} \sim 1.3$. Figure 3.12 illustrates the comparison between experimental data and the current numerical simulations, depicting trends in H^* , P^* , and η with respect to the flow coefficient Q^* .

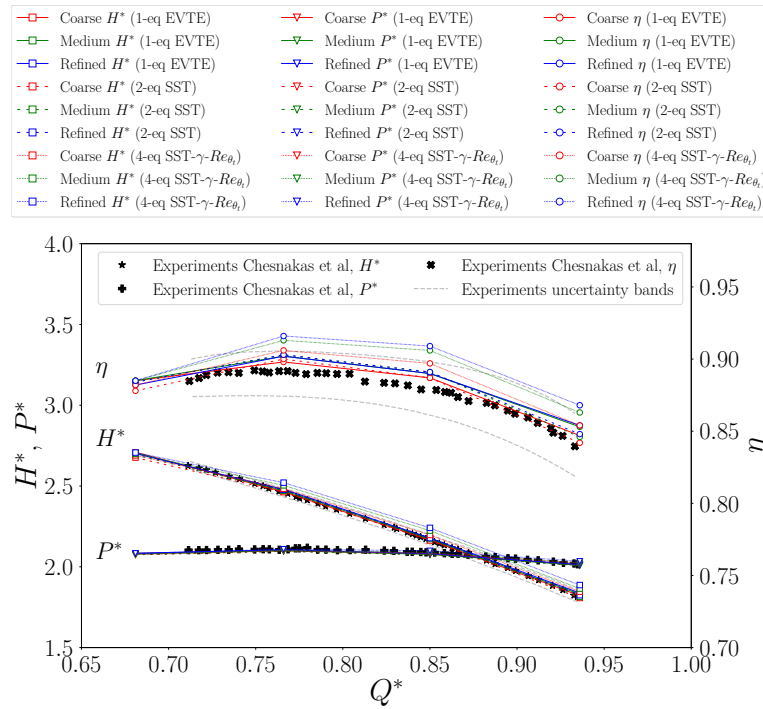


Figure 3.12: Head coefficient H^* , power coefficient P^* , and hydraulic efficiency as functions of flow coefficient Q^* . The CFD results, obtained with three different levels of grid refinement and three different turbulence models, are compared with experimental data [28].

When considering the 1- and 2- equation models, the results from the medium mesh configuration align entirely with those obtained from the finer mesh, indicating that the denser model does not significantly escalate computational expenses while delivering valuable improvements in accuracy. However, a minimal dependency on the variations in spatial resolution are evident between the coarse and medium levels. Overall trends across the curves display an underestimation of the torque applied to the rotor blade. Nevertheless, the head generated closely matches the experimental data. Consequently,

3. VALIDATION

the system hydraulic efficiency appears to be overestimated, reaching a discrepancy up to 1.4%. As regards the Transition SST, hydraulic performance suggest that the adopted discretisations are not yet such refined to provide grid independency. As a consequence, medium and refined grids solutions show head rise (and thus efficiency) estimations that are significantly higher than those obtained with the less resolute grid, up to values exceeding the experiments uncertainty bands.

Figure 3.13 provides an analysis of the $y^+ = \rho u_\tau y_w / \mu$ distribution across the rotor blade, serving as a high-level qualitative domain discretization metric. Here, ρ and μ represent flow density and viscosity, respectively. The wall friction velocity $u_\tau = \sqrt{\tau_w / \rho}$ is determined using $\tau_w = \mu \partial u / \partial y$, where y_w signifies the distance of the first-off-the-wall cell. The presented results cover all three turbulence models: EVTE (Figs. 3.13a, 3.13b and 3.13c), $k - \omega$ SST (Figs. 3.13d, 3.13e and 3.13f), and TSST (Figs. 3.13g, 3.13h and 3.13i). These evaluations are conducted across the three incremental refinement

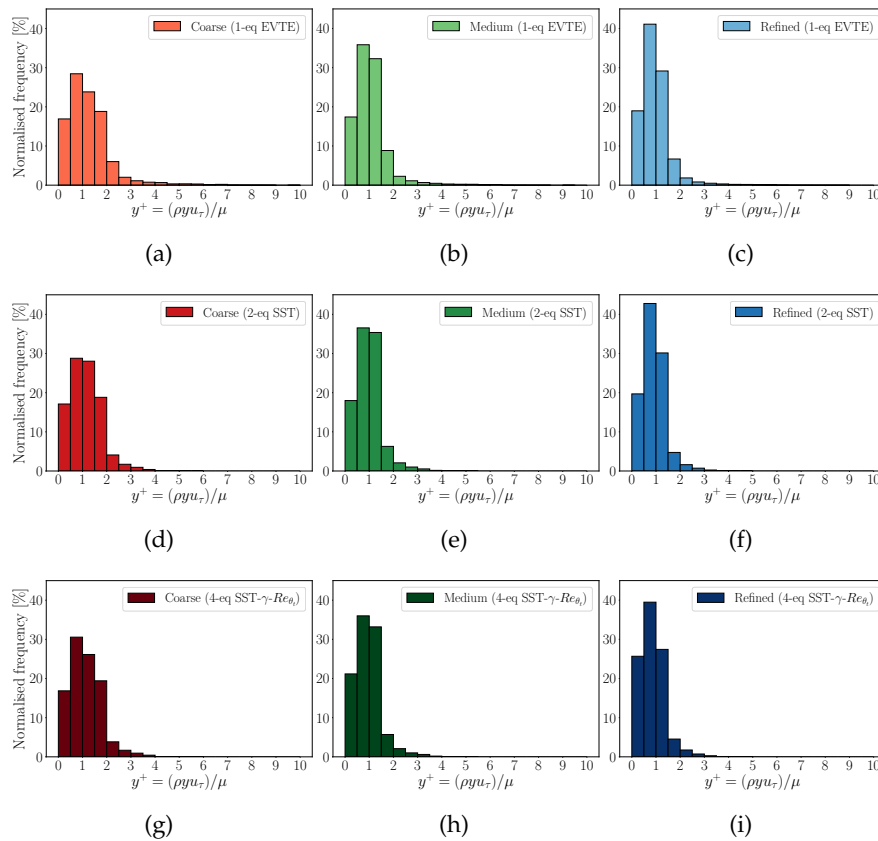


Figure 3.13: Computed normalised distributions of the y^+ on the rotor blade. Each row depicts histograms for every turbulence model (**top to bottom**) and every mesh refinement level (**left to right**).

levels. Histograms indicate that as the mesh becomes finer, the y^+ distribution

progressively centers around the median value, consistently remaining below 1. This reflects an accurate resolution of the boundary layer on the rotor surface. Particularly notable from the medium refinement and even more so from the finest refinement level, nearly 90% of the rotor cells cluster in the value categories up to 1.5. In addition to the y^+ distribution analysis, the local grid sensitivity is observed by examining the blade loading, focusing on pressure and viscous stresses. This evaluation involves the streamwise distribution of pressure and friction coefficients, represented as follows:

$$C_p = \frac{p - p_\infty}{\frac{1}{2}\rho u_\infty^2} \quad (3.27a)$$

$$C_f = \frac{\tau_w}{\frac{1}{2}\rho u_\infty^2} \quad (3.27b)$$

where p and p_∞ symbolise wall and free stream static pressure, and u_∞ represents free stream relative velocity. Load coefficients are observed across the rotor surface at three distinct span locations – near the hub, midspan, and tip (Fig. 3.14). Regarding the pressure coefficient, all three grids produce nearly identical distributions across all turbulence models, particularly evident at midspan (Fig. 3.14b) and tip (Fig. 3.14c), where the curves overlap. Minor distinctions are notable at the hub section (Fig. 3.14c), where enhanced discretization quality is observed due to local gradients generated by the curved hub shape. Concerning the viscous shear, a similar trend is observed; each configuration, irrespective of refinement or turbulence model, shows virtually the same wall-flow distribution at the hub (Fig. 3.14d) and shroud (Fig. 3.14f) blade sections. Slight variations are observed at the midspan (Fig. 3.14e).

Within this context, a pronounced discrepancy primarily arises due to the heightened discernment of laminar-to-turbulent transition points by the TSST model [72]. This distinctive effect significantly differentiates it from the other two models, which almost equivalently handle the flow. Consequently, this distinct formulation of equations permeates the entire load distribution, affirming that the solution sensitivity to the closure technique is unavoidable. Notably, the two extreme span sections display no deviations associated with transitional behaviours. This outcome can be attributed to the profound impact of the casing boundary layer on the corresponding flow evolution. Such influence mitigates the usual development observable at the midspan, where the blade section more closely resembles an aerofoil in free-stream conditions.

As additional metrics for the present model accuracy, hub-to-shroud distributions of significant circumferential-averaged flow quantities are adopted to compare between numerical results and available LDV measurements [28] at different axial locations (Fig. 3.15). The flow at inlet station depicts an undisturbed shape, with the only influence of the casing boundary layer (Fig. 3.15a). For the major part of the channel the velocity equals the area averaged value, which is indifferently observable from all the mesh refinements and turbu-

3. VALIDATION

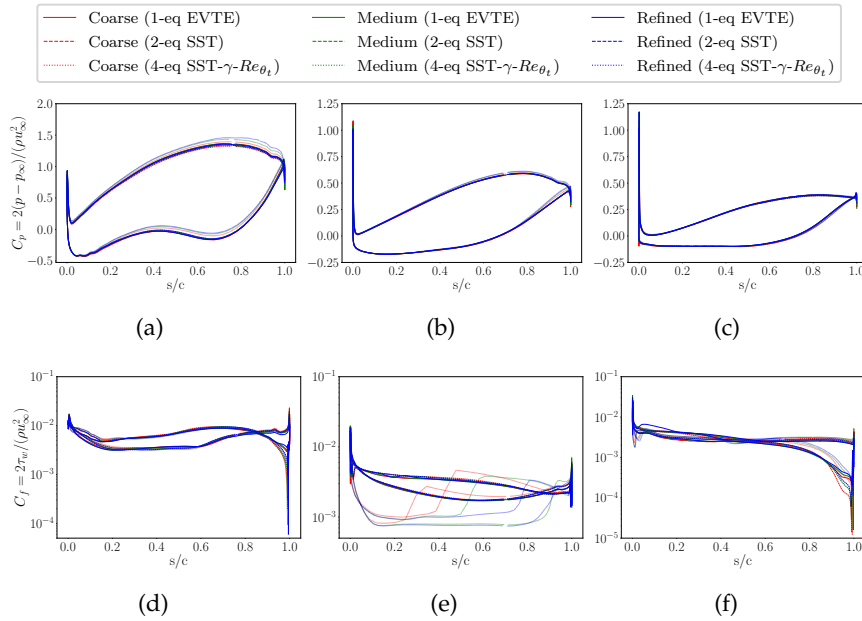


Figure 3.14: Sectional distribution of pressure (a–b–c) and skin friction (d–e–f) coefficients for three different spans, respectively: hub (a–d), mid (b–e) and blade tip (c–f). Each plot includes values obtained with the three turbulence models considered.

lence models, thus recovering the same curve as in the experiments, despite the different flow coefficient considered ($Q^* = 0.783$ by Chesnakas et al. [28] and $Q^* = 0.85$ from present computations). Even at the outlet station, good agreement with measurements is obtained when considering the axial velocity (Fig. 3.15b), except for a slight underprediction of the velocity in the wake dynamics. Again these variable shows no significant dependency on the spatial discretisation or the turbulence modelling technique. However a reduced fluctuation can be identified near span = 30%; the latter proving a minor local influence of the cells dimensions. The analysis of the velocity tangential component suggests instead a major impact of the numerical setup (Fig. 3.15c). In fact, by inspecting this quantity it is possible to infer that the more the grid is refined the more local fluctuations are detected around the experimental values. Conversely, the turbulence treatment induces only a slight shift on the trends modified by the discretisation. In general, it is difficult to recognise a pattern that drives the numerical solution depending on the combination between resolution and turbulence, except for the region at the lower span, below 10%. Here, in fact, the solution recovered by the EVTE is evidently overpredicted with respect to the measured flow, for any of the considered refinements, while the other two turbulence models are always more accurate. This aspect is particularly meaningful of the ability of the 1-equation model in capturing the wake dynamics, this portion being fully immersed in

the boundary layer detaching from the nozzle spinner wall (as evidenced by Figure 3.15b). Following the very accurate solution of the axial component, the behaviour of the swirl angle at the exit plane (Fig. 3.15d) results almost exclusively driven by c_U . As a consequence, the spanwise distribution traces nearly equally the one of the tangential component, thus leading to the same observations.

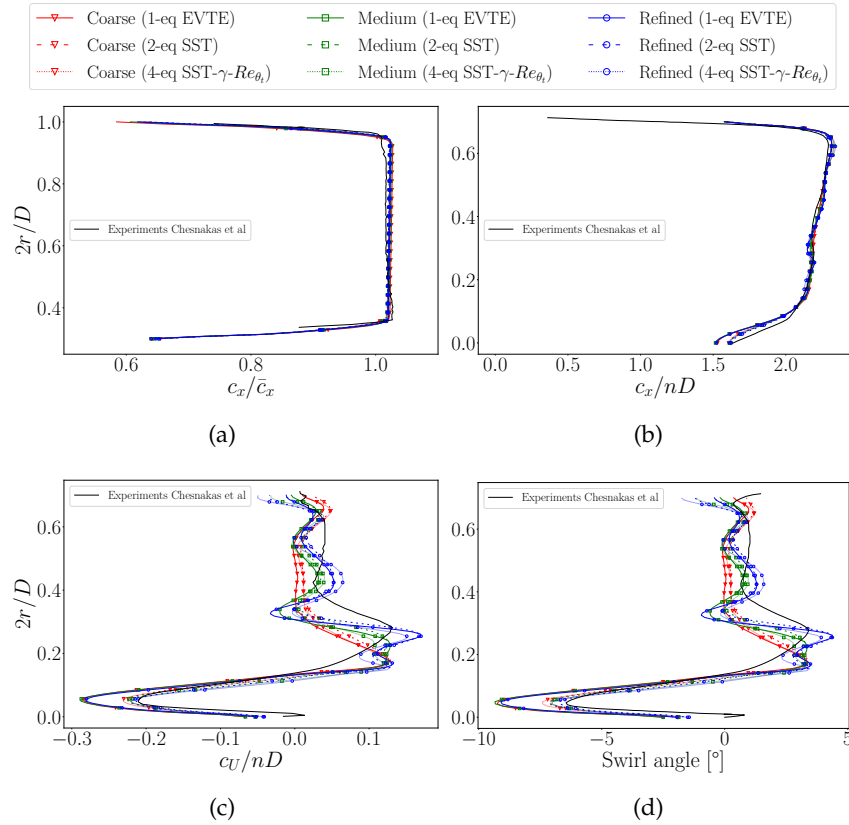


Figure 3.15: Hub-to-shroud distributions of circumferentially-averaged flow quantities at $Q^* = 0.85$, comparing present model with LDV measurements from Chesnakas et al. [28]. The values are extrapolated from the inlet (a) and exhaust (b, c, d) stations, and they represent either the axial (c_x) and tangential (c_U) normalised velocities and the swirl angle.

A visual comparison of the flow field is reported in Figure 3.16 through axial velocity contours on the exit plane, obtained from medium refinement at the flow condition $Q^* = 0.94$. As already evidenced by Chesnakas et al. [28], the CFD tends to overestimate the wake velocity deficit behind the spike, which appears further magnified when using the same range as in the experiment. In this regard, the numerical solution depicts no significant differences between the SST and the EVTE. Both the results show that the wake dynamics rapidly realigns with the higher values observed during

3. VALIDATION

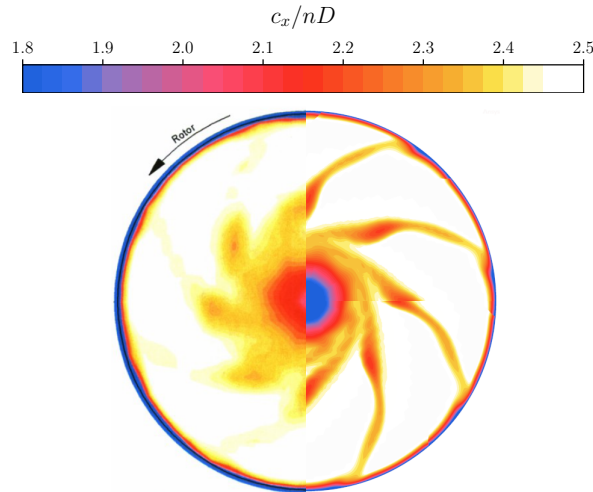


Figure 3.16: Axial velocity contours on the cross-section plane at the nozzle exhaust at $Q^* = 0.94$. Experimental LDV measurements (left half) adapted from Chesnakas et al. [28] are compared with numerical solutions obtained with the present model medium refinement, using $k - \omega$ SST (upper right quadrant) and EVTE (lower right quadrant) turbulence models.

tests measurements. However, the blades wakes confirm the propensity of the numerical model to exaggerate the viscous losses. In fact, the flow deceleration thickening near the midspan is considerably more emphasised in the present model. The same holds true for the remainder of the blades wakes up to the casing, which is instead barely detectable in the experimental LDV.

On the other hand, the streamwise velocity at the mid stage (aft of the rotor) suggests an overprediction of the blade-to-blade flow evolution at $Q^* = 0.77$ (Fig. 3.17). In fact, the numerical results depict a more restrained distribution of the blades wakes if compared with the experiments. The blades channels are mainly characterised by a higher velocity than the maximum value obtained during tests [28]. In terms of turbulence modelling, the SST and the Transition 4-equation variant are almost equivalent. The only peculiarity being the tendency of the second to recover a larger wake on the near-hub region, while reducing it in the proximity of the shroud. In any case, both the techniques agree in underestimating the effects of the tip leakage flow, which is responsible for the boundary layer region near the casing, close to the suction side of the blades.

Moreover, the application of the Grid Convergence Index (GCI) [24] is employed to evaluate the impact of grid discretisation errors on cavitation prediction under fully cavitating conditions. This method involves the selection of two quantities denoted as φ_k , where k signifies the refinement level. These values are assigned as local and integral cavitation-related variables: the estimated length of the vapour bubble on the Suction Side (SS), l_B , and

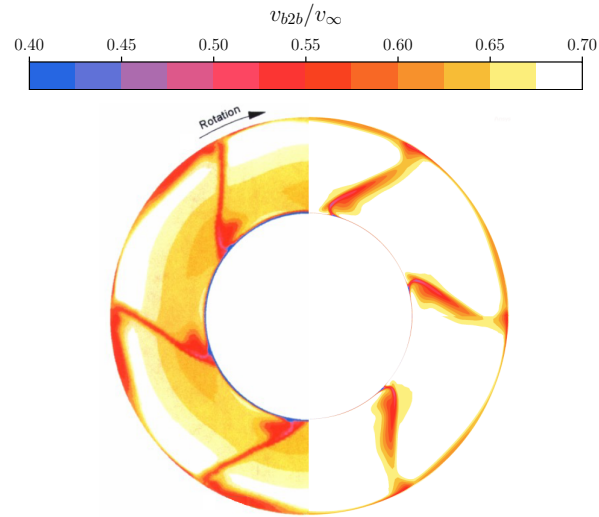


Figure 3.17: Blade-to-blade velocity contours on the cross-sectional plane at the mid stage, just aft of the rotor, at $Q^* = 0.77$. Experimental LDV measurements (left half) adapted from Chesnakas et al. [28] are compared with numerical solutions obtained with the present model medium refinement, using $k-\omega$ SST (upper right quadrant) and TSST (lower right quadrant) turbulence models.

the normalised volume of vapour within the pump domain, V_{vap} , respectively. The l_B measurement represents the normalised streamwise distance between two locations on the blade surface where $\alpha_v = 0$. Meanwhile, V_{vap} includes the volume of cells where $\alpha_v > 0.1$ and is subsequently normalised against the coarse grid result. The GCI parameters for both medium (GCI_{medium}^{32}) and fine refinement (GCI_{fine}^{21}) are presented in Table 3.1. These values include the extrapolated variables, φ_{ext} , and error, e_{ext} . Considering the outcomes derived from model tuning and validation, the medium resolution is chosen as an optimal balance between precision and computational costs. Regarding turbulence modelling, the preceding outcomes indicate that opting for the one-equation EVTE model instead of the two-equation SST model does not provide any notable advantages. Consequently, in this context, the selection is steered by well-established research studies found in the existing literature [78, 128, 50, 130, 79]. As a result, subsequent examinations of the system under cavitation conditions have been executed using this specific numerical configuration.

Thrust breakdown

After confirming the validity of the numerical model, the system response under cavitation conditions is initially examined through thrust breakdown simulations, followed by a comparison with accessible experimental and numerical findings (Fig. 3.18). Following the test protocol delineated by

3. VALIDATION

Table 3.1: Grid discretisation error for the cavitation statistics. The local and global variables are, respectively: the length of the vapour bubble on the Suction Side (SS), l_B , and the vapour volume normalized with the corresponding value from the coarse mesh, V_{vap} .

	l_B	V_{vap}
φ_3	0.813	1
φ_2	0.761	0.881
φ_1	0.757	0.889
φ_{ext}^{32}	0.757	0.872
e_{ext}^{32}	0.006	0.010
GCI_{medium}^{32}	0.726%	1.227%
φ_{ext}^{21}	0.757	0.890
e_{ext}^{21}	0.005	0.001
GCI_{fine}^{21}	0.058%	0.083%

Chesnakas et al. [28], a gradual reduction in the total pressure at the inlet is conducted while maintaining a constant flow rate at $Q^* = 0.83$. The pressure reduction is quantified through a non-dimensional cavitation coefficient, defined as:

$$N^* = \frac{p_{t3} - p_v}{\rho(nD)^2} \quad (3.28)$$

Here, p_v represents the water vapour pressure. Throughout the computational iterations, the rotor angular velocity remains fixed at $n = 2000$ rpm. The recorded values are normalised with their corresponding parameters, H_0^* (Fig. 3.18a) and T_0 (Fig. 3.18b), obtained under non-cavitating conditions ($N_0^* = 3.283$).

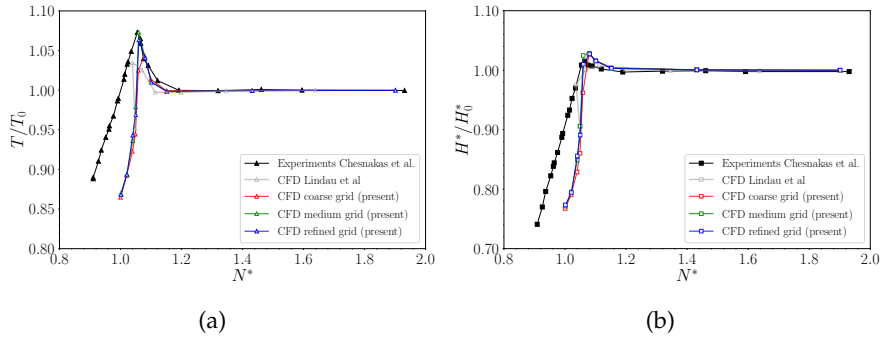


Figure 3.18: Normalised torque, T/T_0 (a), and head coefficient, H^*/H_0^* (b), as a function of the cavitation coefficient, N^* . Reference values T_0 and H_0^* are evaluated in non-cavitating conditions ($N^* = 3.283$). Grid dependency of the present numerical model is compared with available experimental [28] and CFD [76] data.

The test data trends illustrate that both torque and head coefficient generally increase during the initial stages of cavitation until approximately $N^* = 1.06$. At this phase, as detailed by Tan et al. [119] and Chen et al. [25], cavitation begins to affect part of the suction side of the rotor blade, where the pressure is close to the vapour pressure. Simultaneously, the Pressure Side (PS) remains unaffected by cavitation. Consequently, even though the pressure in the blade passage decreases, the partial cavitation on the SS results in heightened blade loading and increased work output by the pump.

The performance curves demonstrate the model significant ability to capture these operational conditions, even when compared with other CFD outcomes. The torque ramp-up phase closely aligns with the experimental curve, except for a slight offset in the initial segment. This trend is observed across the three refinements; however, a notable difference arises in the predicted peak load, notably between the coarse level and the finer ones. The refinement reduces the error from $>4\%$ to $<1\%$ under these conditions. This reduction stems from an earlier anticipation of cavitation breakdown. Regarding the head coefficient, the model behaviour is distinct from nominal conditions. It consistently overestimates the energy imparted to the fluid in the initial phase. Consequently, the peak condition is higher than the measured value and nearly independent of the mesh, with the error restricted to about 1%.

As N^* decreases and both T and H^* steeply decline, the numerical model notably diverges from the test data. This similar trend is observable in the CFD results highlighted by Lindau et al. [76]. These deviations were initially proposed by Chesnakas et al. [28] and later verified by Tan et al. [119] and Chen et al. [25]. The reduction in the inflow pressure for the breakdown test initiated cavitation in the tunnel impeller, which subsequently decreased the circulating mass flow rate. As a result, the measured breakdown values were normalised using performance values obtained at the equivalent flow coefficient under non-cavitating conditions. Therefore, discrepancies in the numerical results are attributed to two simultaneous effects: the imposed boundary conditions do not align with the experimental flow conditions, and the reference values for normalisation are not adjusted based on the actual measured mass flow rate.

For a visual evaluation, Figure 3.19 presents graphical comparisons between images of cavitation volumes in the tip region from Chesnakas et al. [28] and the isosurfaces of vapour volume fraction ($\alpha_v = 0.3$) derived from the present model. The images in Figures 3.19a and 3.19b exhibit low cavitation conditions confined to the blade tip, while Figure 3.19c depicts the performance ramp-up phase preceding the thrust breakdown.

The observations made through flow visualisation indicate that the model portrays a vapor volume distribution that closely resembles the patterns observed in experimental images, particularly in the attached sheets along the span on the SS. However, the computations fall short in accurately reconstruct-

3. VALIDATION

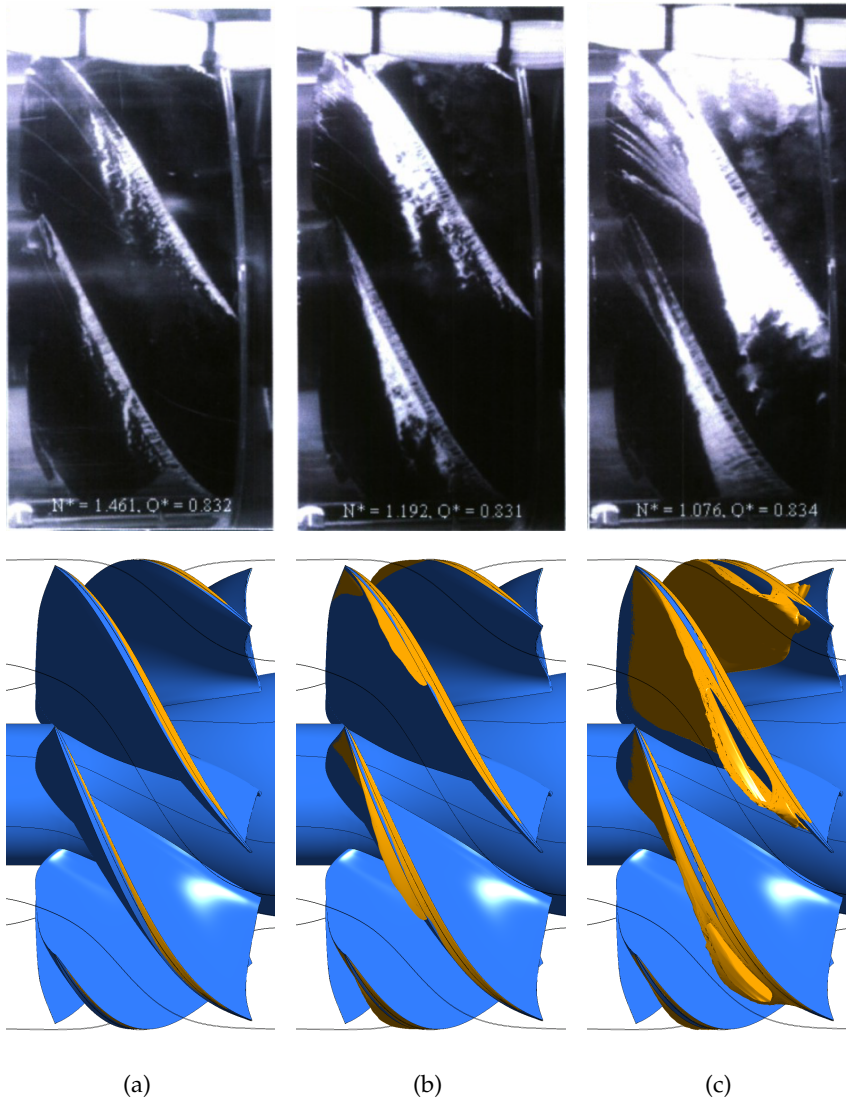


Figure 3.19: Tip leakage cavitation, visualised through isosurfaces of volume fraction $\alpha_v = 0.3$. Pictures reported by Chesnakas et al. [28] are compared with the CFD results for three different flow conditions: (a) $N^* = 1.461, Q^* = 0.83$. (b) $N^* = 1.193, Q^* = 0.83$. (c) $N^* = 1.076, Q^* = 0.83$.

ing the cavitation bubbles linked to the TLV, particularly near the TE. This specific flow characteristic was extensively studied by Guo et al. [50]. According to their research, proper reconstruction of the vortex necessitates unsteady simulations with a unique adaptation of the cavitation model. However, such a detailed analysis of this structure goes beyond the scope of the present study. In the calibration phase, the model modifications proposed by Guo et al. [50] were tested. In a steady computational approach, their adjustments did not notably enhance the results obtained with the default cavitation model, and

this investigation is not detailed here.

Cavitation model sensitivity

The outcomes from the analysis of thrust breakdown distinctly reveal the complexities involved in accurately depicting these phenomena via numerical methods in the CFD model. Consequently, the subsequent investigation aims to fine-tune the parameters of the cavitation model to better align with the experimental results. Specifically, multiple empirical coefficients are adjusted to assess their individual impact on the phase transfer within the fluid mixture. Each coefficient is systematically altered and discussed while maintaining the remaining parameters at their default values. The analysis of these coefficient modifications focuses on three key aspects: the vapour volume at the rotor tip, the load distributions on the rotor blade, and the pump performance concerning N^* . The numerical solutions are extracted from an operational point with $Q^* = 0.83$ and $N^* = 1.076$, providing insights into the load distribution of the impeller at the 99% span. This examination tracks the pressure coefficient, C_p , as it varies depending on the normalised streamwise direction s/c , starting from 0 at the Leading Edge (LE) to 1 at the Trailing Edge (TE).

As outlined by Equation 3.16, the condensation coefficient, F_{cond} , represents an empirical factor that regulates the mass transition rate from vapor to water at interfaces where $p > p_{vap}$. Lowering this parameter effectively refines the liquid phase mass transfer equation, leading to an expansion of the vapour regions. This alteration can be observed through the vapour volume fraction contours over the blade tip, as depicted in Figure 3.20. The solutions are computed at $N^* = 1.076$ for various F_{cond} values: 10 (Fig. 3.20a), 1 (Fig. 3.20b), 0.1 (Fig. 3.20c), and 0.001 (Fig. 3.20a), each denoting a different factor applied to the default value.

Raising the condensation coefficient value constrains the extent of the vapor region interface to a distinct area primarily over the SS. The contours indicate that this adjustment is comparatively less effective than the default value. This observation is reinforced by the blade loading trend displayed in Figure 3.21, revealing that the curves for increased and standard coefficients almost overlap.

Reducing the value of the condensation coefficient by an order of magnitude significantly expands the spatial distribution of the vapour phase over the SS of the blade. Further reduction extends the vapour bubble to the PS of the neighbouring blade, thus impeding flow in the blade passage. This obstruction increases the relative velocity, reigniting the cavitation process. This development justifies the nonlinear behaviour of flow changes due to the coefficient variation. The load on the PS of the blade is also affected at this stage, resulting in a general decrease in shaft power due to the offloading on

3. VALIDATION

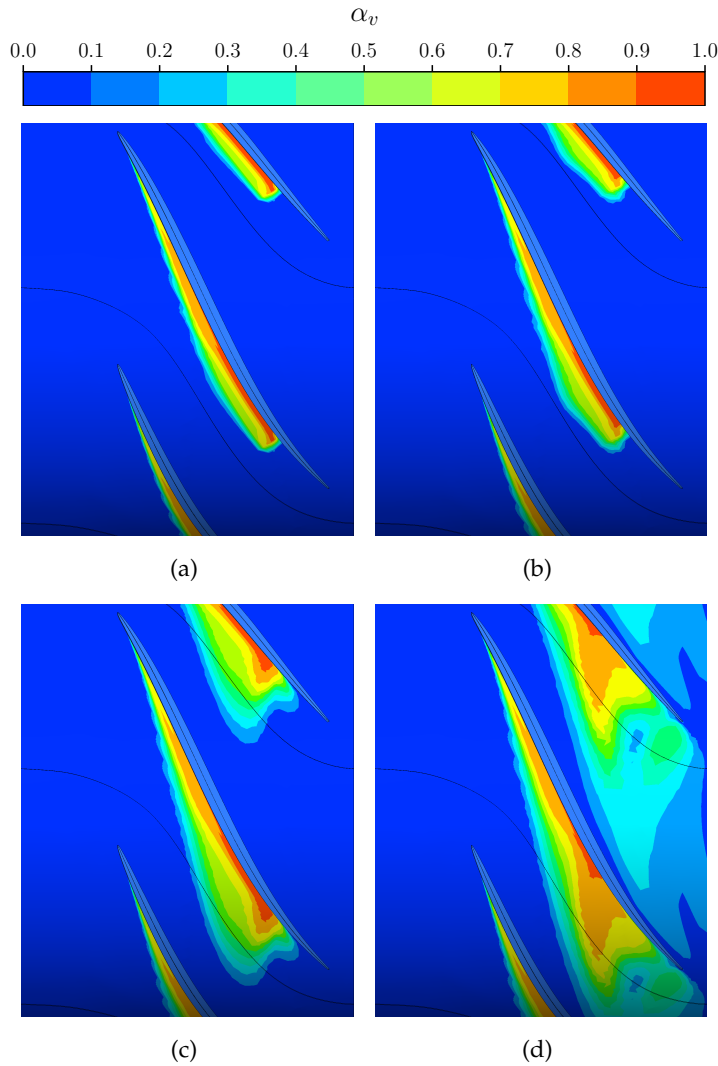


Figure 3.20: Influence of the condensation coefficient on the vapour volume fraction at the rotor tip (span 99%). (a) $F_{cond} = 0.1$. (b) $F_{cond} = 0.01$ (default). (c) $F_{cond} = 0.001$. (d) $F_{cond} = 0.0001$.

the SS. The pressure distribution transitions from an abrupt phase change to a gradual recovery as mass transfer smooths with the condensation coefficient decrement. Consequently, the pure vapour region expands with F_{cond} , while the field is dominated by the mixture with limited unitary volume fraction portions. The blade loading reversal near the trailing edge reduces, affected by the mixing with the partially vaporised wake.

During the breakdown loop, the significant vapour increase from lower condensation coefficient values leads to a substantial discrepancy between measured and predicted performance (Fig. 3.22). This intensified cavitation effect results in an expected decline in machine statistics. Predicted curves

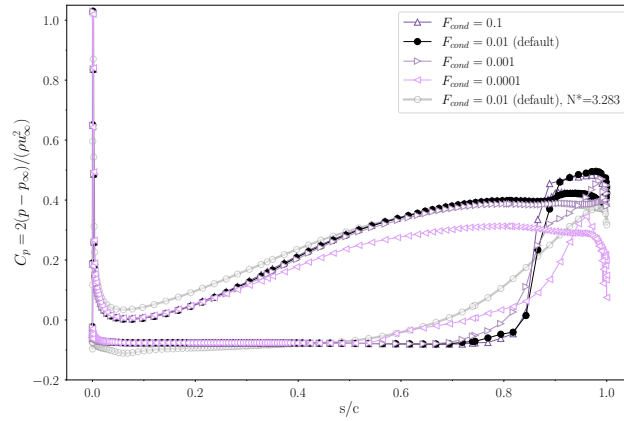


Figure 3.21: Influence of the condensation coefficient F_{cond} on the blade loading, at span 99%. The pressure coefficient is plotted as a function of the normalized streamwise direction s/c , where 0 is the LE, and 1 is the TE. Different values of F_{cond} are compared under cavitating conditions, $N^* = 1.076$. The blade loading under non-cavitating conditions, $N^* = 3.283$, is plotted as a reference.

deviate more from the experimental ones as F_{cond} decreases. Only for the highest values does the peak performance align well. This holds particularly true for shaft power (Fig. 3.22a), while the head coefficient (Fig. 3.22b) is in excess despite matching in terms of N^* .

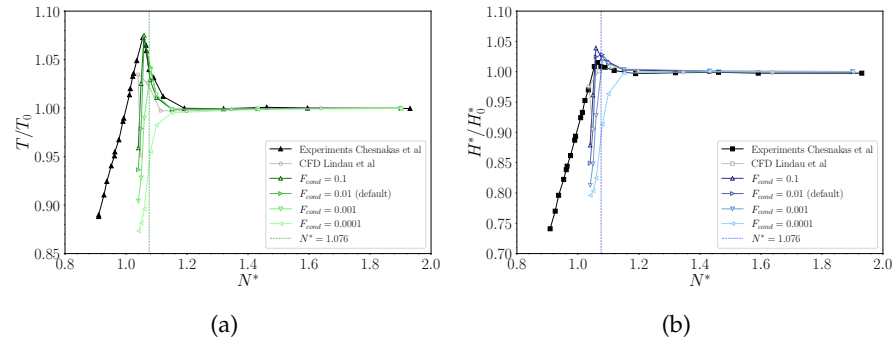


Figure 3.22: Influence of the condensation coefficient on the pump performance. Normalized torque, T/T_0 (a), and head coefficient, H^*/H_0^* (b), as a function of the cavitation coefficient, N^* , compared with available experimental [28] and CFD [76] data.

Regarding the flow evolution at full breakdown conditions, the model demonstrates behaviour similar to the previous sections, wherein the discrepancy between the imposed and tested mass flow rates is the primary cause of the overestimated steepness in the performance decay.

Equations 3.15 and 3.16 indicate that a reduction in the nucleation site ra-

3. VALIDATION

dius intensifies the rate of mass change. Consequently, this factor significantly influences the phase transition during both the evaporation and condensation processes (Fig. 3.23). By smoothing the transport mechanisms at the phase interface, an increase in R_{nuc} tends to limit the growth of cavitation bubbles. This leads to the emergence of vapour regions that are more widespread and characterised by low values of the volume fraction (Figs. 3.23a and 3.23b). Moreover, this adjustment results in a backward shift of the cavitation sheet along the blade Suction Side. As the coefficient increases, the inception of the two-phase region moves upstream, gradually departing from the trailing edge (Figs. 3.23c and 3.23d).

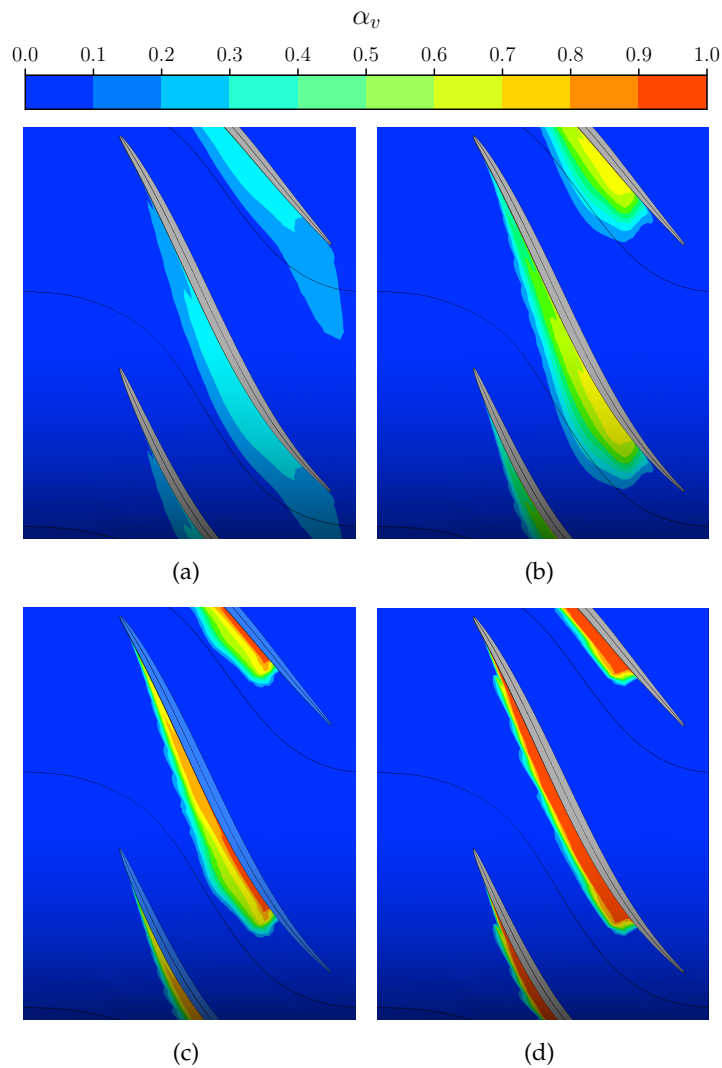


Figure 3.23: Influence of the nucleation site radius on the vapour volume fraction at the rotor tip (span 99%). (a) $R_{nuc} = 1 \times 10^{-4}$ m. (b) $R_{nuc} = 1 \times 10^{-5}$ m. (c) $R_{nuc} = 1 \times 10^{-6}$ m (default). (d) $R_{nuc} = 1 \times 10^{-8}$ m.

This progression illustrates an overall decrease in the spatial distribution of the vapour fraction. As the mass transfers intensify between evaporation and condensation, the local gradients of the phase change interface escalate quickly. Consequently, the transition becomes sharply defined, leading to a denser concentration of vapour but confined to a significantly narrower region. This flow development through the blade passage notably influences the rotor loading (Fig. 3.24).

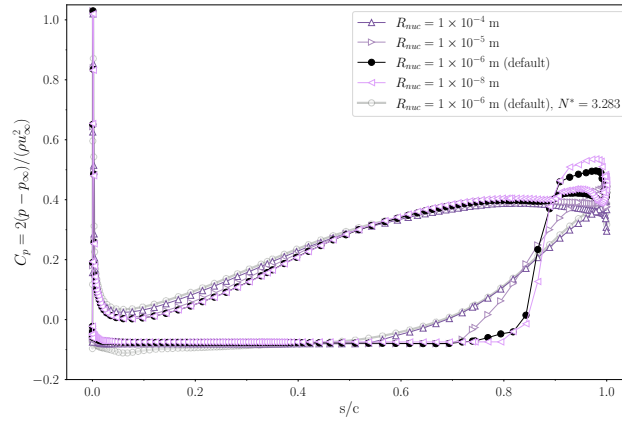


Figure 3.24: Influence of the nucleation site radius R_{nuc} on the blade loading, at span 99%. The pressure coefficient is plotted as a function of the normalized streamwise direction s/c , where 0 is the LE, and 1 is the TE. Different R_{nuc} values are compared under cavitating conditions, $N^* = 1.076$. The blade loading under non-cavitating conditions, $N^* = 3.283$, is plotted as a reference.

The impact on vapour volumes corresponds to outcomes similar to those discussed in the prior section; however, the pressure field exhibits distinct characteristics. As the cavitation region widens due to the increasing coefficient value, the low concentration of vapour is insufficient to create significant obstructive consequences. Consequently, the pressure coefficient over the PS of the blade remains largely unaffected, except for minor fluctuations attributed to the previously mentioned backward shift of the sheet. These fluctuations are more noticeable away from the mid-chord location, while at that point, all the curves are aligned. In general, with the rise of R_{nuc} , the flow evolution tends to increase the loading in the fore half of the blade and simultaneously decrease it towards the aft. When focusing on the behaviour on the SS, the pressure coefficient curves show a comparable trend to that observed earlier. With the promotion of mass exchange between the two phases, the cavitation volume tends to extend over a larger portion of the blade but with a reduced extension through the passage. This condition highlights the sharp interface by the rapid deviation of C_p towards the TE, where flow mixing in the wake occurs following a limited region with a load reversal.

Figure 3.25 depicts the pump performance evolution through a break-

3. VALIDATION

down loop. Similar to the aforementioned observations, the variation in the model coefficient results in an expansion of the vapour volume, leading to a decrease in statistics at higher values of the cavitation parameter N^* . Despite the sensitivity not altering the general curve shape, an earlier breakdown corresponds to reduced hydraulic peak performance in both torque (Fig. 3.25a) and head (Fig. 3.25b) .

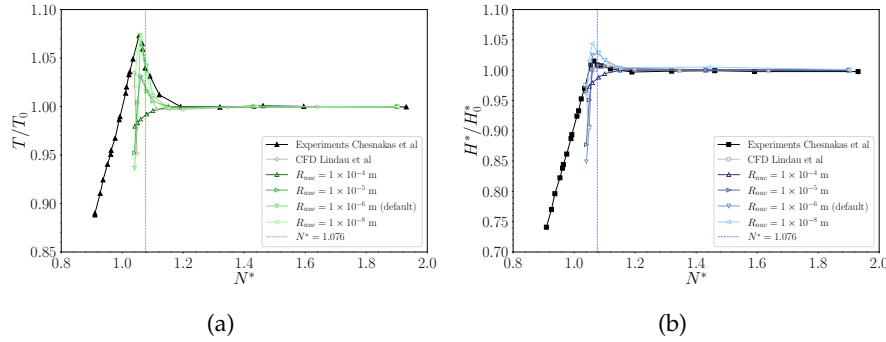


Figure 3.25: Influence of the nucleation site radius on the pump performance. Normalized torque, T/T_0 (a), and head coefficient, H^*/H_0^* (b), as a function of the cavitation coefficient, N^* , compared with available experimental [28] and CFD [76] data.

Again, achieving enhanced accuracy in predicting rotor load leads to a simultaneous underestimation of pressure rise. Decreasing the value of R_{nuc} results in aligning the rotor peak load with experimental measurements, showing a gradual insensitivity to the modification factor. Conversely, estimates of pressure rise exhibit a significant match when the nucleation site radius is increased by one order of magnitude. This alteration reduces the relative error for all points related to the initial breakdown phase, minimising it from a maximum of $>9\%$ to about 5% . However, this change diminishes the rotor loading, confirming the model tendency to overestimate the pump head rise capacity.

This behaviour is particularly associated with the TLV flow evolution (Fig. 3.26) . Comparing an increased value of R_{nuc} to 1×10^{-5} (Fig. 3.26c) against default conditions (Fig. 3.26a) , it appears to yield a vapour distribution that better aligns with experimental observations (Fig. 3.26c) , especially at the blade tip, consequently improving the prediction of average total pressure. Nevertheless, this adjustment leads to an overall reduction in load across the blade surface. Hence, the model efficiency estimate does not improve, maintaining higher values than those observed in experiments. This outcome arises from modifying a parameter that influences both condensation and vaporisation processes, suggesting that enhancing accuracy may necessitate a combination of coefficient alterations.

The vaporisation coefficient stands as another key parameter in fine-tuning

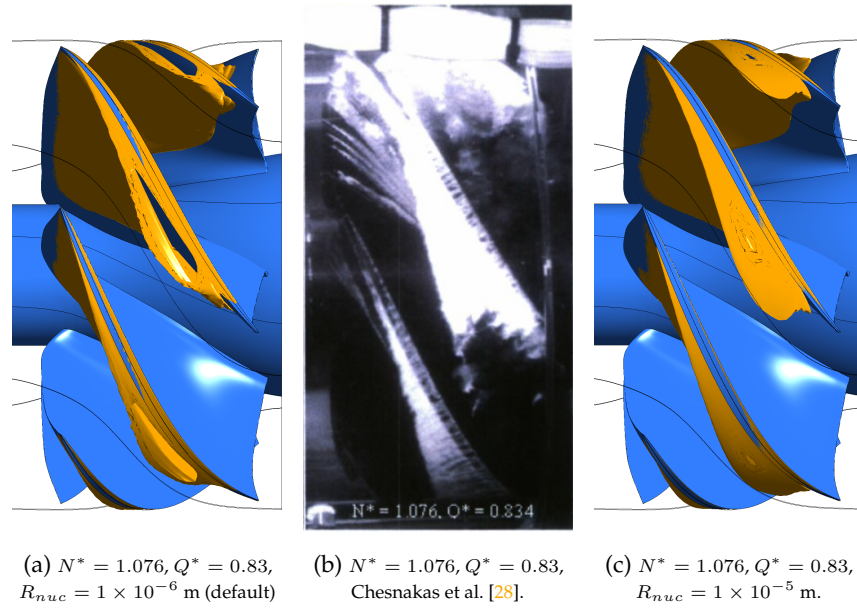


Figure 3.26: Comparison of the cavitation in the impeller for different values of nucleation site radius: $R_{nuc} = 1 \times 10^{-6}$ m (default) (a) and $R_{nuc} = 1 \times 10^{-5}$ m (c), concerning the experimental picture reported by Chesnakas et al. [28] (b).

the ZGB cavitation model. Described by Equation 3.15, this factor governs the phase transition from the liquid to the vapour state, influencing the interface phenomena within cavitation regions where $p < p_v$. Lower values of F_{vap} restrict the mass transfers toward the vapour phase, acting as a limiter for the vaporisation process. The distribution of the vapour field is illustrated in Figure 3.27. Here, the variation in the coefficient reveals a distinct trend. As the value increases from two (Fig. 3.27a) to one order lower (Fig. 3.27b), and then to one order greater (Fig. 3.27d) than the default (Fig. 3.27c), both the generation and extension of vapour are encouraged.

Hence, with the expansion of the bubble within the blade channel and over the SS, both the gas concentration and the interface sharpness intensify, significantly altering the model behaviour compared to the discussions in the preceding sections. In terms of the pressure distribution (Fig. 3.28) near the blade tip walls, the trend on the SS remains consistent up to the region at 0.6 in normalised streamwise coordinates. For $F_{vap} = 0.5$, the curve experiences a sudden departure with a marked rise that is swiftly mitigated. The transition towards the TE occurs with a smoother progression. However, a slight change in the blade loading is barely evident with a reduction in the coefficient by one order of magnitude. Except for a slightly diminished extent of the vapour region, the phase transition resembles the curve obtained under default conditions.

3. VALIDATION

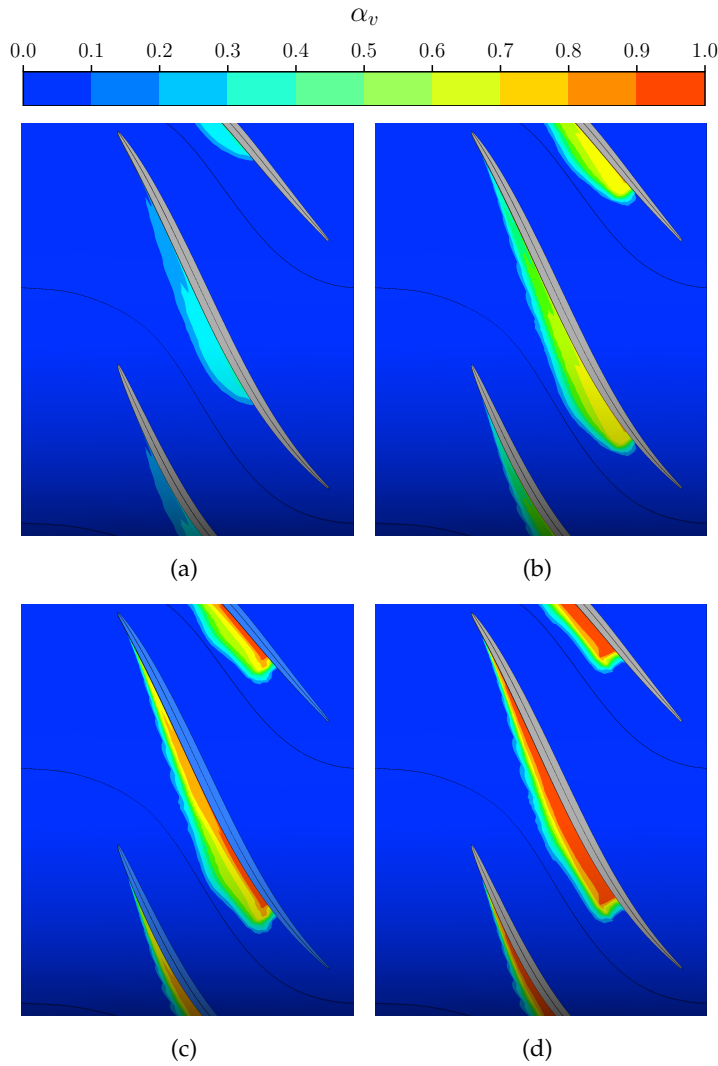


Figure 3.27: Influence of the vaporization coefficient on the vapour volume fraction at the rotor tip (span 99%). (a) $F_{vap} = 0.5$. (b) $F_{vap} = 5$. (c) $F_{vap} = 50$ (default). (d) $F_{vap} = 500$.

For larger F_{vap} values, the curve shares similarities with the reference curve, both exhibiting a reversed load on the restricted terminal blade segment. Meanwhile, the PS demonstrates minimal sensitivity to cavitation behaviour, apart from a limited region before the mid-chord. Here, a marginal pressure excess compared to the reference curve is swiftly reduced as the coefficient increment reverts F_{vap} closer to default values.

The preceding observations have a notable impact on the pump performance throughout the breakdown loop (Fig. 3.29). The restraint imposed by reducing the vaporisation coefficient on the vapour generation process delays the development of the cavitation bubble. Consequently, the rotor can with-

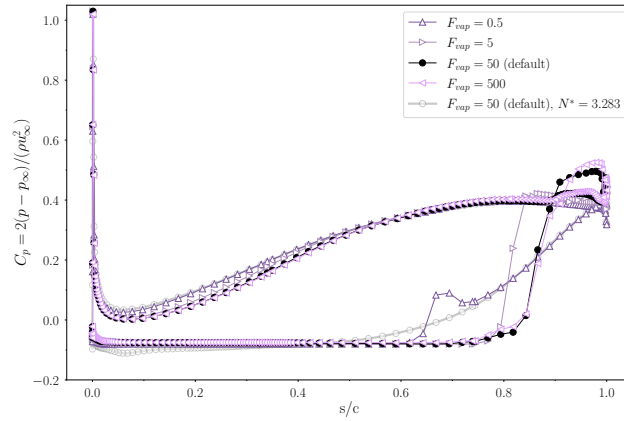


Figure 3.28: Influence of the vaporization coefficient F_{vap} on the blade loading, at span 99%. The pressure coefficient is plotted as a function of the normalized streamwise direction s/c , where 0 is the LE and 1 is the TE. Different values of F_{vap} are compared under cavitating conditions, $N^* = 1.076$. The blade loading under a non-cavitating condition, $N^* = 3.283$, is plotted as a reference.

stand lower inlet pressures, causing the peak performance and its subsequent decline to shift towards smaller values of N^* .

The lowest coefficient considered, $F_{vap} = 0.5$, notably levels off the peak performance. This effect results in the curve remaining relatively unchanged as the cavitation coefficient decreases. Conversely, the increasing trend observed in the initial stages of cavitation is sustained to such an extent that the decay in torque (Fig. 3.29a) and head (Fig. 3.29b) extends well beyond the simulated values of N^* .

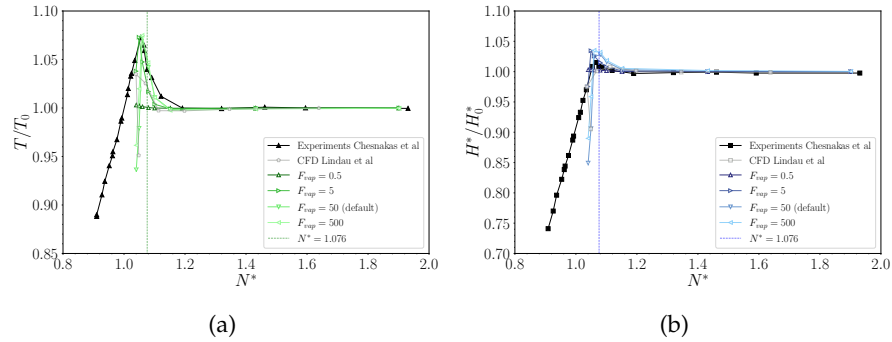


Figure 3.29: Influence of the vaporization coefficient on the pump performance. Normalized torque, T/T_0 (a), and head coefficient, H^*/H_0^* (b) as a function of the cavitation coefficient, N^* , compared with available experimental [28] and CFD [76] data.

In terms of the other parameters considered, no significant impact on the performance values can be discerned. Instead, the observed trend is a leftward

3. VALIDATION

shift in the curves, indicating peak performance occurring at lower inlet pressure values. This aspect underlines a highly non-linear dependency on the vaporisation coefficient. The differences are substantial when transitioning from 0.5 to 5; however, for higher values, the variations are minimal. This analysis confirms the model independence from F_{vap} for values larger than the default, which remains consistent across a wide range of operating conditions.

3.4 Installed pump model

3.4.1 Computational model

Pump installation strategy

The isolated components discussed in the previous sections are integrated to compose a possible design for a ODW. As a first tentative configuration, the pump main geometry is left unchanged, while properly scaling the intake sizing to suitably host the bladed parts. Specifically, both the nacelle and plug outlines are uniformly re-sized to match, respectively, the rotor shroud and hub diameters. As a consequence, the scaling factors differ between the external cowl and the inner centerbody. However, these are applied isotropically in the two parts when considered individually, thus maintaining the geometrical ratios the same as in the reference model (Fig. 3.30). As for the axial alignment,

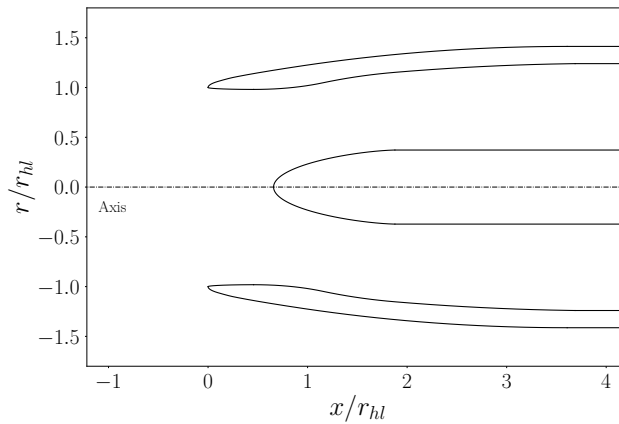


Figure 3.30: Manipulated outline of the intake for the installed pump configuration.

the rotor blade is positioned approximately $D/2$ downstream of the inlet aft end. This placement is chosen in light of ensuring a sufficient extension of the cylindrical sector, aimed at achieving uniform mass flow rate delivery to the pump. Following the principles drawn in Section 2.1, preliminary considerations through 1D equations are adopted to predict the main propulsive quantities of the system, when the pump is operating at design conditions

($Q^* = 0.85$). In fact, through imposition of the in-design volumetric flow rate, Q_J , it is possible to compute the advancing velocity, v_∞ , satisfying a chosen design IVR , as follows:

$$v_\infty = v_{hl}/IVR \quad (3.29)$$

$$v_{hl} = Q_J/A_{hl} \quad (3.30)$$

where the highlight area, A_{hl} , is assumed fixed once the nacelle geometry is obtained by the scaling process. Then, by neglecting inlet losses on first approximation, the pump upstream total pressure, p_t , at the Pump Interface Plane (PIP) equals the free-stream quantity:

$$p_{t,PIP} = p_{t,\infty} = p_\infty + \frac{1}{2}\rho v_\infty^2 \quad (3.31)$$

Thus, from the head rise design value the stagnation pressure at the pump exit is computed as: $p_{t,ex} = p_{t,AIP} + \rho(nD)^2 H^*$. Finally, by assuming the nozzle outlet plane adapted at the far-field ambient conditions, the exhaust velocity is derived from the total pressure relation defined at that location, as:

$$v_{ex} = \sqrt{\frac{2(p_{t,ex} - p_\infty)}{\rho}} \quad (3.32)$$

However, when the IVR is chosen as the intake design value, 0.85, the resulting velocity v_{ex} is not compatible with the continuity assumption through the pump:

$$Q_J = v_{ex}A_{ex} \quad (3.33)$$

if considering the exit plane area fixed by the nozzle geometry. It should be noted that, following this procedure, v_{ex} inherently results as a function of v_∞ , which is in turn regulated by the highlight velocity. With the volume flow rate being fixed, the only way to control v_{hl} is, ultimately, the size of the highlight radius. Specifically, satisfying the continuity would require an increment of the capture area, which is primarily endeavoured by adoption of the retracted plug configuration. Then, attempts to increase the highlight radius show that such operation is unattainable without stretching the outline to a shape that would discard the diffusion ability of the intake. Consequently, the decision is made to manipulate the nozzle size to honour continuity hypothesis. Then, using Equation 3.33, a proper exit radius is computed. To ensure the same smooth transition as the original spline, the area reduction is obtained by extending the nozzle length. The modified axial distance is evaluated by imposing the curve tangent at the common location with the baseline geometry. Then, the spline at the nozzle ending region is stretched up to the point matching the computed radius, and the cylindrical buffer is extended proportionally. The two geometries are compared in Figure 3.31 .

3. VALIDATION

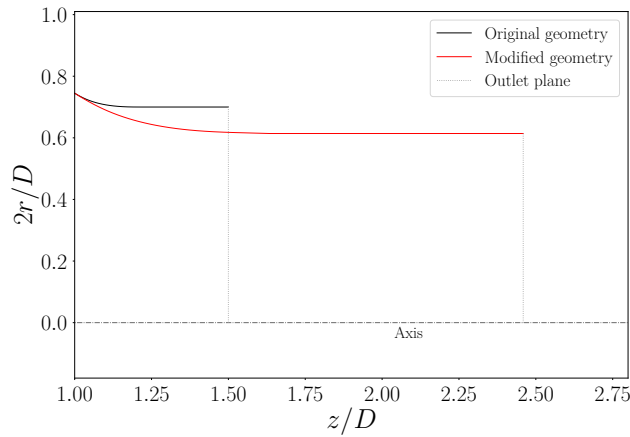


Figure 3.31: Outline of the terminal portion of the nozzle, comparing between original and manipulated geometry. The dimensions are normalised using the pump diameter, D .

Domain discretisation

The fluid domain is discretised following the strategies outlined in the previous sections (Fig. 3.32). The mesh surrounding the intake is generated through a rotational extrusion of the 2D grid. This leads to a mainly structured block, except for the elements along the axis of symmetry, which degenerate into wedges. In particular, the two-dimensional discretisation is sized starting from the extra coarse level mentioned in Section 3.2, by re-scaling the extensions in conformity with the modified dimensions and the cells number according to the ratio of the Reynolds numbers. The latter based on the undisturbed advancing speed and the highlight radius. In this way, the planar domain results discretised into $272k$ quads. The extrusion is then completed by enforcing the circumferential spacing of the rotor block. As a consequence, by taking advantage of the axis-symmetry, the resulting mesh encompasses only $1/6$ of the full fluid domain and matches the rotor block inflow. Concerning the latter, the starting point is the medium refinement as discussed in Section 3.3. The grid is cut $\sim 1D$ upstream of the rotor blade and regenerated while keeping the same walls spacing and normal expansions. Thus, the cylindrical buffer preceding the blade is included in the rotor block and is therefore solved as a rotating frame domain. Conversely, the stator mesh is taken from the isolated case medium discretisation without any further modifications.

As far as the outflow buffer, the grid generation is performed as previously discussed for the baseline, by adopting the modified nozzle geometry. Thus, two main sub-blocks compose the entire mesh. A major structured block on the external part of the channel is connected to a mixed cells region towards the axis, both taking the stator outflow domain as a reference elements distribution. The model assembly is reported in Figure 3.32a, which depicts

the surface discretisation over the propulsor walls. As far as the intake block, the planar periodic domain that generates the 3D computational field can be seen in Figure 3.32b , through a detailed view of both the wall- normal and tangential distributions near the the highlight. The entire computational domain retained for the computations accounts for 10.9 million cells overall.

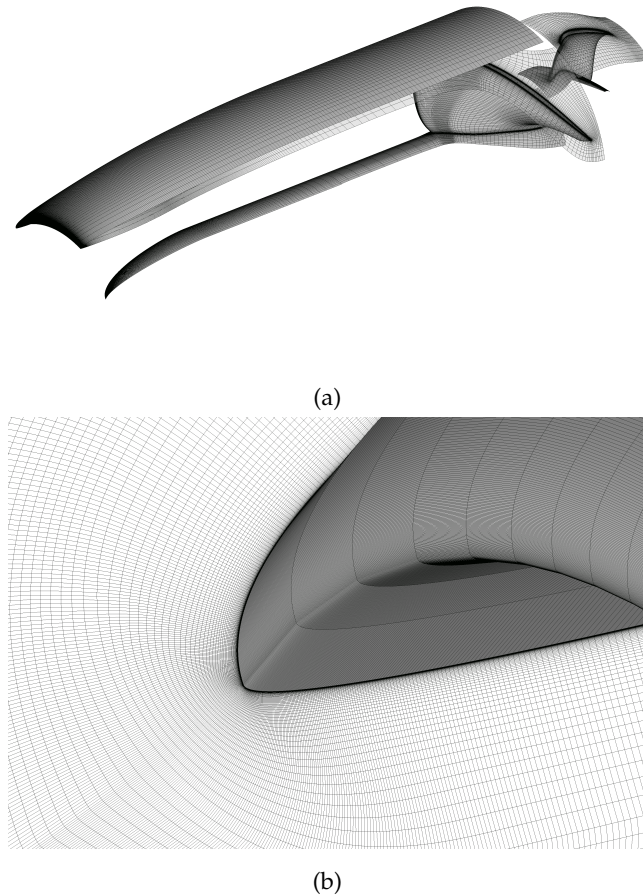


Figure 3.32: Details of the computational grid. **(a)** Full model walls' discretisation. **(b)** Zoom around the highlight region, with background mesh of the periodic domain.

Numerical schemes and boundary conditions

As for the isolated pump modelling, the Ansys solver CFX is adopted for computations. RANS equations are coupled with the SST turbulence model and phase transition is accounted for through the Zwart cavitation model. The latter implementing the modified nucleation radius ($R_{nuc} = 1 \cdot 10^{-5}$) due to the previously discussed ability in predicting the pressure field. High-resolution

3. VALIDATION

scheme is employed for advection and turbulence discretisation.

Selection of boundary conditions is mainly dictated by the preceding discussions. One main difference regards the PIP, where an interface is enforced instead of a mass flow rate to solve for the change in the reference frame, where the flow information is communicated from the stationary frame to the rotor rotating one. Specifically, since the upstream domain involves no phase variation, the Frozen Rotor technique is conveniently chosen according to its robustness and computational efficiency [2]. As a 3D domain, no axis boundary is now required. In fact, rotational periodicity is imposed on the planar domains defining the 60° section retained. Regarding the blocks around the pumps' blades, the boundaries are kept the same as in the isolated model. On the opposite, the outflow plane is set as a pressure outlet, which denotes a substantial difference with the separate component boundary condition. In the latter case, mass flow rate was imposed. However, this does not ensure to satisfy pressure adaption to ambient conditions, which is the expected behaviour of a submerged propulsor that collects the flow from and discharges it into the same incompressible environment. Points may be raised regarding the decision to consider the nozzle exit plane as the adaption section, thus excluding the further downstream vena contracta. However, this choice is acceptable for nozzles equipped with parallel throat [120], as the one analysed here. In fact, this is a common practice for CFD works where the waterjet system is investigated without modelling the free-stream domain behind the nozzle [22, 123, 49].

Computations are initialised through a single-phase converged solution at a given flow configuration. Then, the cavitation model is included in the RANS system and the two-phase field is computed. This approach reveals a difference with respect to the isolated case. In fact, starting from a mixture case and modifying the far-field conditions would result in numerical instabilities that would be hardly dissipated, unless a large number of iterations is permitted. In addition, the modelling of the intake far-field domain improves the stability of the numerical scheme. As a consequence, 200 iterations are sufficient to reach single-phase convergence with an auto timescale technique without the need to guide the solution with an initial local timescale approach. Within the same limit, even two-phase cases are solved. The convergence criterion, once again, is the standard deviation of the hydraulic efficiency, aiming to exceed the lower limit of $1 \cdot 10^{-3}$ over a moving interval of 40 iterations. Mass imbalances are verified to be well below 1%.

3.4.2 Results

To cover a broader range of operating conditions, three different rotational speeds are considered: 800, 1400, and 2000 *rpm*. Considering the chosen set of boundary conditions, once the ambient pressure is assumed fixed, the only

variable flow boundary to be determined is the advancing velocity. Following the procedure outlined in the installation strategy paragraph, the input value for the velocity inlet condition is recovered from Equation 3.30 for each rotor speed, after defining the non-dimensional design parameters. The design-velocity-based Reynolds numbers, Re_{hl} , corresponding to three regimes are, respectively: $9.75 \cdot 10^5$, $1.7 \cdot 10^6$ and $2.44 \cdot 10^6$. Then, the operating map is tracked by spanning over a range of advance ratios, $v_\infty/(nD)$, while keeping the same blade revolution speed. These are uniformly chosen as 9 cases between 60% and 140% (i.e. a 10% increment each) of the design condition.

At this flow configuration (Fig. 3.33) the stream tube enters the propulsor assuming a weakly divergent shape up to the capture section, thus denoting a slight pre-diffusion exerted on the free-stream. The resulting IVR is 0.84,

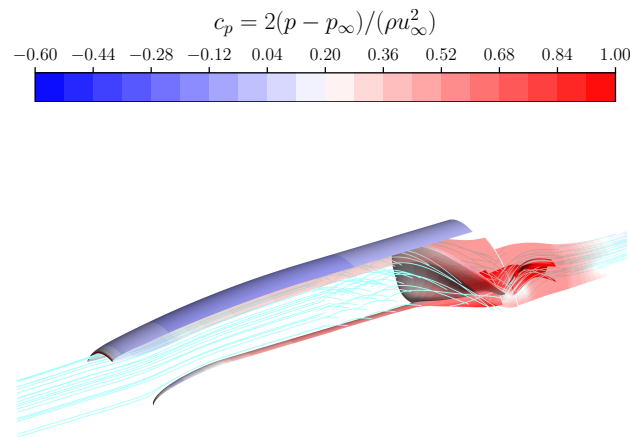


Figure 3.33: Contours of free-stream axial velocity–based pressure coefficient on the propulsor walls, superimposed with a single-channel streamlines distribution at near-design conditions. The flow field is extracted from the solution at $n = 2000 \text{ rpm}$ and $IVR = 0.84$.

which is very close to the value imposed on the 1D model adopted for the system coupling. The present result can be then considered as a numerical proof of the simplified approach in estimating the propulsor performance at installed configurations. In fact, the flow is re-directed to the pump rotor with a proper uniformity, thus allowing the machinery to process an optimally distributed mass flow that is oriented axially, along the thrust direction.

In Figure 3.34, hydraulic performance of the installed pump is analysed in detail, by comparing the present numerical outcomes with the ones obtained with the isolated configuration and, again, the experimental data from Chesnakas et al. [28]. To this purpose, the flow statistics are extracted from the same measurements stations. Effects of installation are here included by adding the computed IVR values as data tips, which contain the information

3. VALIDATION

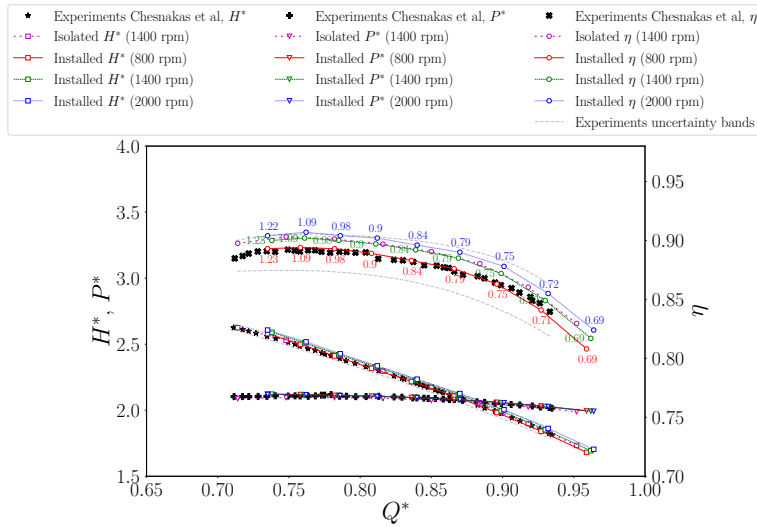


Figure 3.34: Head coefficient H^* , power coefficient P^* , and hydraulic efficiency as functions of flow coefficient Q^* . The CFD results, obtained at three different rotor speeds, are compared with experimental data [28] and previous numerical solution from isolated model. IVR values are added as data tips.

of the stream tube shape and thus the operating point. If compared with the isolated pump performance, it is possible to conclude that embedding the machinery inside the intake has negligible effects on hydraulics over the entire range investigated. Furthermore, it should be noted that the manipulation of the nozzle exhaust section induces no variations on the pump non-dimensional characteristic. However, the current analysis reveals a minor influence of Reynolds effects, with a maximum efficiency discrepancy of 0.5% from the slower regime to the medium. This value further reduces to 0.2% between the medium regime and the case at 2000 rpm . In general, the original trend is preserved and this affinity defect only causes an almost uniform shift of the curves. In this regard, the good agreement between performance maps at 800 rpm and experiments should be evaluated in light of the already mentioned tendency of the numerics to overestimate the pressure rise. Reynolds effect introduces additional losses that mitigate the numerical model behaviour and this, by chance, leads to magnitudes comparable with measurements. However, this observation highlights a significant impact of Reynolds effects, particularly accentuated at high mass flow rates, especially beyond $Q^* = 0.896$.

Following the principles of the TDB, the propulsive performance of the system is extracted (Fig. 3.35). The specific net thrust, $T_s = T/\dot{m}$, denotes a decreasing trend as the advance velocity grows. As a consequence, the mass flow rate processed by the propulsor augments more steeply than the corresponding thrust. At any rotor velocity considered, the curves depict a

3.4. INSTALLED PUMP MODEL

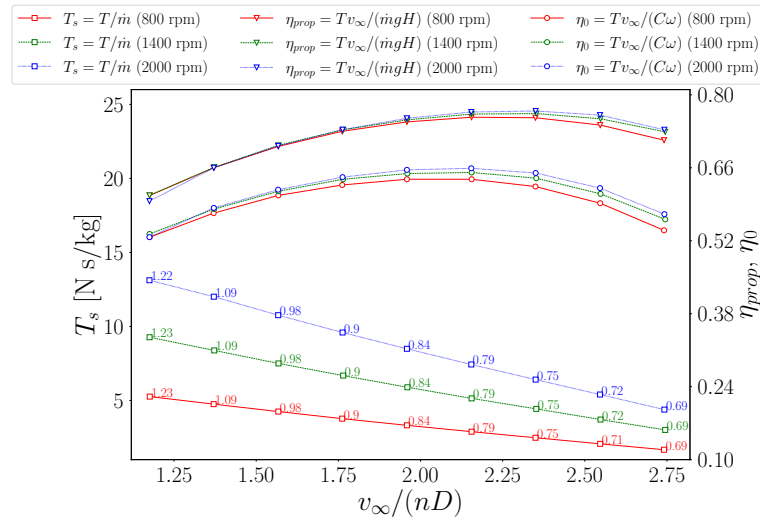


Figure 3.35: Specific thrust T_s , propulsive efficiency η_{prop} , and overall efficiency η_0 as functions of normalised advancing velocity. The CFD results are obtained at three different rotor speeds. IVR values are added as data tips.

smooth monotonic shape. However, these flatten with the rotational regime, denoting a non-linear influence of the rotor velocity in the specific thrust decay throughout the range. In fact, although the initial take-off cases, 1400 and 2000 *rpm* respectively, are characterised by about 2 and 3 times the slower map value, $T_s = 5.26 \text{ Ns/kg}$, all the three curves are confined between 1.67 Ns/kg and 4.38 Ns/kg at high-speed conditions. In general, the system denotes a significant efficiency, with the peak values reaching up to 0.77 and 0.66 when the propulsive and overall statistic are considered, accordingly, at 2000 *rpm*. The latter being defined, respectively, as:

$$\eta_{prop} = \frac{T v_{\infty}}{\dot{m} g H} \quad (3.34)$$

$$\eta_0 = \eta_{prop} = \frac{T v_{\infty}}{C \omega} \quad (3.35)$$

with C representing the rotor torque and ω the angular velocity in *rad/s*. The propulsive curve, which can be taken as metrics for the nacelle operations, portrays a smooth increment up to the best performance point, then the trend shows a more rapid decay after a short plateau. Even for this statistic, the lower regimes suggest a major influence of Reynolds effects, although these are less pronounced than for the machinery performance. It is interesting to notice that at lower advancing speeds the curve for the 2000 *rpm* condition is penalised with respect to the other two. Then, the efficiency increment is sufficient to equal and then to stay stably above them. Similarly, the low and medium regimes curves are almost superimposed up to the advance ratio 1.76, from which the Reynolds effect induces a separation, with the

3. VALIDATION

slower being more affected. Analogous considerations hold for the overall efficiency. Here, the distance among the different rotor velocities is further emphasised by the twofold losses sources being gathered. A major outcome revealed by this analysis is the mutual behaviour of the two efficiency curves. In fact, the separation increases with the advance ratio, thus denoting different characteristics between the cowl and the pump performance throughout the velocity range.

To further investigate this aspect, the hydraulic and propulsive efficiencies are plotted together as functions of the advancing ratio (Fig. 3.36). The curves

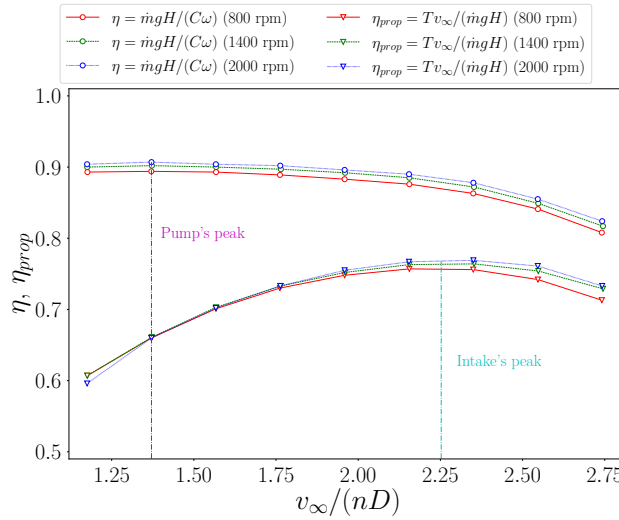


Figure 3.36: Hydraulic and propulsive efficiency as a function of the advance ratio for the three rotational regimes.

confirm a substantial difference regarding the placement of the peak value within the operating range. As a consequence, when they are multiplied to obtain the overall performance, they result to penalise one with each other. Specifically, in the present range the intake figures as the penalising component of the system. In fact, although the hydraulic efficiency drops nearby the inlet peak performance, the variation is generally within the 5%. Conversely, when the pump best efficiency point is considered, the corresponding values of the intake performance are as high as 10% lower than the optimal condition. This outcome highlights how this part of the system is crucial for the entire system operations. Revisions of the design approach and possible way to optimise it, as discussed in Chapter 4, are justifiably required.

Throughout the operating range, the shape of the capture stream tube directly affects the pump performance. At low speeds conditions (60% of the design Re_{hl}), which may be assimilated to take-off operations, the processed mass flow rate is higher than the one expected for the corresponding advance ratio (Fig. 3.37). As a consequence, from continuity, the highlight velocity re-

sults favoured over the free-stream value, thus inducing an acceleration of the flow entering the propulsor. This is recognised through the convergent shape of the streamlines from the far-field to the capture section, which performs a translation of the stagnation point away from the highlight, towards the external cowl (Fig. 3.37a). Such a flow evolution corresponds to pump operations at lower flow coefficient than the one expected by affinity laws. This results in a minor component of the meridional velocity reaching the blade. With the rotation velocity being fixed, the consequent relative component shifts towards the blade pressure side. This effect initially promotes the head rise, which sustains propulsive performance. However, the depression on the suction side expands and intensifies as the mass flow rate lowers. When this region induces cavitation on the rotor blades, as observed in the isolated case, there is a narrow range of operating conditions at higher performance than design ones. Then the statistics abruptly drop, thus causing the loss of thrust capability of the propulsor. For installed configurations, the presence of the intake is fundamental. In fact, at off-design conditions the inner throat may experience cavitation as well, resulting from the significant flow turning at the lip (Fig. 3.37b). Anyhow, despite the consistent vapour volume on the suction side, at the present flow configuration the machinery operates with a pump cavitation number $N^* = 1.53$, which is well above the thrust breakdown limit observed within the isolated case analysis ($N^* = 1.076$). This phenomenon

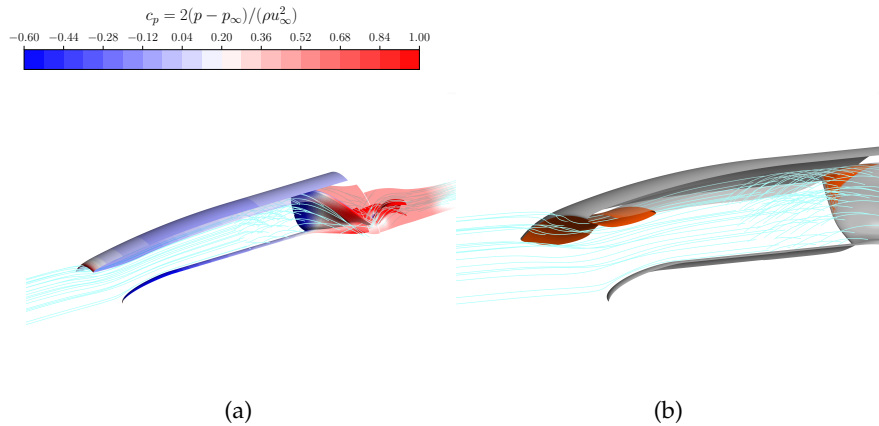


Figure 3.37: Contours of free-stream axial velocity–based pressure coefficient on the propulsor walls, superimposed with a single-channel streamlines distribution at near take-off conditions with $IVR = 1.22$ (a) and the corresponding cavitation volumes visualised through isosurfaces of vapour volume fractions, $\alpha_v = 0.3$ (b). Case with $n = 2000 \text{ rpm}$ and $Re_{hl} = 60\% Re_{hl,design}$.

further obstructs the flow passage, thus inducing additional acceleration on the entering flow and possible pump starvation. As a consequence, the detrimental effects on the impeller loading may result even more emphasised. In this regard, take-off operations represent a highly delicate condition within

3. VALIDATION

the entire envelope, since they may cause the entire mission failure.

On the other hand, a pre-diffusion configuration, as the one characterising the last simulated point of the map (140% of the design Re_{hl}), induces a divergent captured stream tube (Fig. 3.38). The resulting velocity evolution consists in a deceleration of the flow at the highlight section and consequently the stagnation point experiences a shift towards the inner walls surfaces (Fig. 3.38a). During this phase, the pump processes a higher mass flow rate than expected. This induces the incidence velocity to translate towards the suction side, thus reducing the blade loading. Therefore, cavitation may result prevented, provided the off-design is not such deep to cause pressure side cavitation. However, the reduced head rise, with the power characteristic being almost constant, generates a performance decay. While being restrained, as observed in Figure 3.36, the overall performance is substantially affected by the propulsive efficiency drop. In fact, as velocity increases beyond the intake design condition, the nacelle resistance rapidly rises. Despite the field distribution, that favours a drag deduction in the external cowl, the increment of the pre-entry streamtube contribution cannot be contained. As far as inlet cavitation, this flow configuration is such that the depression intensifies on the external walls, where vapour volumes clouds may originate (Fig. 3.38b). Although they do not affect hydraulics, an extensive evolution of the phenomenon should be avoided to prevent performance erosion.

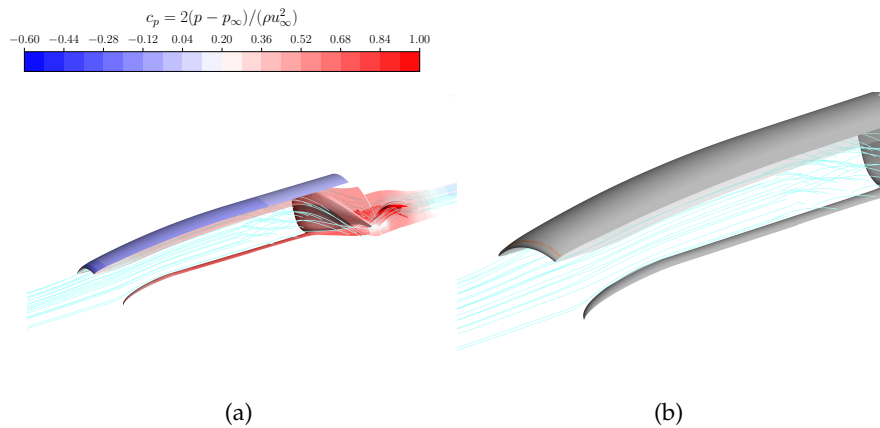


Figure 3.38: Contours of free-stream axial velocity–based pressure coefficient on the propulsor walls, superimposed with a single-channel streamlines distribution at sustained pre-diffusion conditions with $IVR = 0.69$ (a) and the corresponding cavitation volumes visualised through isosurfaces of vapour volume fractions, $\alpha_v = 0.3$ (b). Case with $n = 2000 \text{ rpm}$ and $Re_{hl} = 140\% Re_{hl,design}$.

The occurrence of cavitation substantially affects the intake design as well. In fact, this is regulated by the cavitation coefficient (Eq. 3.23), which has no dependence on the rotational regime. As a consequence, when the pump operates under similarity conditions and the intake processes an optimally

shaped stream tube, cavitation occurrence remains a degree of freedom. This is explained by considering that the coefficient numerator is constant for any flow condition, thus varying only based on the advancing velocity at the denominator. Clearly, the parameter magnitude lowers as the far-field speed increases. Conversely, inlet similarity conditions would dictate a fixed pressure coefficient distribution on the nacelle walls. Actually, this holds true unless the cavitation coefficient is so small to be in the order of the wall pressure field.

This is clearly depicted in Figure 3.39 through pressure coefficients distributions along the intake mid-plane. At low speeds conditions (Fig. 3.39a), where $IVR > 1$, free-stream conditions do not induce cavitation for the cases at 800 and 1400 rpm. As a consequence, the pressure field evolution is exactly the same. Conversely, for the faster condition the cavitation number reaches a value that is considerably within the pressure coefficient distribution in non-cavitating evolution. Thus, cavitation cloud originates in the inner cowl as graphically reported in Figure 3.37b. This phenomenon, except for inside the vapour volume, does not modify the trend of the pressure coefficient curve. However, the single-phase pressure field behaviour is delayed and the complete recovery is achieved only at the ending part of the intake. As a result, the wall integration feeds the ϕ_{pre} term, thus inducing incremental drag on the intake drag. This evidence further confirms the previously documented propulsive efficiency defect at the initial case, despite the affine stream tube shape and pump operating conditions with other simulated rotor speeds. Similar considerations hold for the high-speed case (Fig. 3.39b). However,

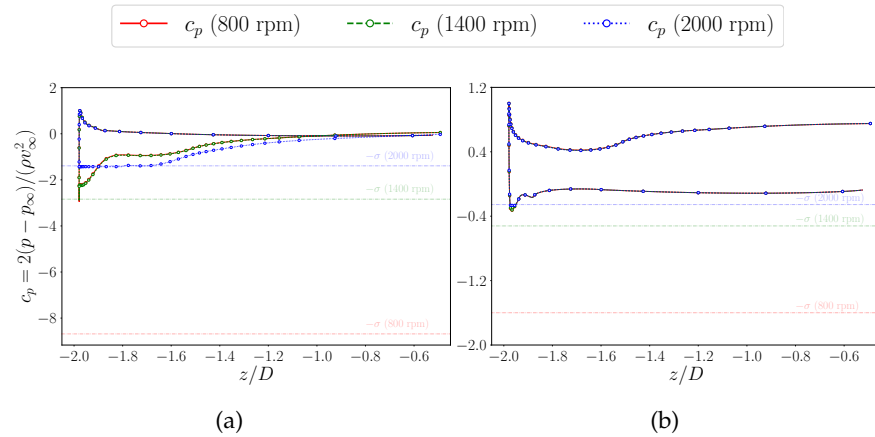


Figure 3.39: Wall pressure coefficient distributions over the external cowl mid-plane, along the axial coordinate, for the three rotor speeds. Corresponding cavitation conditions ($c_p = -\sigma$) are included for clarity. The extreme off-design conditions are reported: (a) near take-off, $IVR > 1$ and $Re_{hl} = 60\% Re_{hl,design}$, and (b) pre-diffusion, $IVR < 1$ and $Re_{hl} = 140\% Re_{hl,design}$.

3. VALIDATION

in this situation the stagnation point location (in the inner cowl) induces the lowest pressures on the outer wall surface. Again, cavitation, now of external type, occurs for the case with $n = 2000 \text{ rpm}$, even though the spatial extension is considerably constrained, as previously highlighted.

The second case on the operating map ($Re_{hl} = 70\%$ of the design Re_{hl}) is analysed more in-depth (Fig. 3.40) to explain the sudden recovery in the propulsive efficiency curve for the case at $n = 2000 \text{ rpm}$, as observed in Figure 3.35. In fact, despite the intake cavitation being not negligible (Fig. 3.40a) at these flow conditions, the extension of the vapour volume is restricted to the throat near-region. As a consequence, the pressure field distribution differs from the non-cavitating one, obtained at the lower regimes, only for the initial portion of the inlet inner surface (Fig. 3.40b). Then, at $z/D \sim -1.8$, the pressure coefficient recovers the same values. The resulting wall integration mitigates the local discrepancy, thus yielding the same propulsive performance obtained at slower rotor speeds.

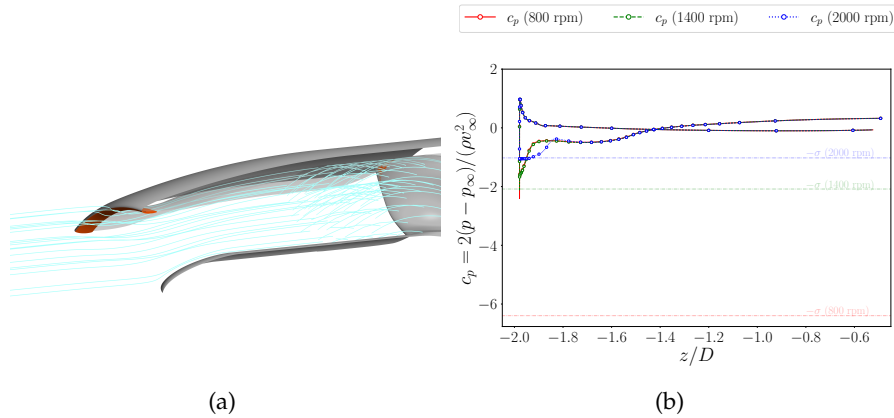


Figure 3.40: Results for the case at $IVR = 1.09$, and $Re_{hl} = 70\% Re_{hl,design}$: (a) cavitation volumes visualised through isosurfaces of vapour volume fractions, $\alpha_v = 0.3$, for the configuration with $n = 2000 \text{ rpm}$; and (b) wall pressure coefficient distributions along the external cowl mid-plane, as a function of the axial coordinate, for the three rotational regimes with cavitation conditions ($c_p = -\sigma$) included for clarity.

4 OPTIMISATION

4.1 Methods

The present section aims at introducing the main concepts recalled during the discussion of the results. A detailed theoretical treatment is beyond the purpose of the work and the reader is referred to the related bibliography for further insights.

4.1.1 Design Of Experiments

Design of Experiments (DOE) encompasses a wide list of methods tailored to efficiently extract valuable information from complex problem scenarios. These approaches are designed to collect pertinent data without investing excessive time in redundant analyses, thus emphasising a high-yield perspective. DOE methods are well-suited for various research domains, offering versatility in the pursuit of valuable insights. In particular, the term "experiments" within DOE extends beyond traditional physical tests and includes computer experiments, making it a comprehensive approach adaptable to different research contexts.

Among these methods, Latin Hypercube Sampling (LHS) stands out as a statistical technique, ensuring a systematic and evenly distributed exploration of the parameter space, contributing to a more thorough understanding of the system response to different conditions. Its advantage relies in the ability to randomly explore the design space, without including repeated or too similar evaluation points [36].

4.1.2 Evolutionary algorithms

This type of optimisation algorithms exploits the principles of the Darwinian evolutionary theory, according to which the fittest individuals survival allows for the biological evolution [95]. In nature, this process is achieved through the transfer of the optimal genes from the parents chromosomes to the offspring ones. Numerically, this concept is translated by linking each decision variable to a gene. In this way, an equivalent chromosome, characteristic of each individual, consists of a set of genes. These latter are selected based on their optimality, which is quantitatively measured with the objectives of the optimisation problem to be solved. Essentially, this quantity represents the metrics of the survival probability of each individual [68].

A set of individuals defines a generation. Thus, the process starts from an initial population, from which a new set of individuals is generated, which, in turn, sets the starting point for the next generation, and so on. The key stages

4. OPTIMISATION

during the evolution are directly borrowed from the biological nomenclature and are briefly outlined below.

Selection

Selected individuals are retained for breeding, based on their fitness. Several methods are available for the extraction of chosen chromosomes, the most popular including: proportional selection, ranking and tournament selection [68]. Specifically, the latter is implemented as follows (Fig. 4.1). In principle, all the individuals from a generation may be selected. Thus, a certain group is randomly extracted, which promotes preservation of the chromosomes diversity [14]. The winner individuals within the competitors are finally chosen among the ones characterised by the highest fitness values.

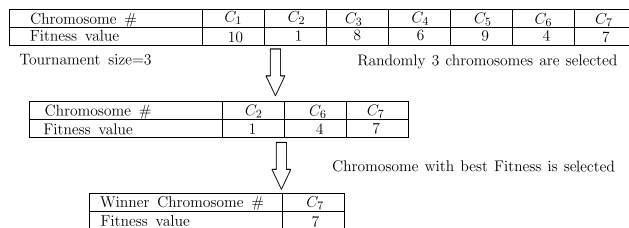


Figure 4.1: Concept of the Tournament selection, adapted from Banihashemian and Adibnia [14].

Crossover

The genes of the parents retained for breeding are recombined and mixed together in the offspring chromosome. These are chosen based on the fitness, thus promoting the inheritance of the best characters. A common implementation is the so-called Simulated Binary Crossover (SBX), which performs a representation of real values into binary notation before applying the single-point crossover. Probability density of the genes crossover is regulated through the coefficient, η_c [37]. Thus, single-point operation defines the crossover point at which the chromosomes of the two parents are split, a the corresponding halves are swapped [64].

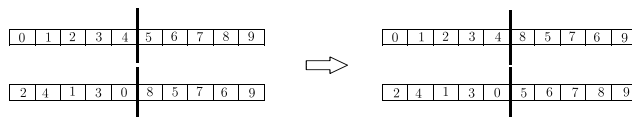


Figure 4.2: Concept of the single-point crossover, adapted from Katoch et al. [64].

Mutation

Crossover operation itself is not sufficient to explore the possible space of decision variables. If genes do not undergo mutation, optimal solutions may be locked in local optima, thus preventing the generation of fitter individuals [95]. Therefore, random mutation of genes introduces diversity among subsequent generations. One possible implementation is the Polynomial mutation, where the gene variation is applied linearly, by adopting factor that is chosen within the bounding values, according to a density distribution coefficient [121].

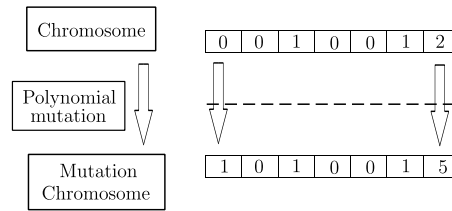


Figure 4.3: Concept of the Polynomial mutation, adapted from Tong and Du [121].

Elitism

This operation prevents the complete substitution of the parents chromosomes by offspring ones, at a given generation. Preserving part of the parents characteristic unchanged, by selecting them based on the fitness values, allows for transferring the optimal genes, without damaging them through the crossover process. Thus, retained candidates can be newly selected as parents [95].

Among the several GA implementations available, the NSGA-II represents a common choice in CFD optimisation of aerodynamic applications [110].

4.2 Intake optimisation

Parametric model

The focus of the following analysis is to maximise the propulsive performance through the minimisation of the intake resistance. The motivation behind this choice is twofold. In fact, according to Equation 3.22, in the present model the net thrust is regulated by the inlet drag and the momentum imbalance across the pump sections. Therefore, while considering the machinery operations unchanged, the only driver to increase the efficiency is the reduction of the nacelle axial resistant force. As for the assumption of known pump characteristic curve, Section 3.4 already clarified that within a certain operating range, the installed hydraulic performance are the same as the isolated ones. Therefore, a multi-fidelity approach is employed, with the optimisation conducted on the

4. OPTIMISATION

2D axi-symmetric model. The assessment of improvements is then verified using the integrated intake-pump configuration.

To efficiently control the nacelle shape, the corresponding geometry is piecewise-defined and parameterised. Specifically, B-splines are adopted to reconstruct the external cowl and the aft inner walls. The latter encompassing the outline from the intake throat to the pump interface. Conversely, for the fore inner curve that completes the geometry the original quarter-ellipse equation [71] is retained and altered. Three points are directly manipulated during the whole optimisation process, respectively: the axial (x_{hl}) and the radial (r_{hl}) coordinates of the highlight location, and the throat section area through the extension of the corresponding radius, r_{th} (Fig. 4.4). These parameters directly affect the way the sucked stream tube is directed towards the pump. As a consequence, they result as primary drivers in the research of an optimal flow distribution, which is able to improve the propulsive performance. This fact explains why these geometrical features are a common choice as decision variables for aeronautical nacelles optimisation studies [83, 82]. With the downstream control points being fixed, no variations of the maximum diameter and related thickness are included. To keep the smooth trend of the profile, the B-spline interior control points are linearly scaled, based on the terminal fixed coordinates and the modified initial point location. This applies for both the axial and radial positions in the case of the external cowl, while only the vertical locations are re-computed for the inner curve. As far as the fore inner wall, the coefficients are determined by inverting the quarter ellipse equation based on the modified coordinates of the extreme points. This ensures the

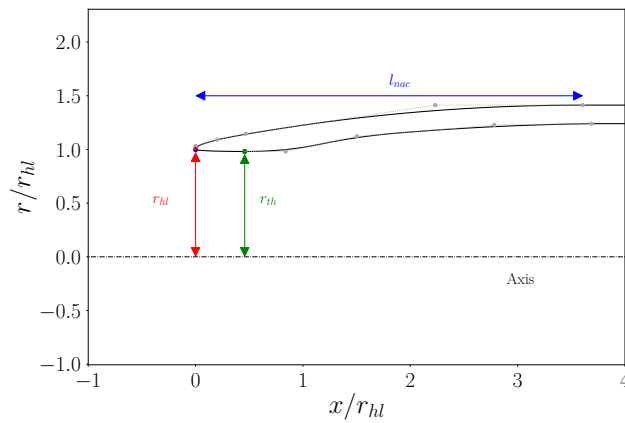


Figure 4.4: Outline of the baseline intake geometry, with addition of the manipulated coordinates and the B-splines' control polygons.

original null tangency at the throat section is maintained across the various individuals. It is not worthless to be mentioned that, to preserve the diffusive behaviour of the shape and its ability to ingest the flow without inducing consistent lip separations, the throat radius is restrained to lay always be-

low the highlight location. To guarantee this constraint, the vertical variation is provided as a negative distance, relative to the lip radius. Following this approach, the main nacelle characteristics being modified are: the external axial extension, l_{nac} , the capture area and the throat area or, equivalently, the Contraction Ratio (CR). The latter being defined as ratio between the throat and the highlight areas, as $CR = A_{th}/A_{hl}$. Within this study, no influence of the inner walls axial length is considered. The maximum extensions of the exploration ranges is reported in Table 4.1.

Table 4.1: Ranges of the modified geometrical parameters, with respect to the baseline.

	Minimum	Maximum
r_{hl}	-16%	+16%
l_{nac}	-7%	+7%
r_{th}	-17%	+19%
(CR)	(-24%)	(+4%)

Solution strategy

Optimisation algorithms are managed by Python scripts. The latter are responsible for all the tasks required for the generation of the individuals' necessary statistics. The steps include:

- nacelle curves manipulation;
- writing of the geometry file in a mesher-readable format;
- invoking the CFD solver (Ansys Fluent) for case computation and performance extrapolation;
- storing the propulsive metrics;
- selection of the next individual parameters according to the optimisation method.

The process for creating the intake 2D planar grid described in Section 3.4 is scripted and executed for all the geometry variants considered. As a consequence, the grid sizing and elements distributions are kept unchanged. The only minor differences being the cells quality at local level, where the baseline manipulation occurs. As far as the boundary conditions and computational strategy, the same approach as described in Section 3.2 is applied. Thus, SST turbulence model is employed for in-design flow investigations. In addition, to account for feasible solutions, the geometries with cavitation susceptibility are discarded. Although the two-phase modelling is not included in the individuals' CFD evaluations, the selection relies on the pressure distribution along the intake walls. Specifically, the cases recovering minimum values, lower than the saturation pressure are not retained for statistic post-processing.

4. OPTIMISATION

The optimisation is cast as a two-objective constrained problem, which aims at reducing the drag coefficient (see Eq. 3.21) while maximising the Pressure Recovery, the latter being defined as the ratio between the PIP and the free-stream total pressure:

$$PR = \frac{p_{PIP}^0}{p_\infty^0} \quad (4.1)$$

It should be noted that to satisfy the requirements of the GA, which is implemented to solve a minimisation problem, the second objective function is re-formulated in terms of a pressure coefficient as:

$$1 - PR \quad (4.2)$$

4.2.1 Latin Hypercube Sampling

Sampling setup

An initial design space exploration is conducted by analysing the statistics of a set of geometry variants, distinguished following a LHS distribution. In this process, 150 individuals are generated. Specifically, a LHS matrix with three columns and as many rows as the geometrical variants is produced. Thus, each row contains a triplet of decision variables that uniquely identifies one of the individuals. Then, to enforce the dimensional variations as of Table 4.1, the matrix arrays are further manipulated. In particular, the first two columns, representing the axial and radial coordinates of the highlight, are re-ranged from -1 to 1 , while the third column is multiplied by -1 to include only negative values, representing the difference between the throat and the lip radius. The prescribed variable-specific Δ is then multiplied columnwise, according to the chosen ranges. In this way, the triplet are read at each simulation step by the script, which is then responsible for the definition of the B-splines describing the intake shape. Thus, the algorithm can proceed with the mesh generation, before CFD computation results are returned for post-processing.

Results

In Figure 4.5 the sensitivities of both the nacelle drag and pressure recovery are reported as a function of the decision variables. The two statistics indicate a clear monotonically increasing trend as a function of the highlight radius (Figs. 4.5a and 4.5d), suggesting a mutual conflict in the search for an optimal solution. The corresponding R -values prove almost the same linear correlation, despite the deviation is one order higher for the pressure recovery. This aspect is motivated by the significant dispersion of the scatter in a majority of the interval, even though the scatter denotes a slight clustering towards the right end. It is important to mention that by assuming the flow conditions fixed, while modifying the highlight radius, induces a variability of the captured

stream tube shape, which is included through the IVR colorbar. Even in this regard, the two objectives denote opposite behaviours, where near-cylindrical flow configurations favours drag reduction, while significant pre-diffusion can improve the pressure recovery. Concerning the intake length, reducing the extension of the nacelle allows for decreasing the overall wetted surface, thus acting in favour of lower resistance (Fig. 4.5b). On the other side, the PR looks almost insensitive to such a variable, with a barely null correlation (Fig. 4.5e). Although the scatter plots depict a consistent dispersion, the general behaviours allow for an important consideration. In fact, moving towards shorter solutions appear as an efficient driver for the optimisation, since drag reduction can be pursued without any significant impact on the pressure recovery. As for the contraction ratio, the considerations hold similar to those drawn for the highlight radius sensitivity (Figs. 4.5c and 4.5f). In

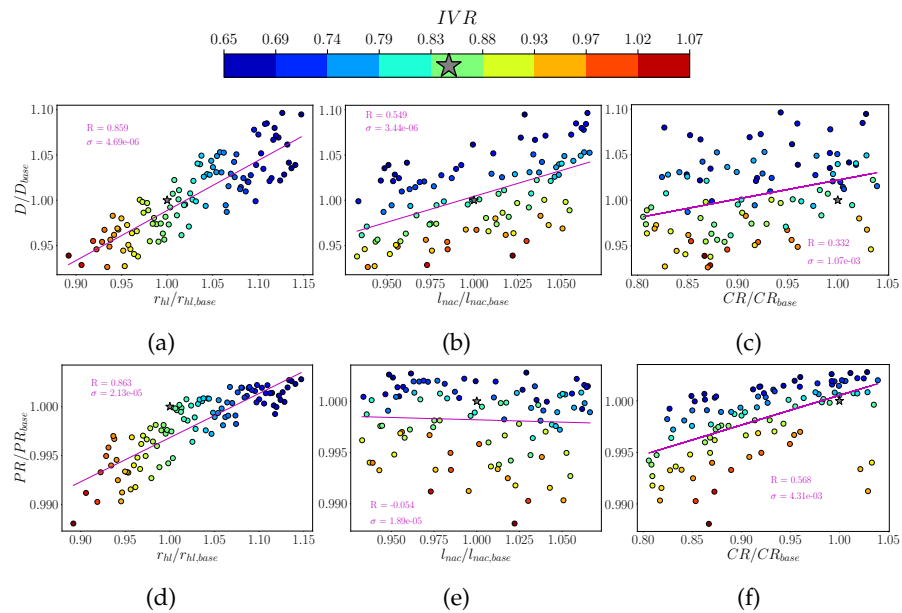


Figure 4.5: Nacelle drag (a-c) and pressure recovery (d-f) sensitivity to the decision variables, respectively: highlight radius (a-d), intake length (b-e) and throat radius (c-f). The R -values and deviation for the corresponding linear regressions are printed.

fact, the two objects denote clear conflicting trends, even though the effect of the modified IVR is in this case less defined. It should be noted that the pressure recovery exhibits a reduction of the database dispersion towards the right limit of the considered range, except for the presence of three outliers. This evidence suggests that a stabilisation in the direction of a maximum improvement achievable at high contraction ratios. With little room left for increasing this parameter, it follows that optimal solutions should not be endeavoured far from the baseline value, especially if at lower CR . In general,

4. OPTIMISATION

the results indicate that drag performance can be improved up to 5%, if part of the solutions are excluded based on the IVR . Conversely, the PR best increments do not exceed 1%.

From these considerations, a Pareto front is expected to generate on the objective functions domain (Fig. 4.6). Low-resistance curves require in gen-

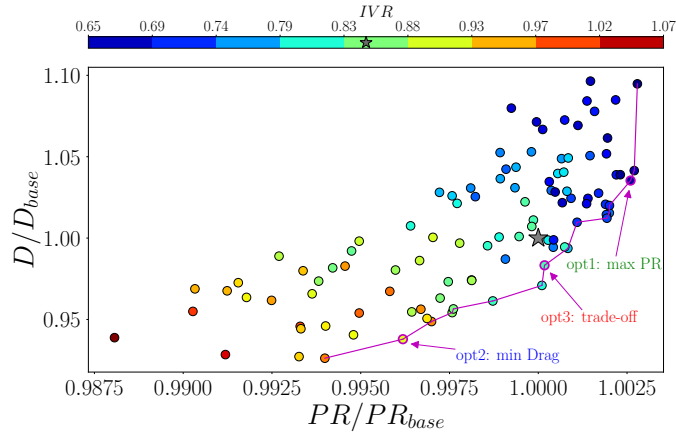


Figure 4.6: Objective functions space, depicting nacelle drag versus the pressure recovery. The Pareto front from the DOE analysis is tracked and three dominant solutions are selected.

eral a high- IVR flow configuration, even though the baseline performance can be slightly outreached even without drastic variations on the captured stream tube. On the other hand, to obtain minimal pressure recovery rise it is necessary to account for consistently increased pre-diffusion. Further flow field investigations are performed by selecting three distinct individuals on the Pareto front. To this end, two solutions are identified that exhibit IVR values not significantly distant from the design. These include: one in favour of maximum PR (named $opt1$) and one with consistent drag minimisation ($opt2$). In particular, the latter reduces the resistance by 6%, while the best pressure recovery improvement from $opt2$ is limited to 0.26%. Then, a third trade-off case ($opt3$) is retained. The latter allows for satisfying both the objectives, with -2% in drag and +0.02% in PR , while preserving a feasible IVR value.

A comparison between the optimised geometries and the baseline is drawn in Figure 4.7. Following the previous discussion on the decision variables sensitivity, the three individuals all show a shorter intake length. Specifically, $opt1$ geometry depicts a significantly augmented capture section, with a contraction ratio that is only about 1% lower than the baseline. Thus, the expansion is only partially affected. However, if the relative variation between the highlight and throat areas is minimal, the same consideration is not applicable to the reciprocal variation between the throat and the pump interface section. In fact, while the latter experiences no manipulation, the former results significantly aug-

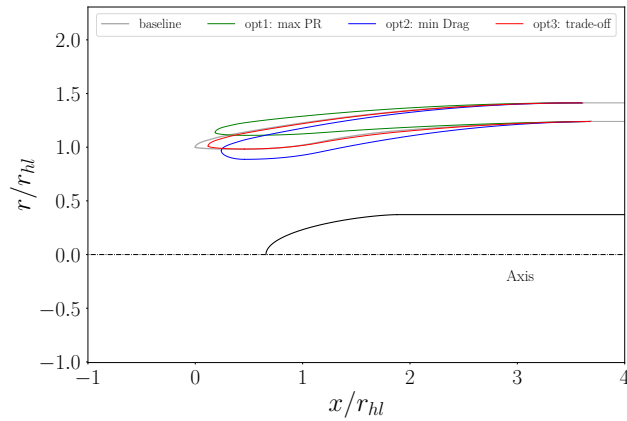


Figure 4.7: Comparison between the baseline geometry and the chosen optimised solutions from the Pareto front (Fig. 4.6).

mented. As a consequence, the diffusion occurring in the inner region of the intake is markedly reduced, which favours the decrease in the pressure losses. The solution providing minimum drag displays instead a completely different shape. The highlight is shifted downward, thus reducing the capture area by 6%. The evident increased bluntness of the lip, due to a CR reduction by 13%, suggests greater expansion and, consequently, major effect through the diffusion process. In this case, the motivations for the solution optimality should be endeavoured in the TDB. In fact, as the intake shape favours cylindrical captured stream tube, the ϕ_{pre} component becomes negligible and so does the external nacelle contribution. On the other hand, a sustained pre-diffusion tends to feed the pre-entry drag up to a condition that neither a negative ϕ_{nac} can mitigate the resistance. Interestingly, the trade-off solution appears as a shorter version of the baseline, with only a 2% increment in the highlight area and a 2% reduction in the contraction ratio, which proves the reference geometry an efficient starting point within the present flow conditions and decision variable ranges.

The flow field distribution (Fig. 4.8) is analysed to draw a visual comparison among the optimised solutions and the baseline (Fig. 4.8a). The slim lip geometry of solution *opt1* (Fig. 4.8b) almost suppresses the flow acceleration at the throat location. This is a consequence of the increased pre-diffusion induced by the augmented highlight area. As the IVR reduces to 0.66 from the design value, 0.84, the stagnation point shifts towards the inner walls surface. As a consequence, the depression transitions at the external cowl, where the pressure distribution indicates visibly lower field values. The reduced diffusion allows for a smoother recovery, which results in a higher pressure distribution at the pump interface. The solution minimising the drag, here named *opt2* (Fig. 4.8c), portrays a completely opposite situation. The blunt nose induces a high flow acceleration that is hardly recovered at the

4. OPTIMISATION

impeller upstream, from which the inferior recovery capability is justified. On the external surface the pressure has essentially the same distribution as in the baseline flow field, except for an enhanced depression on the rear region. The trade-off between the two (Fig. 4.8d) provides no significant difference with the starting geometry. A minor region towards the backward section of the external cowl displays lower pressure values, which suggests that despite increased highlight radius, the length reduction locally generates slightly strong wall gradients.

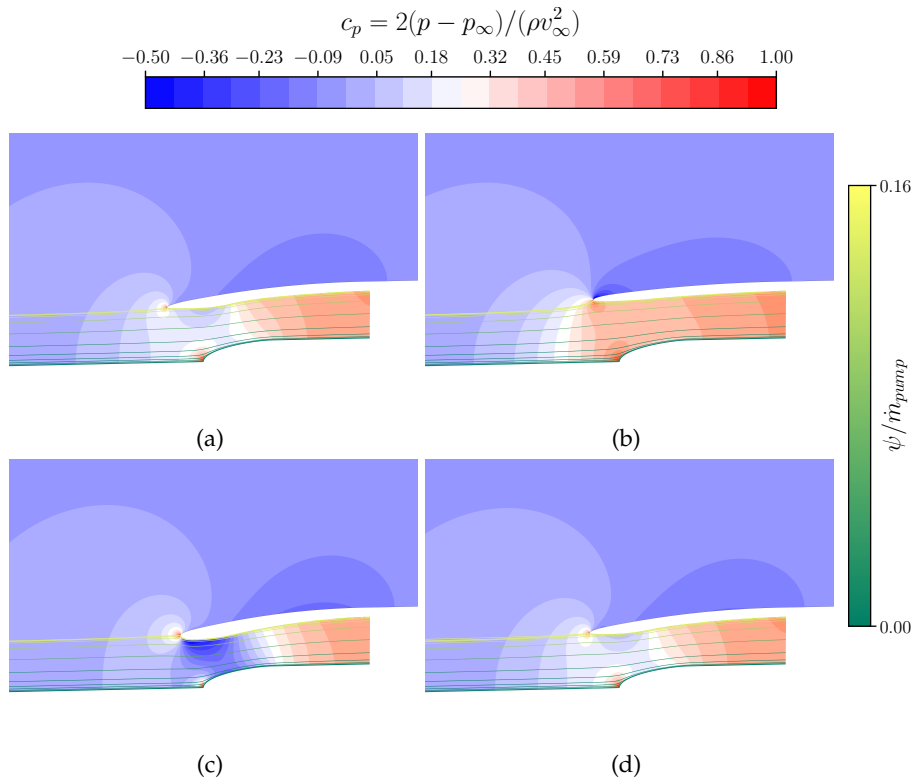


Figure 4.8: Contours of pressure coefficient, c_p , superimposed with streamlines coloured by stream function, ψ , normalised with the pump mass flow rate. Baseline solution (a) is compared with three optimised individuals: (b) maximum pressure recovery, *opt1*, (c) minimum drag, *opt2*, and (d) a trade-off between the two, *opt3*. The corresponding *IVR* are: 0.85, 0.66, 0.91 and 0.83.

4.2.2 Genetic Algorithm

Evolutionary setup

Conflicts between the chosen objectives, as proved in the previous discussion, justify the adoption of a GA for the research of optimal individuals. A NSGA-II implementation is selected from the Python Multi-Objective Optimisation

(PyMOO) open source library. The optimal individuals triplets identified in the Pareto front of the DOE are retained as the initial population. Thus, this set of starting parents are let propagate for 30 generations, each consisting of 15 individuals. Crossover among the parents characteristics is regulated using SBX with a probability set to 0.9. Mutations of geometrical parameters inherited from the parents are introduced following a polynomial strategy, with a distribution index, $\eta_c = 20$ [37]. Shape constraints are set as reported in Table 4.1.

Results

The objectives function domain is plotted in Figure 4.9 . The dispersion of

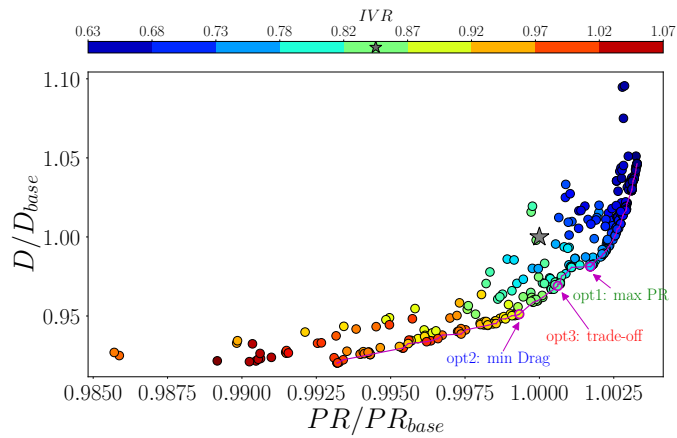


Figure 4.9: Objective functions space, depicting nacelle drag versus the pressure recovery. The Pareto front from the GA analysis is tracked and three dominant solutions are selected.

the individuals allows for a clear identification of the Pareto front, which further confirms the conflicting response of the two statistics. The minimal improvements achievable on the pressure recovery enforces the curve to flatten asymptotically towards the right end of the plot, which then acts as a physical limit for the system. The solutions clustering around this region feature significant reduction of the cruise IVR , thus resulting in augmented drag. Conversely, the front follows a much smoother trend in the sense of resistance deduction. In fact, up to baseline values the curve portrays a monotonic behaviour with an average reduced slope. This in general encompasses solutions with a wider range of admitted capture ratios. In is worth noting that in the region where trade-off solutions lay, the increasing outline of the minimum drag branch transitions to a short plateaux before the ramp-up segment promoting PR maximisation. This small sector denotes an optimiser defect in keeping the resistance minimisation trend while increasing the pump inlet pressure. Notably, these individuals meet the two-objectives optimisa-

4. OPTIMISATION

tion with feasible values IVR . In this case, the variety of admissible cruise solutions is more populated. The latter intended as the ones characterised by optimised performance without a stream tube shape that may compromise off-design conditions. Consequently, the selection of three improved individuals is possible even within suitable IVR values, ranging from 0.78 to 0.91. Due to the more pronounced tendency of the drag objective to be optimised, the chosen maximum PR configuration, $opt1$, results, in fact, as a lower resistance geometry, with c_d reduced by $\sim 2\%$. However, the trade-off solution, $opt3$, loses only 0.1% benefit in pump pressure if compared with the previous, while improving the drag by $\sim 1.2\%$, thus leading to more than 3% increment in the propulsive efficiency. If a 0.07% deterioration in the PR is accepted, a minimum drag solution ($opt2$) can be selected to provide a resistance reduction of 4.9%, while keeping the $IVR = 0.91$, i.e. 0.06 higher than the baseline.

To provide an increased pressure recovery without including an excessive pre-diffusion, the algorithm performs towards the suppression of the throat section, therefore minimising the diffusion through the internal ducting (Fig. 4.10). Thus, preserving the IVR induces a contraction ratio almost equal

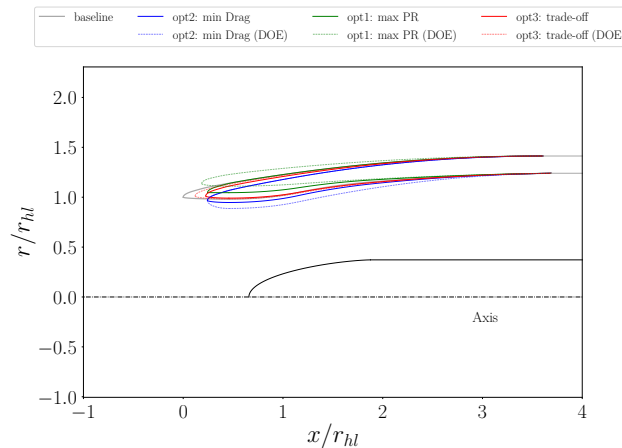


Figure 4.10: Comparison between the baseline geometry and the chosen optimised solutions from the Pareto front (Fig. 4.9).

to 1 and, consequently, a strong sharpness of the lip outline, which may be critical for off-design conditions. Notably, solution $opt2$ recovers the same shape of the external surface as the DOE counterpart and so does with the capture stream tube. Conversely, the inner surface is considerably manipulated, by restoring the flat shape at the throat section typical of the baseline. In addition, the contraction ratio is markedly augmented, from -13% obtained with the analogous DOE individual to the present -0.5%. As a consequence, the strength of the diffusion process results significantly reduced. As far as the trade-off solution, the latter denotes only minimal modifications with respect to the previous DOE solution. The most evident being the length re-

duction. Precisely, the highlight radius is only partially mutated from the DOE counterpart, while the throat width modification provides a CR reduction of 1.1% from the baseline. This result further confirms the optimal design of the inner ducting, despite no definite conclusions can be drawn since local manipulation is not performed at finer level than the linear scaling of the control points. In general, all these three geometries collapse to shorter shapes, flattening towards the lower constraint of the nacelle extension. This observation suggests that further analysis should be conducted by loosing such bound and, consequently, letting the axial location of the plug being adjusted to include the benefits of different mutual placements.

Propulsive performance is further analysis by comparing the walls pressure distributions on the optimised solutions obtained from the two approaches (Fig. 4.11). The maximum PR solution from the GA allows for a substantial reduction of the pressure undershoot on the external cowl, near the lip (Fig. 4.11a). This evidence results from the substantial reduction of the pre-diffusion, which induces lower flow turnings upon stagnation and, consequently, lower depression intensity. While this behaviour affects mainly the initial region, the remainder recovers essentially the same field as both the LH counterpart and the baseline. As far as the internal duct, the straight shape of the LH solution ensures an almost flat trend of the pressure coefficient. The addition of a lower throat radius induces augmented acceleration of the captured stream tube. As a consequence, the diffusion process depicts a stronger local gradient that explains the poorer recovery capability at the pump interface. This flow evolution impacts on the entire internal duct. As a result, the increment in the total pressure introduces higher pressure components on the plug, thus resulting in raised coefficient curves (Fig. 4.11b). Thus, the walls integration favours the drag reduction of the GA variant over the other two. Figure 4.11c suggests that to reduce the propulsor resistance, the main strategy to follow is to drastically reduce the internal pressure distribution, which again contrasts with the optimisation of the other objective. Specifically, if the external contribution is neglected since is almost equivalent among the three geometries, the inner ducting portrays completely inverted trend as previously observed. The highlight radius reduction generates a captured flow acceleration that results in lower wall pressure loads than in the external surface. This effect is evidently emphasised by the small contraction ratio of the LH solution, characterised by a significant bluntness. Additionally, the internal pressure reduction induces smaller pressure distributions on the spinner (Fig. 4.11d). The strong diffusion occurring on the region downstream of the throat is markedly depicted through the slope of the c_p curves, on both the nacelle and the centerbody surfaces. This effect results in a penalised pressure recovery at the pump inlet. A trade-off solution figures in general as a shorter variant of the baseline. In fact, the pressure distribution on the internal channel is essentially the same, though spread over a smaller wetted surface

4. OPTIMISATION

(Fig. 4.11e) . This fact is further confirmed from the coefficient trend of the plug wall (Fig. 4.11f) . Similar considerations hold for the external surface, where

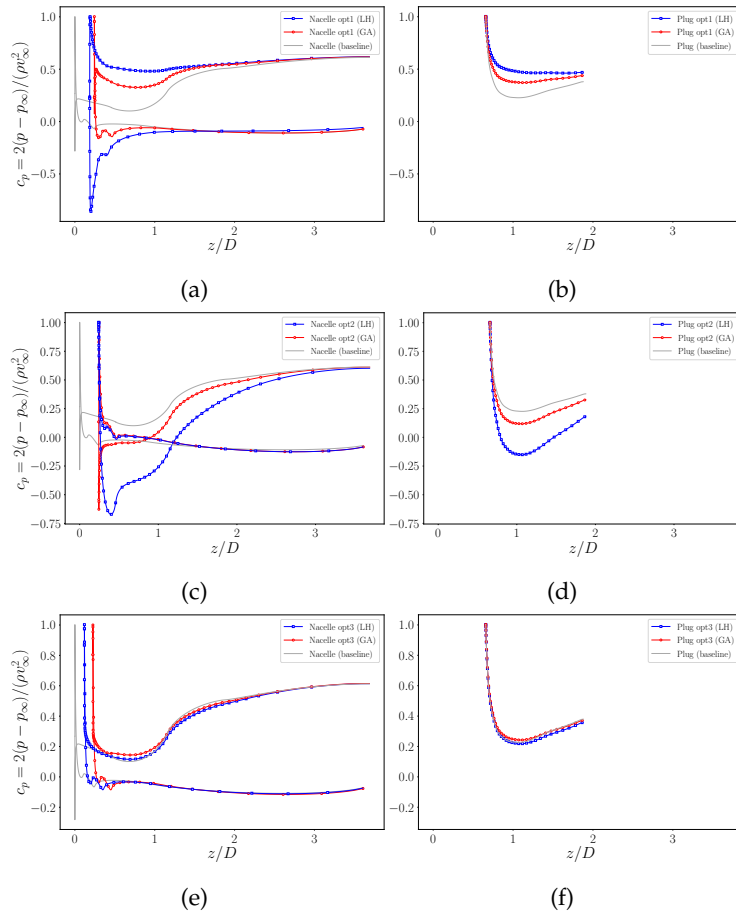


Figure 4.11: Pressure coefficients distributions on the intake walls, comparing between the optimal solutions from LH and GA, with baseline as a reference. Nacelle (a-c-e) and spinner (b-d-f) data are reported for the solutions labelled as: maximum pressure recovery, *opt1* (a-b), minimum drag, *opt2* (c-d), and trade-off performance, *opt3* (e-f).

minimal local modifications of the undershoots intensities can be identified. In this regard, the augmented performance of the GA solution should be primarily ascribed to the nacelle length, and partially to pressure distribution on the near-throat region, which promotes the thrust integral, thus reducing the ϕ_{pre} term.

4.3 Installed model outcomes

4.3.1 Results

To assess the operations at off-design conditions, the optimised solutions analysed in the GA section are retained and tested in installed configuration. To this end, the corresponding 2D-axisymmetric geometries are revolved by 60° and the 3D periodically reduced integrated model is defined following the computational principles outlined in Section 3.4 for the baseline shape.

The chosen geometrical manipulation strategy focuses on the fore portion of the intake, thus letting essentially unaltered the inner ducting in the proximity of the pump interface. As a result, the hydraulic performance depicts no significant sensitivity to the inlet geometry over almost the entire set of operational regimes (Fig. 4.12).

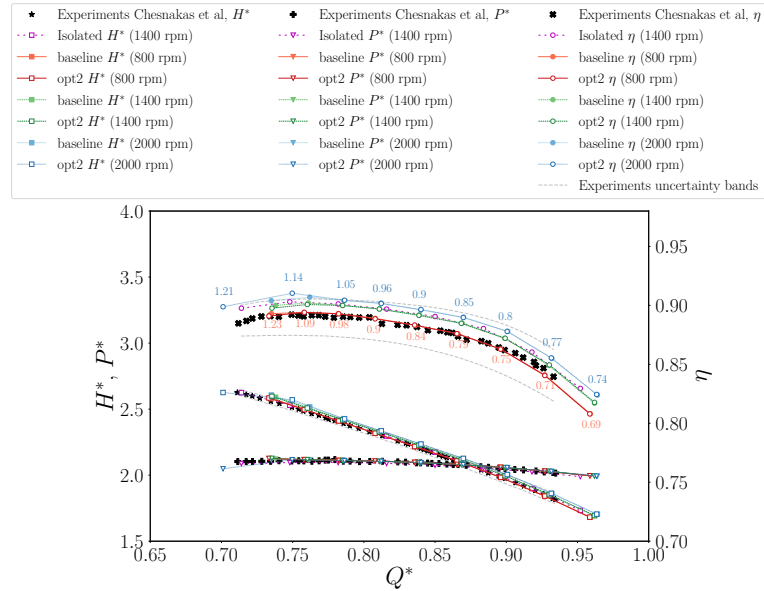


Figure 4.12: Head coefficient H^* , power coefficient P^* , and hydraulic efficiency as functions of flow coefficient Q^* . The CFD results, obtained at three different rotor speeds for both the baseline and *opt2* geometries, are compared with experimental data [28] and previous numerical solution from isolated model. *IVR* values are added as data tips: baseline beneath and optimal solution atop.

However, the pump characteristics at low-speed conditions ($Re_{hl} = 60\% Re_{hl,design}$) deserve some additional inspections. In fact, with the stagnation point located in the external cowl, the flow turning at the lip increases thus inducing a low pressure core in the internal fore region. The circulation occurring within causes an obstruction of the ingested mass flow rate, resulting in

4. OPTIMISATION

lower flow coefficients in the configurations with higher design IVR (Fig. 4.13). However, the stream tube capture ratio is not sufficient to determine the pump operations. In fact, the shape of the inner walls may promote the boundary layer thickness, thus inducing augmented obstructions despite the value of IVR . This is the case of the *opt1* geometry ($IVR = 1.12$) reported in Figure 4.13b. Anyhow, although depicting the wider circulation bubble among the other shapes, the highlight opening is sufficient to mitigate the blockage effect, then resulting in ingested mass flow rates, stably higher than the baseline (Fig. 4.13a), despite the 11% defect in the capture ratio. Furthermore, the minimum drag solution portrays a smaller circulation region than the previous geometries (Fig. 4.13c), even at high $IVR = 1.31$. Nevertheless the depression intensity outreaches any other individual, especially *opt3*, which recovers the best stream tube configuration for the low-speeds conditions (Fig. 4.13d). The obstruction effect depicts a non-linear trend, en-

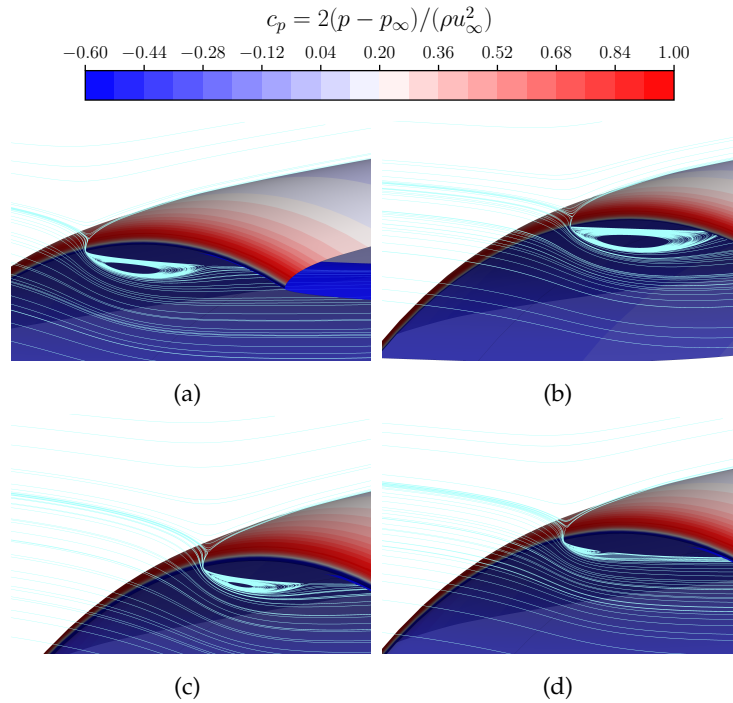


Figure 4.13: Contours of free-stream axial velocity–based pressure coefficient on the propulsor walls, superimposed with a single-channel streamlines distribution at $Re_{hl} = 60\% Re_{hl,design}$ and $n = 800 \text{ rpm}$. Magnification of the circulation region near the lip for the baseline (a), *opt1* (b), *opt2* (c) and *opt3* (d) geometries. Corresponding IVR values are: 1.23, 1.12, 1.31 and 1.20.

hancing as the rotor velocity, especially as a consequence of the cavitation volumes development as observed in Figure 4.12. The implications are extremely emphasised with the *opt2* solution, where the two lower operating

points of the curve at 2000 *rpm* denote a significant reduction of the mass flow rate processed by the pump. This induces lesser velocities at the highlight section, with a consequent reduction of the *IVR* by up to $\sim 10\%$ if compared with the corresponding conditions at 800 *rpm*. Conversely, as the far-field velocity increases the optimality of the stagnation point location mitigates this flow evolution, thus allowing the pump to operate at the same conditions irrespective of the upstream inlet geometry.

Considering propulsive performance, the improvements are only marginal and in general lower than predicted by the 2D axi-symmetric model. In particular, at the lower regimes, no significant two-phase phenomena affect the system operations and the propulsor maps depict restrained discrepancies until the free-stream cavitation number starts to play a role (Fig. 4.14). The

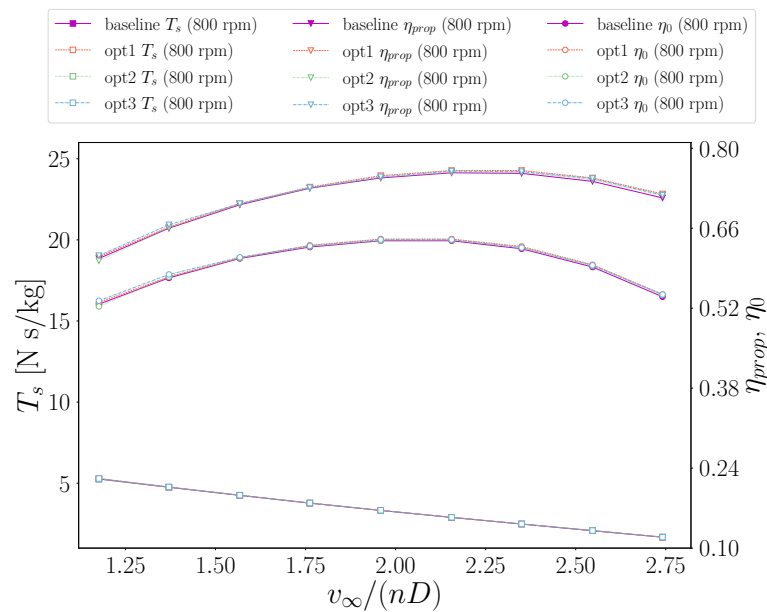


Figure 4.14: Specific thrust T_s , propulsive efficiency η_{prop} , and overall efficiency η_0 as functions of normalised advancing velocity. The baseline performance is compared with the one obtained from the three optimal individuals, at a rotor speed of 800 *rpm*.

main advantages of the optimisation procedure are evident at low-speeds conditions, where the intake trade-off shape provides improved propulsive efficiency by $\sim 0.5\%$ over the baseline. Conversely, *opt2* geometry denotes a performance degradation. In fact, the combination of hydraulic and propulsive statistics induces a lowering of 0.4% with respect to the starting outline that increases to 1% if *opt3* is considered. Near the design conditions, the efficiency peaks are more bounded, ranging from 0.756 to 0.761 , which reduce to $0.638 \div 0.641$ if the overall quantity is considered. In any case, the baseline operates with lower performance. At high-speeds operations, the

4. OPTIMISATION

maps result improved by all the optimised solutions. In terms of propulsive efficiency, solution *opt2* outperforms by 0.7%, compared to the +0.5% of the trade-off geometry. However, this slight superiority is mitigated by the pump performance, thus leading the two shapes to the same overall performance of 0.544. Despite the restrained improvements, geometry *opt3* results in more efficient operations over the entire envelope. Although the obstruction effects developing at the highlight at higher rotor regimes, significant detrimental effects appear only when inlet flow acceleration induces cavitation occurrence. As a consequence, the lowest far-field velocities considered for operations at 1400 rpm, as observed in Section 3.4, have no remarkable outcomes on the propulsor maps.

Irrespective of the installation, the pump operates at similar conditions (Fig. 4.15), thus resulting in the same non-dimensional hydraulic curves as in the cases at 800 rpm. The system can tolerate over 7% difference in the *IVR*, as in the case of *opt1* (Fig. 4.15a) and *opt3* (Fig. 4.15b) geometries, without considerable impacts on the pumping device. In fact, despite the major

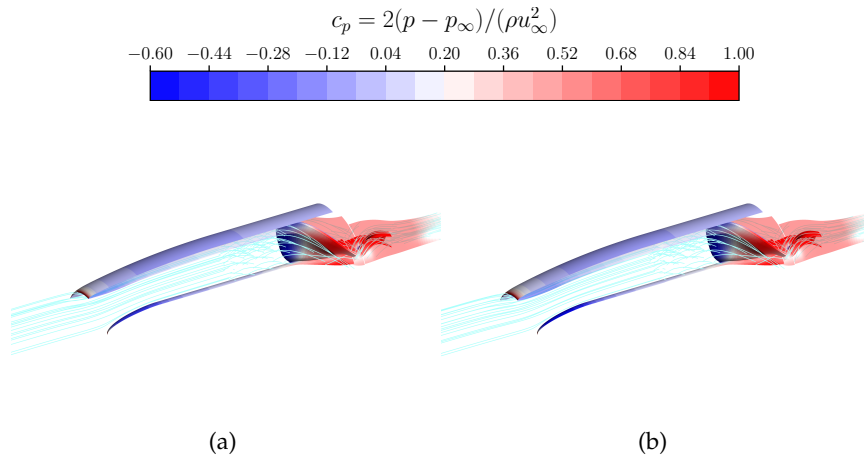


Figure 4.15: Contours of free-stream axial velocity–based pressure coefficient on the propulsor walls, superimposed with a single-channel streamlines distribution at $Re_{hl} = 60\% Re_{hl,design}$ and $n = 1400 \text{ rpm}$, for the *opt1* (a) and *opt3* (b) geometries. Corresponding *IVR* values are: 1.13 and 1.20.

extension on the internal low pressure region near the throat of the trade-off solution, the c_p over the blade is essentially the same. Inner and outer pressure field discrepancies are only effective in terms of propulsive performance. However, when considering non-dimensional quantities, these follow the discussion for the operations at the lower regimes, depicted in Figure 4.14. Specifically, except for the Reynolds effect, which tends to penalise low rotor speeds conditions, the trends of the performance curves and the relations among the different geometries remain valid.

The shape of the capture stream tube throughout the operating points can

be quantitatively analysed through the behaviour of the IVR as a function of the normalised far-field velocity (Fig. 4.16). The curves in general follow the

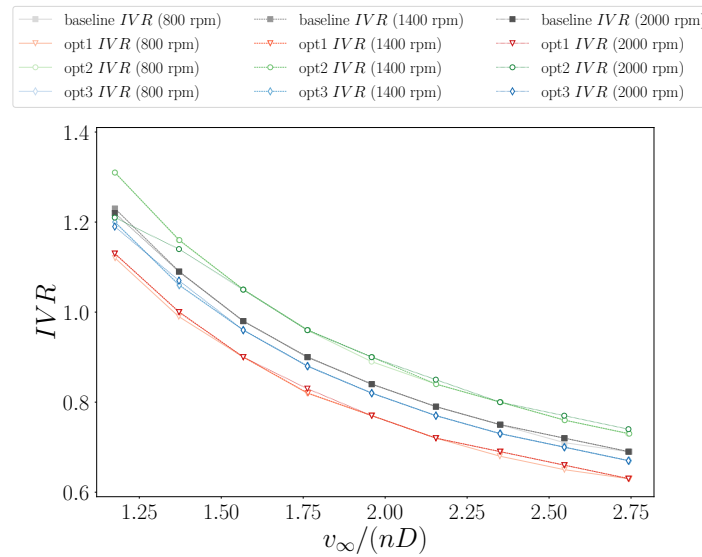


Figure 4.16: IVR as a function of normalised advancing velocity, comparing the three optimised solutions and the baseline at the three rotor rotational regimes.

same monotonic decreasing trend, collapsing on single lines depending on the intake geometry. These portray a separation from the baseline reference, which remain nearly constant over the whole range of advancing velocities. This evidence denotes a tendency of the system to operate always under similarity conditions, unless non-linear flow phenomena alter the general evolution. When these occur, the related effects are observable in the curve of the *opt2* configuration operating at 2000 *rpm*. As anticipated, when cavitation occurs in the inner ducting, thus obstructing the ingested flow, the resulting highlight velocity can be such affected to cause affinity breakdown on the processed stream tube. Conversely, vapour volumes developing on the external walls, a situation typical of high velocity conditions, induce no alterations on the capture stream, thus letting the hydraulic performance unaffected. However, either internal and external cavitation drastically impact on the propulsive statistics. This aspect results evident when propulsor maps at 2000 *rpm* are investigated (Fig. 4.17). Low Re_{hl} operations are drastically prejudiced when extended cavitation volumes develop at the inlet, which is the case of the initial operating points on the high design IVR *opt2* geometry. Here, the performance sudden drop is mainly caused by the intake pressure field distribution. In fact, while the pump experiences markedly different operating points, the blades' vapour volumes are not enough to overcome thrust breakdown limit, the corresponding cavitation coefficient being $N^* = 1.219$. On

4. OPTIMISATION

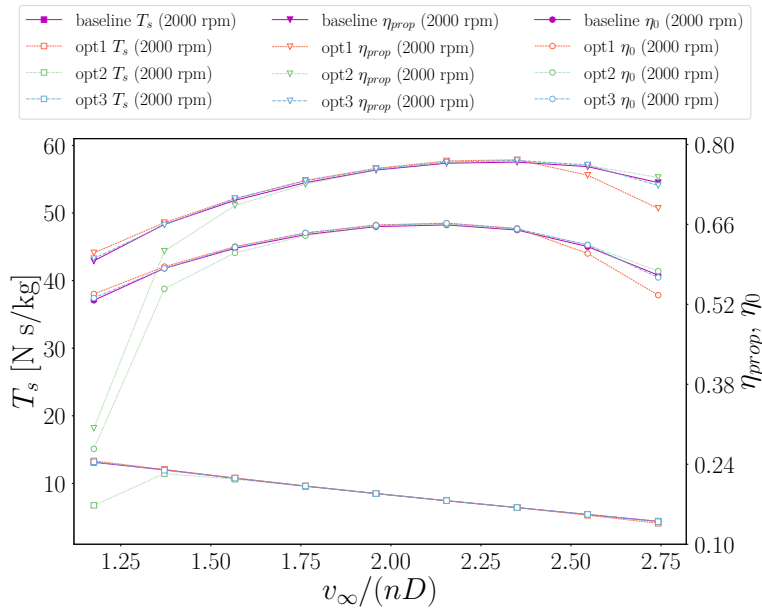


Figure 4.17: Specific thrust T_s , propulsive efficiency η_{prop} , and overall efficiency η_0 as functions of normalised advancing velocity. The baseline performance is compared with the one obtained from the three optimal individuals, at a rotor speed of 2000 *rpm*.

the contrary, wall pressure integration massively feeds the ϕ_{pre} component, which suddenly erodes the efficiency by up to 49%, thus confirming a highly non-linear response. At the same flow conditions, the maximum pressure geometry exhibits the exact opposite behaviour. At reduced *IVR*, internal cavitation is delayed, thus sustaining propulsive performance up to 1% over the trade-off solution. Anyhow, this improvement comes at the expense of high speed operations. Here, in fact, the behaviour of *opt1* and *opt2* is inverted, even though the efficiency drop of the former is considerably less pronounced than the one of the latter at low Re_{hl} . In general, the two extreme solutions denote reduced ranges of the feasible operating points. Additionally, with a peak overall performance again bounded into a limited range of $0.659 \div 0.662$, the trade-off solution results as an optimal choice when considering the entire envelope, despite improvements on the baseline are minimal.

The preceding considerations are visualised through flow field snapshots below. Critical evolution at high *IVR*, obtained with the minimum drag solution at low Re_{hl} , are reported in Figure 4.18. While the external cowl portrays no significant variations with respect to near-design configurations, the internal ducting is evidently experiencing massive low pressures, which also affect a major region of the blade suction side (Fig. 4.18a). The flow obstruction results clear from the vapour regions extensions at the inlet, which now are consistently distributed even on the hub surface (Fig. 4.18b). As a

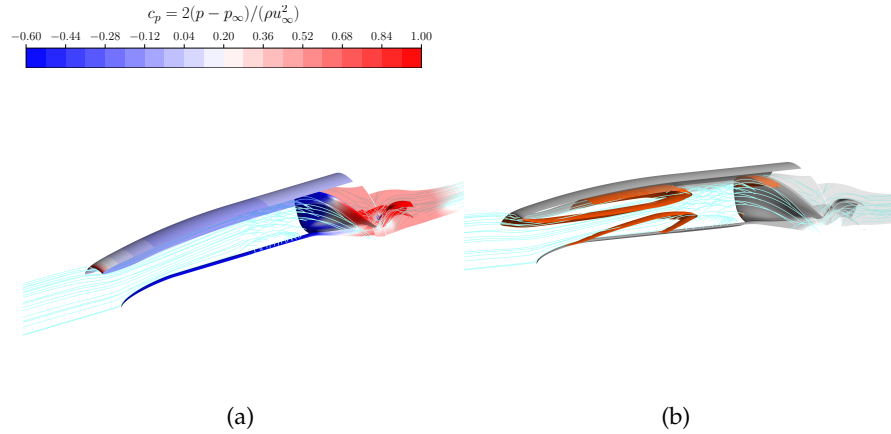


Figure 4.18: Contours of free-stream axial velocity–based pressure coefficient on the *opt2* propulsor walls, superimposed with a single-channel streamlines distribution at near take-off conditions with $IVR = 1.21$ (a) and the corresponding cavitation volumes visualised through isosurfaces of vapour volume fractions, $\alpha_v = 0.3$ (b). Case with $n = 2000$ rpm and $Re_{hl} = 60\% Re_{hl,design}$.

consequence, the mass flow rate is altered not only in terms of magnitude, which produces smaller IVR values if compared with similarity conditions at slower regimes, but also regarding its optimal distribution. In fact, while pump starvation promotes the vapour generation at the tip, the flow distortion causes cavitation to occur also at the blade root. This observation sets a difference with the isolated thrust breakdown analysis, where the vapour volumes gradually extend from the tip as the inflow total pressures reduces. However, the axial placement of the pump seems to partially prevents inlet cavitation clouds to directly touch the blades. Off-design operations of the rotor induce non-optimal conditions at the stator leading edge, which consequently experiences high angles of attack, thus resulting in cavitation occurring on the suction side along the entire span.

High advancing speeds operations ($Re_{hl} = 140\% Re_{hl,design}$) represent a difficult operating point for geometries characterised by low design IVR , as in the case of individual *opt2* (Fig. 4.19). However, in this case the pump is far from cavitating conditions and the efficiency loss is rather due to the transition of the stagnation point toward the suction side, deriving from the increment of the processed mass flow rate. As a consequence, this part of the blade operates under higher pressure distributions, which holds true even for the inner inlet ducting as a consequence of the capture stream tube stagnation line located internally (Fig. 4.19a). Here, the propulsor performance drop is almost entirely a result of non-optimal flow distribution on the outer walls. Specifically, with the pump operations not departing from the characteristic curve, the efficiency deduction is to be attributed to the lower pressures occurring on the cowl. At

4. OPTIMISATION

particularly low IVR values, these region experiences cavitation (Fig. 4.19b) . Here, the cloud is significantly more extended than in the baseline geometry.

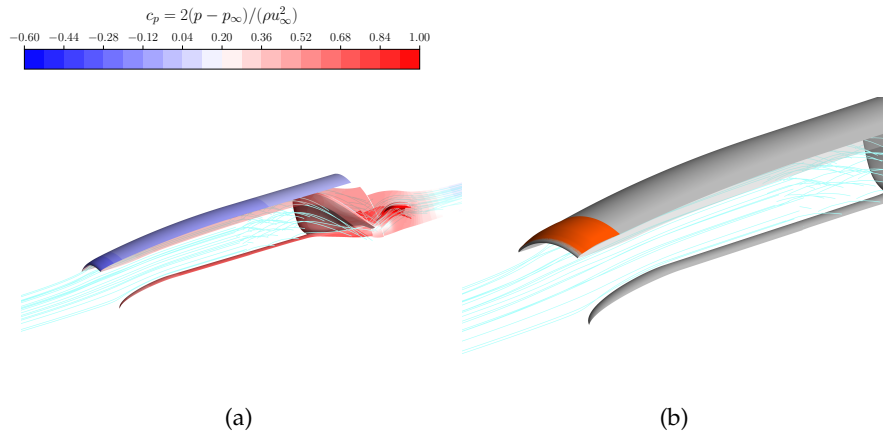


Figure 4.19: Contours of free-stream axial velocity–based pressure coefficient on the *opt1* propulsor walls, superimposed with a single-channel streamlines distribution at near take-off conditions with $IVR = 0.63$ (a) and the corresponding cavitation volumes visualised through isosurfaces of vapour volume fractions, $\alpha_v = 0.3$ (b). Case with $n = 2000$ rpm and $Re_{hl} = 140\% Re_{hl,design}$.

This flow phenomenon boosts the ϕ_{nac} component, thus inducing a drag increment. However, the lack of a concomitant hydraulic drop seems to justify the slower decay than the one observed at low speeds.

This last concept is further confirmed when the best performing geometry at $Re_{hl} = 140\% Re_{hl,design}$ is considered, i.e. *opt2*. Here, the internal flow pressure evolution is essentially unchanged from the previous one (Fig. 4.20a) . Conversely, the external walls depict much higher c_p values, especially in the near lip region, which is where the stream experiences the highest acceleration. As a result, a higher IVR results in a suppression of the external vapour generation (Fig. 4.20b) . Thus, from the flow field integration the propulsive efficiency results improved by more than 5% over the *opt1* corresponding performance.

Finally, the trade-off solution proves the only geometry that can conjugate the two objectives of the optimisation. However, the manipulation adopted during the process shows its limits. Shorter shapes than considered and additional variability on the plug axial locations appear as possible drivers for a further performance improvement. At the local level, increasing the number of degrees of freedom, by letting autonomous modification of the interior splines control points, appear as a natural consequent approach. Considering the critical off-design operations observed in the optimised individuals, the single-point optimisation here conducted proves an insufficient approach. Thus, in addition to an advanced geometrical variation, a multi-point strategy

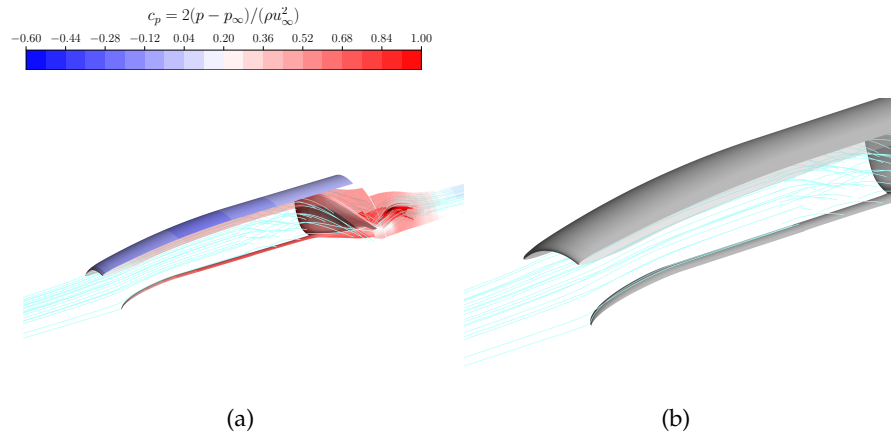


Figure 4.20: Contours of free-stream axial velocity–based pressure coefficient on the *opt2* propulsor walls, superimposed with a single-channel streamlines distribution at near take-off conditions with $IVR = 0.74$ (a) and the corresponding cavitation volumes visualised through isosurfaces of vapour volume fractions, $\alpha_v = 0.3$ (b). Case with $n = 2000 \text{ rpm}$ and $Re_{hl} = 140\% Re_{hl,design}$.

results mandatory. Anyhow, assuming the pumping device fixed represents a strong limit. The results commented so far seem to suggest that without modifying the two components simultaneously, a significant improvement is hardly reachable, since no solution is obtained for the performance peak shift observed in the detailed discussion on the baseline operations.

5 CONCLUSIONS AND OUTLOOK

The present state of waterjet marine propulsion is intrinsically tied to the integration of the propulsion system with the vessel. This integration poses challenges to significant advancements in propulsive performance due to flow distortions and losses introduced by the driving shaft and non-optimal capture stream tube, influenced by the nearby hull boundary layer. Recent innovations in industrial technology, particularly electric engines, have demonstrated the possibility for a novel propulsion system design. This Outboard Dynamic-inlet Waterjet (ODW) represents an innovative outboard device, independent of the specific vehicle application. Unlike traditional systems, the ODW is a stand-alone unit, housing the entire propulsion apparatus, reminiscent of aeronautical installations. This design eliminates the need for a shaft connecting the pump to the internal engine, allowing flexibility in propulsor placement below the waterline. Notably, this configuration overcomes previous limitations and ensures optimal alignment between thrust and advancing directions.

In light of these recent advancements, the current work aims to establish a comprehensive numerical framework for approaching the study of the proposed ODW system. By employing various methods with increasing complexity, the study provides essential tools for system design and the development of validated numerical models for analysing and optimising preliminary geometries.

Taking inspiration from fluid dynamic principles in aero-engines cowls, a 1D method is implemented to offer initial predictions of propulsive performance. Fundamental fluid dynamic laws are applied to an axisymmetric duct, with intake recovery modelled using experimental- and numerical-derived correlations, where the former are obtained from available measurements in literature, while the latter are derived from the present study systematic analyses. The code is compared with computations performed on an intake-installed pump configuration developed later in this work. Results show promising accuracy in estimating the thrust coefficient, though propulsive efficiency is still overestimated. In fact, while the CFD reference propulsor map denotes a peak performance, the meanline solution depicts a delay in the curves drop. As a consequence, at the best efficiency point the overprediction reaches a value of 6.7%, which gradually increases due to the opposite plot trends, with only minimal differences between the two correlations. A design approach for the bladed components is proposed, involving a BEM-aided meanline implementation. The method solves mass and flow momentum conservation principles through a predefined number of streamlines, discretising the stage channel. Empirical correlations, derived from experimental and numerical literature, are used to include in- and off-design deviation angles, head losses, and other

5. CONCLUSIONS AND OUTLOOK

effects. The code's accuracy is assessed by comparing global and local quantities with available experiments, concerning three test cases from different axial-flow pump applications. The analysis confirms significant accuracy in predicting flow directions and magnitudes, with a remarkable overlapping between experimental and computed spanwise distributions downstream of the blades. Conversely, underestimation of the head losses appears as a major cause for the pressure field overprediction. At the integral level, this effect mitigates the shaft power overestimate, thus resulting in pump efficiency maps as accurate as $\sim 1\%$ near design conditions. At off-design, the computed curves tend to depart from experimental data, showing discrepancies up to $\sim 10\%$. While this outcomes suggest a lack of strong calibration, the code stability is proved over wide range of operating conditions.

Validation of isolated geometries computational models begins with an open-source ram-type inlet shape, solved using 2D-axisymmetric RANS equations coupled with four turbulence models with incremental closure equation. Sensitivity to domain discretisation is assessed through incremental grid refinements, with computational results proving accurate in reproducing experimental flow evolution. Specifically, pressure coefficient distributions are analysed against measurements for both external and internal locations. Different combinations of grid resolution and turbulence modelling provides no additional accuracy for this field variable, while boundary layer specific statistics, such as y^+ and friction coefficients, depict major dependency on the turbulence treatment strategy. For pump validation, the AxWJ-2 test case is chosen, and an extensive study is conducted to numerically characterise the model under nominal and cavitating conditions. This analysis including the combination of three incremental discretisation refinements and three turbulence models with different boundary layer modelling strategies. While near design operations can in general reproduce experimental measurements with good agreement at both local and integral precision, thrust breakdown loops show poor reliability during fully-developed cavitation. This effect resulting especially as a consequence of a generalised tendency to overestimate the pressure rise capability. To this end, in-depth investigations are conducted to evaluate the influence of the ZGB cavitation model coefficients as possible drivers for accuracy improvement. Specifically, the head rise curve shows enhanced similarity to measurements when the nucleation site radius is increased, thus leading up to a 4% error reduction. The results from this phase of the work contribute to a published paper [9]. Based on insights from isolated investigations, an installation strategy is proposed to evaluate pump behaviour under the influence of an upstream dynamic inlet. During this study, the free stream velocity is varied while keeping the pump rotational speed fixed, repeating the computations for three different regimes. As a consequence, both hydraulic and propulsive statistics result from the assumption of nozzle adaption to ambient pressure at the exhaust section. While hydraulic

performance shows minimal sensitivity, the mutual inspection of propulsive statistics reveals non-optimal conditions, with distinct performance peaks of the two subsystems occurring at different operating points. Additionally, the entire system proves to operate under almost similarity conditions among the three regimes, except for a minor Reynolds effect penalising operations at lower speeds. However, when the boundary conditions are such that cavitation occurs on the intake, the similarity becomes affected by the evolution of vapour volumes on the inlet inner side, which induce performance degradation of the two subsystems.

To enhance the system's propulsive performance, an optimisation study focuses on the intake while assuming fixed blade geometry. A multi-fidelity strategy is adopted, optimising the 2D-axisymmetric model and evaluating off-design operations using the installed configuration. The baseline shape is parameterised and three decision variables are selected, namely: axial and radial coordinates of the highlight location and the vertical extension of the throat section. Thus, a genetic algorithm is employed after a starting from the post-processing data of a LHS analysis, performed on 150 individuals generated as triplets of the decision variables. Minimisation of both the intake drag and pressure recovery reveals the two objectives as conflicting. As a consequence, 15 individuals on the LHS Pareto are retained as initial population for a 30-generations based GA optimisation. The latter depicts an optimal solution as a shorter variant of the baseline, providing up to 3% increment in the propulsive efficiency. Despite this significant drag performance improvement, the pressure recovery has limited potential for maximisation. Additionally, simulations with the installed pump show that at off-design conditions, cavitation on the offspring may result anticipated, leading to drastic efficiency drops. As a consequence, while improvements for a single operating point may be moderate, the effects evaluated on wider mission envelopes are necessary to finally deem an individual as optimal or unfeasible.

Future developments

Based on the discussed points, several additional investigations are considered crucial:

1. Propulsor design method enhancement: The propulsor design method needs further refinement to enhance accuracy, particularly in terms of propulsive efficiency. Adopting a more robust approach, similar to the one commonly used for pumpjet ducting, is seen as a natural extension.
2. ARES calibration: A comprehensive calibration of ARES is anticipated as a near-future activity to minimise discrepancies in predicting the pressure field. This calibration is essential before introducing the capability to perform geometry manipulations within design explorations.
3. Integration of design codes: The integration of the two methods is ex-

5. CONCLUSIONS AND OUTLOOK

pected to create a comprehensive tool for the accurate design of the entire system. This outlook is considered as strictly tied to point 1.

4. Transient simulations and distorted inflow: The integrated model is intended to be utilized for transient simulations to better capture take-off dynamics and operations under inlet distortion conditions.
5. Advanced optimisation analysis: A more in-depth optimisation is planned, involving local manipulation of the intake splines. Moving towards a multi-point strategy will allow the inclusion of potential off-design detrimental effects before evaluating them using the installed model.

BIBLIOGRAPHY

- [1] ALLISON, J. L. "Marine Waterjet Propulsion". In: *SNAME Transactions* 101.T1993-1-SNAME (1993), pp. 275–335.
- [2] ANSYS, INC. *Ansys CFX Reference Guide*. Version 2022.R1. Aug. 2022.
- [3] ANSYS, INC. *Ansys CFX-Solver Theory Guide*. Version 2022.R1. Aug. 2022.
- [4] ANSYS, INC. *ANSYS Fluent Theory Guide*. Version 2022.R1. Jan. 2022.
- [5] ANSYS, INC. *Ansys Fluent User's Guide*. Version 2022.R1. Jan. 2022.
- [6] ARNDT, R., ARAKERI, V., and HIGUCHI, H. "Some observations of tip-vortex cavitation". In: *J. Fluid Mech.* 229 (1991), pp. 269–289. DOI: [10.1017/S0022112091003026](https://doi.org/10.1017/S0022112091003026).
- [7] ATHAVALE, M. M., LI, H. Y., JIANG, Y., and SINGHAL, A. K. "Application of the full cavitation model to pumps and inducers". In: *Int. J. Rotating Mach.* 8.1 (2002), pp. 45–56. DOI: [10.1155/s1023621x02000052](https://doi.org/10.1155/s1023621x02000052).
- [8] AUNGIER, R. H. *AXIAL-FLOW COMPRESSORS: A STRATEGY FOR AERODYNAMIC DESIGN AND ANALYSIS*. ASME PRESS, 2003.
- [9] AVANZI, F., BAÙ, A., DE VANNA, F., and BENINI, E. "Numerical Assessment of a Two-Phase Model for Propulsive Pump Performance Prediction". In: *Energies* 16.18 (2023). DOI: [10.3390/en16186592](https://doi.org/10.3390/en16186592).
- [10] AVANZI, F., DE VANNA, F., BENINI, E., RUARO, F., and GOBBO, W. "Analysis of Drag Sources in a Fully Submerged Waterjet". In: *The 9th Conference on Computational Methods in Marine Engineering (Marine 2021)*. Vol. 1. June 2021. DOI: [10.2218/marine2021.6824](https://doi.org/10.2218/marine2021.6824).
- [11] AVANZI, F., DE VANNA, F., RUAN, Y., and BENINI, E. "Design-Assisted of Pitching Aerofoils through Enhanced Identification of Coherent Flow Structures". In: *Designs* 5(1).11 (2021). DOI: [10.3390/designs5010011](https://doi.org/10.3390/designs5010011).
- [12] AVANZI, F., DE VANNA, F., RUAN, Y., and BENINI, E. "Enhanced Identification of Coherent Structures in the Flow Evolution of a Pitching Wing". In: *AIAA SciTech Forum 2022*. San Diego, CA & Virtual, Jan. 2022. DOI: [10.2514/6.2022-0182](https://doi.org/10.2514/6.2022-0182).
- [13] BAI, X.-r., CHENG, H.-y., JI, B., and LONG, X.-p. "Large eddy simulation of tip leakage cavitating flow focusing on cavitation-vortex interaction with Cartesian cut-cell mesh method". In: *J. Hydrodyn.* 30.4 (2018), pp. 750–753. DOI: [10.1007/s42241-018-0068-8](https://doi.org/10.1007/s42241-018-0068-8).

BIBLIOGRAPHY

- [14] BANIHASHEMIAN, S. and ADIBNIA, F. "A Novel Robust Soft-Computed Range-Free Localization Algorithm Against Malicious Anchor Nodes". In: *Cognitive Computation* 13 (July 2021). DOI: [10.1007/s12559-021-09879-w](https://doi.org/10.1007/s12559-021-09879-w).
- [15] BANJAC, M. and PETROVIC, M. V. "Development of Method and Computer Program for Multistage Axial Compressor Design: Part I — Mean Line Design and Example Cases". In: vol. Volume 2C: Turbomachinery. Turbo Expo: Power for Land, Sea, and Air. June 2018. DOI: [10.1115/GT2018-75410](https://doi.org/10.1115/GT2018-75410).
- [16] BANJAC, M., PETROVIC, M. V., and WIEDERMANN, A. "Secondary Flows, Endwall Effects, and Stall Detection in Axial Compressor Design". In: *Journal of Turbomachinery* 137.5 (May 2015), p. 051004. DOI: [10.1115/1.4028648](https://doi.org/10.1115/1.4028648).
- [17] BENINI, E. "Advances in Aerodynamic Design of Gas Turbines Compressors". In: *Gas Turbines*. Ed. by G. INJETI. Rijeka: IntechOpen, 2010. Chap. 1. DOI: [10.5772/10205](https://doi.org/10.5772/10205).
- [18] BRANDAU, J. H. *ASPECTS OF PERFORMANCE EVALUATION OF WATERJET PROPULSION SYSTEMS AND A CRITICAL REVIEW OF THE STATE-OF-THE-ART*. Tech. rep. Report 2550. Available online: <https://apps.dtic.mil/sti/pdfs/AD0827069.pdf>. DAVID W TAYLOR NAVAL SHIP RESEARCH and DEVELOPMENT CENTER BETHESDA MD, Oct. 1967.
- [19] BRANDAU, J. H. "Performance of Waterjet Propulsion Systems- A Review of the State-of-the-Art". In: *Journal of Hydronautics* 2.2 (1968), pp. 61–73. DOI: [10.2514/3.62775](https://doi.org/10.2514/3.62775).
- [20] BRENNEN, C. E. *Cavitation and bubble dynamics*. Cambridge university press, 2014.
- [21] BRENNEN, C. E. *Hydrodynamics of pumps*. Cambridge University Press, 2011.
- [22] BULTEN, N. W. H. "Numerical Analysis of a Waterjet Propulsion System". Available online: <https://research.tue.nl/files/2277312/200612081.pdf>. PhD thesis. Technische Universiteit Eindhoven, 2006. DOI: [10.6100/IR614907](https://doi.org/10.6100/IR614907).
- [23] CARRARO, M., DE VANNA, F., ZWEIRI, F., BENINI, E., HEIDARI, A., and HADAVINIA, H. "CFD modeling of wind turbine blades with eroded leading edge". In: *Fluids* 7.9 (2022), p. 302. DOI: [10.3390/fluids7090302](https://doi.org/10.3390/fluids7090302).
- [24] CELIK, I. B., GHIA, U., ROACHE, P. J., and FREITAS, C. J. "Procedure for estimation and reporting of uncertainty due to discretization in CFD applications". In: *J. Fluids Eng. Trans. ASME* 130.7 (2008). DOI: [10.1115/1.2960953](https://doi.org/10.1115/1.2960953).

- [25] CHEN, H., DOELLER, N., LI, Y., and KATZ, J. "Experimental Investigations of Cavitation Performance Breakdown in an Axial Waterjet Pump". In: *J. Fluids Eng.* (2020). DOI: [10.1115/1.4047287](https://doi.org/10.1115/1.4047287).
- [26] CHENG, H., LONG, X., JI, B., PENG, X., and FARHAT, M. "LES investigation of the influence of cavitation on flow patterns in a confined tip-leakage flow". In: *Ocean Eng.* 186 (2019), p. 106115. DOI: [10.1016/j.oceaneng.2019.106115](https://doi.org/10.1016/j.oceaneng.2019.106115).
- [27] CHENG, H., BAI, X., LONG, X., JI, B., PENG, X., and FARHAT, M. "Large eddy simulation of the tip-leakage cavitating flow with an insight on how cavitation influences vorticity and turbulence". In: *Appl. Math. Model.* 77 (2020), pp. 788–809. DOI: [10.1016/j.apm.2019.08.005](https://doi.org/10.1016/j.apm.2019.08.005).
- [28] CHESNAKAS, C. J., DONNELLY, M. J., PFITSCH, D. W., BECNEL, A. J., and SCHROEDER, S. D. *Performance Evaluation of the ONR Axial Waterjet 2 (AxWJ-2)*. Tech. rep. NSWCCD-50-TR-2009/089. Available online: <https://apps.dtic.mil/sti/pdfs/ADA516369.pdf>. Naval Surface Warfare Center Carderock Division, Dec. 2009.
- [29] CHRISTIE, R. "Propulsion System Integration and Modelling Synthesis". Available online: <https://dspace.lib.cranfield.ac.uk/handle/1826/11711>. PhD thesis. University of Cranfield, 2016.
- [30] CROUSE, J. E., SOLTIS, R. F., and MONTGOMERY, J. C. *Investigation of the Performance of an Axial-Flow-Pump Stage Designed by the Blade-Element Theory: Blade-Element Data*. Tech. rep. NASA-TN-D-1109. Available online: <https://ntrs.nasa.gov/api/citations/19980228119/downloads/19980228119.pdf>. NASA, Dec. 1961.
- [31] DE VANNA, F., AVANZI, F., COGO, M., SANDRIN, S., BETTENCOURT, M., PICANO, F., and BENINI, E. "GPU-acceleration of Navier-Stokes solvers for compressible wall-bounded flows: the case of URANOS". In: *AIAA SCITECH 2023 Forum*. National Harbor, MD & Online, Jan. 2023. DOI: [10.2514/6.2023-1129](https://doi.org/10.2514/6.2023-1129).
- [32] DE VANNA, F., AVANZI, F., COGO, M., SANDRIN, S., BETTENCOURT, M., PICANO, F., and BENINI, E. "URANOS: A GPU accelerated Navier-Stokes solver for compressible wall-bounded flows". In: *Computer Physics Communications* 287 (2023), p. 108717. DOI: [10.1016/j.cpc.2023.108717](https://doi.org/10.1016/j.cpc.2023.108717).
- [33] DE VANNA, F., BALDAN, G., PICANO, F., and BENINI, E. "Effect of convective schemes in wall-resolved and wall-modeled LES of compressible wall turbulence". In: *Comput. Fluids* 250 (2023), p. 105710. DOI: [10.1016/j.compfluid.2022.105710](https://doi.org/10.1016/j.compfluid.2022.105710).

BIBLIOGRAPHY

- [34] DE VANNA, F., BERNARDINI, M., PICANO, F., and BENINI, E. "Wall-modeled LES of shock-wave/boundary layer interaction". In: *Int. J. Heat Fluid Flow* 98 (2022), p. 109071. DOI: [10.1016/j.ijheatfluidflow.2022.109071](https://doi.org/10.1016/j.ijheatfluidflow.2022.109071).
- [35] DE VANNA, F., BOF, D., and BENINI, E. "Multi-objective RANS aerodynamic optimization of a hypersonic intake ramp at Mach 5". In: *Energies* 15.8 (2022), p. 2811. DOI: [10.3390/en15082811](https://doi.org/10.3390/en15082811).
- [36] DEAN, A., VOSS, D., and DRAGULJIĆ, D. *Design and Analysis of Experiments*. Springer Cham, 2017. DOI: [10.1007/978-3-319-52250-0](https://doi.org/10.1007/978-3-319-52250-0).
- [37] DEB, K., SINDHYA, K., and OKABE, T. "Self-Adaptive Simulated Binary Crossover for Real-Parameter Optimization". In: GECCO '07. London, England: Association for Computing Machinery, 2007, pp. 1187–1194. DOI: [10.1145/1276958.1277190](https://doi.org/10.1145/1276958.1277190).
- [38] DECAIX, J., DREYER, M., BALARAC, G., FARHAT, M., and MÜNCH, C. "RANS computations of a confined cavitating tip-leakage vortex". In: *Eur. J. Mech. B Fluids* 67 (2018), pp. 198–210. DOI: [10.1016/j.euromechflu.2017.09.004](https://doi.org/10.1016/j.euromechflu.2017.09.004).
- [39] DENTON, J. D. "The 1993 IGTI Scholar Lecture: Loss Mechanisms in Turbomachines". In: *Journal of Turbomachinery* 115.4 (Oct. 1993), pp. 621–656. DOI: [10.1115/1.2929299](https://doi.org/10.1115/1.2929299).
- [40] DONG-RUN, W., JIN-FANG, T., XIAO-QING, Q., and JIN-ZHANG, F. "An Implicit Off-Design Deviation Angle Correlation of Axial Flow Compressor Blade Elements". In: vol. Volume 2B: Turbomachinery. Turbo Expo: Power for Land, Sea, and Air. June 2017, V02BT41A005. DOI: [10.1115/GT2017-63189](https://doi.org/10.1115/GT2017-63189).
- [41] DONGRUN, W., JINFANG, T., XIAOQING, Q., and TAN, Z. "Development of an off-design deviation angle prediction model for full blade span in axial flow compressors". In: *Proceedings of the Institution of Mechanical Engineers, Part G: Journal of Aerospace Engineering* 233.9 (2019), pp. 3170–3183. DOI: [10.1177/0954410018793265](https://doi.org/10.1177/0954410018793265).
- [42] ESLAMDOOST, A. "The Hydrodynamics of Waterjet/Hull Interaction". Available online: <https://publications.lib.chalmers.se/records/fulltext/208838/208838.pdf>. PhD thesis. Chalmers University of Technology, 2014.
- [43] FALTINSEN, O. M. *Hydrodynamics of High-Speed Marine Vehicles*. Cambridge University Press, 2006. DOI: [10.1017/CBO9780511546068](https://doi.org/10.1017/CBO9780511546068).
- [44] FAROKHI, S. *Aircraft Propulsion*. John Wiley & Sons, 2014. DOI: [10.1201/9781315156743](https://doi.org/10.1201/9781315156743).

- [45] FARRELL, K. J. and BILLET, M. L. "A Correlation of Leakage Vortex Cavitation in Axial-Flow Pumps". In: *J. Fluids Eng.* 116.3 (Sept. 1994), pp. 551–557. DOI: [10.1115/1.2910312](https://doi.org/10.1115/1.2910312).
- [46] FURUYA, O. and CHIANG, W. L. *A New Pumpjet Design Theory*. Tech. rep. N00014-85-C-0050. Available online: <https://apps.dtic.mil/sti/pdfs/ADA201353.pdf>. DAVID TAYLOR RESEARCH CENTER, June 1988.
- [47] GAGGERO, S. and MARTINELLI, M. "Design and analysis of pumpjet propulsors using CFD-based optimization". In: *Ocean Engineering* 277 (2023), p. 114304. DOI: [10.1016/j.oceaneng.2023.114304](https://doi.org/10.1016/j.oceaneng.2023.114304).
- [48] GAGGERO, S., TANI, G., VIVIANI, M., and CONTI, F. "A study on the numerical prediction of propellers cavitating tip vortex". In: *Ocean Eng.* 92 (2014), pp. 137–161. DOI: [10.1016/j.oceaneng.2014.09.042](https://doi.org/10.1016/j.oceaneng.2014.09.042).
- [49] GUO, J., ZHANG, Y., CHEN, Z., and FENG, Y. "CFD-based multi-objective optimization of a waterjet-propelled trimaran". In: *Ocean Engineering* 195 (2020), p. 106755. DOI: [10.1016/j.oceaneng.2019.106755](https://doi.org/10.1016/j.oceaneng.2019.106755).
- [50] GUO, Q., HUANG, X., and QIU, B. "Numerical investigation of the blade tip leakage vortex cavitation in a waterjet pump". In: *Ocean Eng.* 187 (2019), p. 106170. DOI: [10.1016/j.oceaneng.2019.106170](https://doi.org/10.1016/j.oceaneng.2019.106170).
- [51] GUO, Q., ZHOU, L., WANG, Z., LIU, M., and CHENG, H. "Numerical simulation for the tip leakage vortex cavitation". In: *Ocean Eng.* 151 (2018), pp. 71–81. DOI: [10.1016/j.oceaneng.2017.12.057](https://doi.org/10.1016/j.oceaneng.2017.12.057).
- [52] HAN, C.-z., XU, S., CHENG, H.-y., JI, B., and ZHANG, Z.-y. "LES method of the tip clearance vortex cavitation in a propelling pump with special emphasis on the cavitation-vortex interaction". In: *J. Hydrodyn.* 32.6 (2020), pp. 1212-5–1216. DOI: [10.1007/s42241-020-0070-9](https://doi.org/10.1007/s42241-020-0070-9).
- [53] HANIMANN, L., MANGANI, L., CASARTELLI, E., and WIDMER, M. "Steady-state cavitation modeling in an open source framework: Theory and applied cases". In: *16th International Symposium on Transport Phenomena and Dynamics of Rotating Machinery*. 2016.
- [54] HATTE, R. and DAVIS, H. J. "Selection of Hydrofoil Waterjet Propulsion Systems". In: *Journal of Hydronautics* 1.1 (1967), pp. 12–22. DOI: [10.2514/3.62747](https://doi.org/10.2514/3.62747).
- [55] HENDERSON, R. E., MCMAHON, J. F., and WISLICENUS, G. F. *A METHOD FOR THE DESIGN OF PUMPJETS*. Tech. rep. NOW 63-0209-C-7. Available online: <https://apps.dtic.mil/sti/pdfs/AD0439631.pdf>. PENNSYLVANIA STATE UNIV STATE COLLEGE ORDNANCE RESEARCH LAB, May 1964.

BIBLIOGRAPHY

- [56] HERRIG, L. J., EMERY, J. C., and ERWIN, J. R. *Systematic two-dimensional cascade tests of NACA 65-series compressor blades at low speeds*. Tech. rep. NACA-TN-3916. Available online: <https://ntrs.nasa.gov/api/citations/19930084843/downloads/19930084843.pdf>. NASA, Feb. 1957.
- [57] HESS, J. and SMITH, A. "Calculation of potential flow about arbitrary bodies". In: *Progress in Aerospace Sciences* 8 (1967), pp. 1–138. DOI: [10.1016/0376-0421\(67\)90003-6](https://doi.org/10.1016/0376-0421(67)90003-6).
- [58] HOWELL, A. R. "Fluid Dynamics of Axial Compressors". In: *Proceedings of the Institution of Mechanical Engineers* 153.1 (1945), pp. 441–452. DOI: [10.1243/PIME_PROC_1945_153_049_02](https://doi.org/10.1243/PIME_PROC_1945_153_049_02).
- [59] HUANG, R., DAI, Y., LUO, X., WANG, Y., and HUANG, C. "Multi-objective optimization of the flush-type intake duct for a waterjet propulsion system". In: *Ocean Engineering* 187 (2019), p. 106172. DOI: [10.1016/j.oceaneng.2019.106172](https://doi.org/10.1016/j.oceaneng.2019.106172).
- [60] HUANG, X., SHI, S., SU, Z., TANG, W., and HUA, H. "Reducing underwater radiated noise of a SUBOFF model propelled by a pump-jet without tip clearance: Numerical simulation". In: *Ocean Engineering* 243 (2022), p. 110277. DOI: [10.1016/j.oceaneng.2021.110277](https://doi.org/10.1016/j.oceaneng.2021.110277).
- [61] JIANG, J., DING, J., LYU, N., LUO, H., and LI, L. "Control volume determination for submerged waterjet system in self-propulsion". In: *Ocean Engineering* 265 (2022), p. 112594. DOI: [10.1016/j.oceaneng.2022.112594](https://doi.org/10.1016/j.oceaneng.2022.112594).
- [62] JIANG, J. W. and HUANG, W. X. "Hydrodynamic design of an advanced submerged propulsion". In: *Proceedings of the Institution of Mechanical Engineers, Part C: Journal of Mechanical Engineering Science* 233.18 (2019), pp. 6367–6382. DOI: [10.1177/0954406219860166](https://doi.org/10.1177/0954406219860166).
- [63] JOHNSON, I. A. and BULLOCK, R. O. *Aerodynamic Design of Axial-Flow Compressors*. Tech. rep. NASA-SP-36. Available online: <https://ntrs.nasa.gov/api/citations/19650013744/downloads/19650013744.pdf>. NASA, Jan. 1965.
- [64] KATOCH, S., CHAUHAN, S., and KUMAR, V. "A review on genetic algorithm: past, present, and future." In: *Multimed Tools Appl* 80 (2021), pp. 8091–8126. DOI: [10.1007/s11042-020-10139-6](https://doi.org/10.1007/s11042-020-10139-6).
- [65] KAWANAMI, Y., KATO, H., YAMAGUCHI, H., TANIMURA, M., and TAGAYA, Y. "Mechanism and Control of Cloud Cavitation". In: *J. Fluids Eng.* (1997). DOI: [10.1115/1.2819499](https://doi.org/10.1115/1.2819499).
- [66] KIDIKIAN, J. and REGGIO, M. "Off-Design Prediction of Transonic Axial Compressors: Part 1 — Mean-Line Code and Tuning Factors". In: vol. Volume 2A: Turbomachinery. Turbo Expo: Power for Land, Sea, and Air. June 2018, V02AT39A002. DOI: [10.1115/GT2018-75124](https://doi.org/10.1115/GT2018-75124).

- [67] KOCH, C. C. and SMITH L. H., J. "Loss Sources and Magnitudes in Axial-Flow Compressors". In: *Journal of Engineering for Power* 98.3 (July 1976), pp. 411–424. DOI: [10.1115/1.3446202](https://doi.org/10.1115/1.3446202) .
- [68] KONAK, A., COIT, D. W., and SMITH, A. E. "Multi-objective optimization using genetic algorithms: A tutorial". In: *Reliability Engineering & System Safety* 91.9 (2006). Special Issue - Genetic Algorithms and Reliability, pp. 992–1007. DOI: [10.1016/j.ress.2005.11.018](https://doi.org/10.1016/j.ress.2005.11.018) .
- [69] KUBOTA, A., KATO, H., YAMAGUCHI, H., and MAEDA, M. "Unsteady structure measurement of cloud cavitation on a foil section using conditional sampling technique". In: *J. Fluids Eng.* (1989). DOI: [10.1115/1.3243624](https://doi.org/10.1115/1.3243624) .
- [70] LABORDE, R., CHANTREL, P., and MORY, M. "Tip Clearance and Tip Vortex Cavitation in an Axial Flow Pump". In: *J. Fluids Eng.* 119.3 (Sept. 1997), pp. 680–685. DOI: [10.1115/1.2819298](https://doi.org/10.1115/1.2819298) .
- [71] LAFRANCE, P. *A Review of Resistance Prediction and Design Methods for Strut-Pod Inlets*. Tech. rep. SPD-789-O1. Available online: <https://apps.dtic.mil/sti/pdfs/ADA052710.pdf>. DAVID W TAYLOR NAVAL SHIP RESEARCH and DEVELOPMENT CENTER BETHESDA MD SHIP PERFORMANCE DEPT, Apr. 1978.
- [72] LANGTRY, R. B. and MENTER, F. R. "Correlation-Based Transition Modeling for Unstructured Parallelized Computational Fluid Dynamics Codes". In: *AIAA Journal* 47.12 (2009), pp. 2894–2906. DOI: [10.2514/1.42362](https://doi.org/10.2514/1.42362) .
- [73] LAUNDER, B. and SPALDING, D. "The numerical computation of turbulent flows". In: *Computer Methods in Applied Mechanics and Engineering* 3.2 (1974), pp. 269–289. DOI: [10.1016/0045-7825\(74\)90029-2](https://doi.org/10.1016/0045-7825(74)90029-2) .
- [74] LEI, T., SHAN, Z. B., LIANG, C. S., CHUAN, W. Y., and BIN, W. B. "Numerical simulation of unsteady cavitation flow in a centrifugal pump at off-design conditions". In: *Proc. Inst. Mech. Eng. C: J. Mech. Eng. Sci.* 228.11 (2014), pp. 1994–2006. DOI: [10.1177/0954406213514573](https://doi.org/10.1177/0954406213514573) .
- [75] LEVY, J. "The Design of Water-Jet Propulsion Systems for Hydrofoil Craft". In: *Marine Technology and SNAME News* 2.01 (Jan. 1965), pp. 15–25. DOI: [10.5957/mt1.1965.2.1.15](https://doi.org/10.5957/mt1.1965.2.1.15) .
- [76] LINDAU, J. W., PENA, C., BAKER, W. J., DREYER, J. J., MOODY, W. L., KUNZ, R. F., and PATERSON, E. G. "Modeling of cavitating flow through waterjet propulsors". In: *Int. J. Rotating Mach.* 2012 (2012). DOI: [10.1155/2012/716392](https://doi.org/10.1155/2012/716392) .

BIBLIOGRAPHY

- [77] LIU, H.-I., WANG, J., WANG, Y., ZHANG, H., and HUANG, H. "Influence of the empirical coefficients of cavitation model on predicting cavitating flow in the centrifugal pump". In: *Int. J. Nav. Archit. Ocean Eng.* 6.1 (2014), pp. 119–131. DOI: [10.2478/IJNAOE-2013-0167](https://doi.org/10.2478/IJNAOE-2013-0167).
- [78] LIU, J., LIU, S., WU, Y., JIAO, L., WANG, L., and SUN, Y. "Numerical investigation of the hump characteristic of a pump–turbine based on an improved cavitation model". In: *Comput Fluids* 68 (2012), pp. 105–111. DOI: [10.1016/j.compfluid.2012.08.001](https://doi.org/10.1016/j.compfluid.2012.08.001).
- [79] LONG, Y., AN, C., ZHU, R., and CHEN, J. "Research on hydrodynamics of high velocity regions in a water-jet pump based on experimental and numerical calculations at different cavitation conditions". In: *Phys. Fluids* 33.4 (2021), p. 045124. DOI: [10.1063/5.0040618](https://doi.org/10.1063/5.0040618).
- [80] LONG, Y., LONG, X., JI, B., and XING, T. "Verification and validation of Large Eddy Simulation of attached cavitating flow around a Clark-Y hydrofoil". In: *Int. J. Multiph. Flow* 115 (2019), pp. 93–107. DOI: [10.1016/j.ijmultiphaseflow.2019.03.026](https://doi.org/10.1016/j.ijmultiphaseflow.2019.03.026).
- [81] MAGRINI, A., BENINI, E., YAO, H.-D., POSTMA, J., and SHEAF, C. "A review of installation effects of ultra-high bypass ratio engines". In: *Progress in Aerospace Sciences* 119 (2020), p. 100680. DOI: [10.1016/j.paerosci.2020.100680](https://doi.org/10.1016/j.paerosci.2020.100680).
- [82] MAGRINI, A., BUOSI, D., and BENINI, E. "Maximisation of installed net resulting force through multi-level optimisation of an ultra-high bypass ratio engine nacelle". In: *Aerospace Science and Technology* 119 (2021), p. 107169. DOI: [10.1016/j.ast.2021.107169](https://doi.org/10.1016/j.ast.2021.107169).
- [83] MAGRINI, A., BUOSI, D., BENINI, E., and SHEAF, C. "Ultra-high bypass nacelle geometry design space exploration". In: *AIAA Scitech 2021 Forum*. DOI: [10.2514/6.2021-0990](https://doi.org/10.2514/6.2021-0990).
- [84] MARQUARDT, M. W. *Summary of Two Independent Performance Measurements of the ONR Axial Waterjet 2 (AxWJ-2)*. Tech. rep. NSWCCD-50-TR-2011/016. Available online: <https://apps.dtic.mil/sti/tr/pdf/ADA540499.pdf>. Naval Surface Warfare Center Carderock Division, Mar. 2011.
- [85] MCDONALD, A. and FOX, R. "An experimental investigation of incompressible flow in conical diffusers". In: *International Journal of Mechanical Sciences* 8.2 (1966), pp. 125–139. DOI: [10.1016/0020-7403\(66\)90071-3](https://doi.org/10.1016/0020-7403(66)90071-3).
- [86] MCDONALD, A. and FOX, R. *INCOMPRESSIBLE FLOW IN CONICAL DIFFUSERS*. Tech. rep. DA-31-124-ARO(D)-138. Available online: <https://apps.dtic.mil/sti/pdfs/AD0448505.pdf>. Purdue Research Foundation, 1964.

- [87] MEJRI, I., BAKIR, F., REY, R., and BELAMRI, T. "Comparison of computational results obtained from a homogeneous cavitation model with experimental investigations of three inducers". In: *J. Fluids Eng.* (2006). DOI: [10.1115/1.2353265](https://doi.org/10.1115/1.2353265).
- [88] MENEGOZZO, L. "Development of a Numerical Code for Analysis and Design of Axial Compressors operating under Inlet Flow Distortion". PhD thesis. Università degli Studi di Padova, 2020.
- [89] MENEGOZZO, L. and BENINI, E. "Meanline Calculation of Surge Margin Loss due to Inlet Flow Distortion". In: vol. Volume 2A: Turbomachinery. Turbo Expo: Power for Land, Sea, and Air. Sept. 2020. DOI: [10.1115/GT2020-14775](https://doi.org/10.1115/GT2020-14775). eprint: <https://asmedigitalcollection.asme.org/GT/proceedings-pdf/GT2020/84065/V02AT32A030/6614131/v02at32a030-gt2020-14775.pdf>.
- [90] MENTER, F. R. "Eddy Viscosity Transport Equations and Their Relation to the $k-\varepsilon$ Model". In: *J. Fluids Eng. Trans. ASME* 119.4 (Dec. 1997), pp. 876–884. DOI: [10.1115/1.2819511](https://doi.org/10.1115/1.2819511).
- [91] MENTER, F. R. "Two-equation eddy-viscosity turbulence models for engineering applications". In: *AIAA journal* 32.8 (1994), pp. 1598–1605. DOI: [10.2514/3.12149](https://doi.org/10.2514/3.12149).
- [92] MICHAEL, T. J., SCHROEDER, S. D., and BECNEL, A. J. *Design of the ONR AxWJ-2 Axial Flow Water Jet Pump*. Tech. rep. NSWCCD-50-TR-2008/066. Available online: <https://apps.dtic.mil/sti/pdfs/ADA489739.pdf>. Naval Surface Warfare Center Carderock Division, Nov. 2008.
- [93] MILLER, M. J., CROUSE, J. E., and SANDERCOCK, D. M. "Summary of Experimental Investigation of Three Axial-Flow Pump Rotors Tested in Water". In: *Journal of Engineering for Power* 89.4 (Oct. 1967), pp. 589–599. DOI: [10.1115/1.3616748](https://doi.org/10.1115/1.3616748).
- [94] MILLER, M. J., OKIISHI, T. H., SEROVY, G. K., SANDERCOCK, D. M., and BRITSCH, W. R. *Summary of design and blade-element performance data for 12 axial-flow pump rotor configurations*. Tech. rep. NASA-TN-D-7074. Available online: <https://ntrs.nasa.gov/api/citations/19730006255/downloads/19730006255.pdf>. NASA, Jan. 1973.
- [95] MIRJALILI, S., SONG DONG, J., SADIQ, A. S., and FARIS, H. "Genetic Algorithm: Theory, Literature Review, and Application in Image Reconstruction". In: *Nature-Inspired Optimizers: Theories, Literature Reviews and Applications*. Ed. by S. MIRJALILI, J. SONG DONG, and A. LEWIS. Cham: Springer International Publishing, 2020, pp. 69–85. DOI: [10.1007/978-3-030-12127-3_5](https://doi.org/10.1007/978-3-030-12127-3_5).

BIBLIOGRAPHY

- [96] MOTLEY, M. R., SAVANDER, B. R., and YOUNG, Y. L. "Influence of Spatially Varying Flow on the Dynamic Response of a Waterjet inside an SES". In: *Int. J. Rotating Mach.* 2014 (2014). DOI: [10.1155/2014/275916](https://doi.org/10.1155/2014/275916).
- [97] OKIISHI, T. H. and PULLEN, C. R. "Nonconvergence in the Computation of Turbomachinery Performance". In: *Journal of Mechanical Engineering Science* 17.5 (1975), pp. 285–292. DOI: [10.1243/JMES_JOUR_1975_017_041_02](https://doi.org/10.1243/JMES_JOUR_1975_017_041_02).
- [98] OKIISHI, T., MILLER, M., KAVANAGH, P., and SEROVY, G. "Axial-flow pump blade-element loss and deviation angle prediction". In: *International Journal of Mechanical Sciences* 17.10 (1975), pp. 633–641. DOI: [10.1016/0020-7403\(75\)90081-8](https://doi.org/10.1016/0020-7403(75)90081-8).
- [99] PARK, W. G., JANG, J. H., CHUN, H. H., and KIM, M. C. "Numerical flow and performance analysis of waterjet propulsion system". In: *Ocean Engineering* 32.14 (2005), pp. 1740–1761. DOI: [10.1016/j.oceaneng.2005.02.004](https://doi.org/10.1016/j.oceaneng.2005.02.004).
- [100] PARK, W. G., YUN, H. S., CHUN, H. H., and KIM, M. C. "Numerical flow simulation of flush type intake duct of waterjet". In: *Ocean Engineering* 32.17 (2005), pp. 2107–2120. DOI: [10.1016/j.oceaneng.2005.03.001](https://doi.org/10.1016/j.oceaneng.2005.03.001).
- [101] POLLARD, D. and GOSTELOW, J. P. "Some Experiments at Low Speed on Compressor Cascades". In: *Journal of Engineering for Power* 89.3 (July 1967), pp. 427–436. DOI: [10.1115/1.3616709](https://doi.org/10.1115/1.3616709).
- [102] RAMIREZ RUBIO, S. and MACMANUS, D. "Framework for estimation of nacelle drag on isolated aero-engines with separate jets". In: *Proceedings of the Institution of Mechanical Engineers, Part G: Journal of Aerospace Engineering* 234.14 (May 2020), pp. 2025–2040. DOI: [10.1177/0954410020922928](https://doi.org/10.1177/0954410020922928).
- [103] ROBINSON, M., MACMANUS, D. G., CHRISTIE, R., SHEAF, C., and GRECH, N. "Nacelle design for ultra-high bypass ratio engines with CFD based optimisation". In: *Aerospace Science and Technology* 113 (2021), p. 106191. DOI: [10.1016/j.ast.2020.106191](https://doi.org/10.1016/j.ast.2020.106191).
- [104] ROBINSON, M., MACMANUS, D. G., and SHEAF, C. "Aspects of aero-engine nacelle drag". In: *Proceedings of the Institution of Mechanical Engineers, Part G: Journal of Aerospace Engineering* 233.5 (2019), pp. 1667–1682. DOI: [10.1177/0954410018765574](https://doi.org/10.1177/0954410018765574).
- [105] EL-SAYED, A. *Aircraft Propulsion and Gas Turbine Engines*. CRC Press, Taylor & Francis Group, 2017. DOI: [10.1201/9781315156743](https://doi.org/10.1201/9781315156743).

- [106] SEROVY, G., KAVANAGH, P., OKIISHI, T., and MILLER. *PREDICTION OF OVERALL AND BLADE-ELEMENT PERFORMANCE FOR AXIAL-FLOW PUMP CONFIGURATIONS*. Tech. rep. NASA CR-2301. Available online: <https://ntrs.nasa.gov/api/citations/19730023457/downloads/19730023457.pdf>. NASA, Aug. 1973.
- [107] SHI, S., TANG, W., HUANG, X., DONG, X., and HUA, H. “Experimental and numerical investigations on the flow-induced vibration and acoustic radiation of a pump-jet propulsor model in a water tunnel”. In: *Ocean Engineering* 258 (2022), p. 111736. DOI: [10.1016/j.oceaneng.2022.111736](https://doi.org/10.1016/j.oceaneng.2022.111736).
- [108] SHIH, T.-H., LIOU, W. W., SHABBIR, A., YANG, Z., and ZHU, J. “A new $k-\varepsilon$ eddy viscosity model for high reynolds number turbulent flows”. In: *Computers & Fluids* 24.3 (1995), pp. 227–238. DOI: [10.1016/0045-7930\(94\)00032-T](https://doi.org/10.1016/0045-7930(94)00032-T).
- [109] SINGHAL, A. K., ATHAVALE, M. M., LI, H., and JIANG, Y. “Mathematical basis and validation of the full cavitation model”. In: *J. Fluids Eng.* 124.3 (2002), pp. 617–624. DOI: [10.1115/1.1486223](https://doi.org/10.1115/1.1486223).
- [110] SKINNER, S. and ZARE-BEHTASH, H. “State-of-the-art in aerodynamic shape optimisation methods”. In: *Applied Soft Computing* 62 (2018), pp. 933–962. DOI: [10.1016/j.asoc.2017.09.030](https://doi.org/10.1016/j.asoc.2017.09.030).
- [111] SOBOLEWSKI, A. D. *Hydrodynamic Performance of the Model of a Variable Area Waterjet Inlet Designed for a 200 Ton, 100 Knot Hydrofoil Ship*. Tech. rep. SPD—735—O1. Available online: <https://apps.dtic.mil/sti/pdfs/ADA038590.pdf>. DAVID W TAYLOR NAVAL SHIP RESEARCH and DEVELOPMENT CENTER BETHESDA MD SHIP PERFORMANCE DEPT, Feb. 1977.
- [112] SPALART, P. and ALLMARAS, S. “A one-equation turbulence model for aerodynamic flows”. In: *30th Aerospace Sciences Meeting and Exhibit*. DOI: [10.2514/6.1992-439](https://doi.org/10.2514/6.1992-439).
- [113] STÁKOWSKI, T., MACMANUS, D., SHEAF, C., and CHRISTIE, R. “Aerodynamics of Aero-Engine Installation”. In: *Proceedings of the Institution of Mechanical Engineers, Part G: Journal of Aerospace Engineering* 230.14 (2016), pp. 2673–2692. DOI: [10.1177/0954410016630332](https://doi.org/10.1177/0954410016630332).
- [114] STAVROPOULOS-VASILAKIS, E., KYRIAZIS, N., JADIDBONAB, H., KOUKOUVINIS, P., and GAVAISES, M. “Review of Numerical Methodologies for Modeling Cavitation”. In: *Cavitation and Bubble Dynamics* (2021), pp. 1–35. DOI: [10.1016/B978-0-12-823388-7.00004-7](https://doi.org/10.1016/B978-0-12-823388-7.00004-7).
- [115] STEDEN, M., HUNDEMER, J., and ABDEL-MAKSOU, M. “Optimisation of a Linearjet”. In: *First International Symposium on Marine Propulsors (smp'09)*. June 2009.

BIBLIOGRAPHY

- [116] SURYANARAYANA, C., SATYANARAYANA, B., and RAMJI, K. "Performance evaluation of an underwater body and pumpjet by model testing in cavitation tunnel". In: *International Journal of Naval Architecture and Ocean Engineering* 2.2 (2010), pp. 57–67. DOI: [10.2478/IJNAOE-2013-0020](https://doi.org/10.2478/IJNAOE-2013-0020).
- [117] SURYANARAYANA, C., SATYANARAYANA, B., RAMJI, K., and SAIJU, A. "Experimental evaluation of pumpjet propulsor for an axisymmetric body in wind tunnel". In: *International Journal of Naval Architecture and Ocean Engineering* 2.1 (2010), pp. 24–33. DOI: [10.2478/IJNAOE-2013-0016](https://doi.org/10.2478/IJNAOE-2013-0016).
- [118] SURYANARAYANA, SATYANARAYANA, B., RAMJI, K., and NAGESWARA, M. R. "Cavitation studies on axi-symmetric underwater body with pumpjet propulsor in cavitation tunnel". In: *International Journal of Naval Architecture and Ocean Engineering* 2.4 (2010), pp. 185–194. DOI: [10.2478/IJNAOE-2013-0035](https://doi.org/10.2478/IJNAOE-2013-0035).
- [119] TAN, D., LI, Y., WILKES, I., VAGNONI, E., MIORINI, R. L., and KATZ, J. "Experimental investigation of the role of large scale cavitating vortical structures in performance breakdown of an axial waterjet pump". In: *J. Fluids Eng.* 137.11 (2015). DOI: [10.1115/1.4030614](https://doi.org/10.1115/1.4030614).
- [120] TERWISGA, T. J. van. "A parametric propulsion prediction method for waterjet driven craft". In: *Proceedings of the 4th International Conference on FAST'97*. Available online: <https://repository.tudelft.nl/islandora/object/uuid:e82b243c-8f41-4396-9d75-51bf69d81dfd?collection=research>. 1997.
- [121] TONG, L. and DU, B. "Neural architecture search via reference point based multi-objective evolutionary algorithm". In: *Pattern Recognition* 132 (2022), p. 108962. DOI: [10.1016/j.patcog.2022.108962](https://doi.org/10.1016/j.patcog.2022.108962).
- [122] TOURNIER, J. and EL-GENK, M. S. "Axial flow, multi-stage turbine and compressor models". In: *Energy Conversion and Management* 51.1 (2010), pp. 16–29. DOI: [10.1016/j.enconman.2009.08.005](https://doi.org/10.1016/j.enconman.2009.08.005).
- [123] WANG, C., HE, X., CHENG, L., LUO, C., XU, J., CHEN, K., and JIAO, W. "Numerical Simulation on Hydraulic Characteristics of Nozzle in Waterjet Propulsion System". In: *Processes* 7.12 (2019). DOI: [10.3390/pr7120915](https://doi.org/10.3390/pr7120915).
- [124] WILCOX, D. C. "Reassessment of the scale-determining equation for advanced turbulence models". In: 26.11 (1988), pp. 1299–1310. DOI: [10.2514/3.10041](https://doi.org/10.2514/3.10041).

- [125] WISLICENUS, G. F. *Hydrodynamic Design Principles of Pumps and Ducting for Waterjet Propulsion*. Tech. rep. Report 3990. Available online: <https://apps.dtic.mil/sti/pdfs/AD0775620.pdf>. DAVID W TAYLOR NAVAL SHIP RESEARCH and DEVELOPMENT CENTER BETHESDA MD, June 1973.
- [126] WU, C., LU, Y., LIU, S., LI, Z., GU, Z., SHAO, W., and LI, C. “Research on Optimization Design of Fully Parameterized Pump-Jet Propulsion”. In: *Journal of Marine Science and Engineering* 10.6 (2022). DOI: [10.3390/jmse10060766](https://doi.org/10.3390/jmse10060766).
- [127] WU, H., MIORINI, R. L., and KATZ, J. “Measurements of the tip leakage vortex structures and turbulence in the meridional plane of an axial water-jet pump”. In: *Exp Fluids* 50 (2011), pp. 989–1003. DOI: [10.1007/s00348-010-0975-0](https://doi.org/10.1007/s00348-010-0975-0).
- [128] ZHANG, D., SHI, L., SHI, W., ZHAO, R., WANG, H., and VAN ESCH, B. B. “Numerical analysis of unsteady tip leakage vortex cavitation cloud and unstable suction-side-perpendicular cavitating vortices in an axial flow pump”. In: *Int. J. Multiph. Flow* 77 (2015), pp. 244–259. DOI: [10.1016/j.ijmultiphaseflow.2015.09.006](https://doi.org/10.1016/j.ijmultiphaseflow.2015.09.006).
- [129] ZHANG, R. and CHEN, H.-x. “Numerical analysis of cavitation within slanted axial-flow pump”. In: *J. Hydrodyn.* 25.5 (2013), pp. 663–672. DOI: [10.1016/S1001-6058\(13\)60411-4](https://doi.org/10.1016/S1001-6058(13)60411-4).
- [130] ZHAO, X., LIU, T., HUANG, B., and WANG, G. “Combined experimental and numerical analysis of cavitating flow characteristics in an axial flow waterjet pump”. In: *Ocean Eng.* 209 (2020), p. 107450. DOI: [10.1016/j.oceaneng.2020.107450](https://doi.org/10.1016/j.oceaneng.2020.107450).
- [131] ZHAO, Y., WANG, G., JIANG, Y., and HUANG, B. “Numerical analysis of developed tip leakage cavitating flows using a new transport-based model”. In: *Int. Commun. Heat Mass Transf.* 78 (2016), pp. 39–47. DOI: [10.1016/j.icheatmasstransfer.2016.08.007](https://doi.org/10.1016/j.icheatmasstransfer.2016.08.007).
- [132] ZHOU, Y., PAVESI, G., YUAN, J., and FU, Y. “A Review on Hydrodynamic Performance and Design of Pump-Jet: Advances, Challenges and Prospects”. In: *Journal of Marine Science and Engineering* 10(10).1514 (2022). DOI: [10.3390/jmse10101514](https://doi.org/10.3390/jmse10101514).
- [133] ZIERKE, W. C. and STRAKA, W. A. “Flow visualization and the three-dimensional flow in an axial-flow pump”. In: *Journal of Propulsion and Power* 12.2 (1996), pp. 250–259. DOI: [10.2514/3.24021](https://doi.org/10.2514/3.24021).
- [134] ZIERKE, W. C., STRALA, W. A., and TAYLOR, P. D. *THE HIGH REYNOLDS NUMBER FLOW THROUGH AN AXIAL-FLOW PUMP*. Tech. rep. TR 93-12. Available online: <https://apps.dtic.mil/sti/pdfs/ADA273844.pdf>. Applied Research Laboratory, Nov. 1993.

BIBLIOGRAPHY

- [135] ZWART, P. J., GERBER, A. G., BELAMRI, T., et al. "A two-phase flow model for predicting cavitation dynamics". In: *Fifth international conference on multiphase flow, Yokohama, Japan*. Vol. 152. 2004.

RINGRAZIAMENTI

Ed infine, il capitolo più complesso. Perché commentare metodi ed analisi potrà sembrare difficile, ma, di certo, mai quanto mettere per iscritto un sincero sentimento di riconoscenza verso chi, col proprio indispensabile supporto, mi accompagna ogni giorno.

Un ringraziamento speciale va al prof. Ernesto Benini, per avermi dato questa opportunità di formazione e per essere un punto di riferimento costante e disponibile, condividendo conoscenze dall'enorme valore scientifico. La mia massima riconoscenza a SEALENCE, per aver creduto in me fin dall'inizio, rendendo possibile questa esperienza, e per essere garanzia di confronto sempre professionale e competente.

Un grazie sincero a Francesco, ancor più che una guida irrinunciabile, un grande amico.

Grazie ad Alberto: il tuo contributo a questo lavoro è stato fondamentale. E grazie anche ai colleghi di TEMPEST, ad Andrea in particolare. Le poche occasioni di incontro mi hanno, però, sempre offerto spunti di riflessione costruttivi.

Ai miei Amici: grazie, perché in vostra compagnia ogni scalata diventa più leggera.

A Claudia, presenza costante, solido supporto e riferimento lungo questo sentiero.

Alla mia famiglia, a mia Mamma, a mia Sorella, a mia Nonna e a mio Padre. Al vostro esempio, ai vostri insegnamenti e al vostro sostegno devo la persona che sono oggi e i risultati che ho raggiunto fin qui. A te, Leonardo, perché sei arrivato da poco, ma mi hai già spiegato tanto.

E a chi, pur senza lasciare impronte, continua a camminare al mio fianco.